

ADVANCED LOWER LIMB MUSCLE MRI

LOWER LIMB MUSCLE ASSESSMENT USING DIFFUSION
TENSOR AND BLOOD OXYGEN-LEVEL DEPENDENT
IMAGING

By

ALYAA H. ELZIBAK, HON. B.SC., M.SC.

A Thesis

Submitted to the School of Graduate Studies

in Partial Fulfilment of the Requirements

for the Degree

Doctor of Philosophy

McMaster University

©Copyright by Alyaa H. Elzibak, January 2014

DOCTOR OF PHILOSOPHY (2014)

McMaster University

(Medical Physics and Applied Radiation Sciences)

Hamilton, Ontario

TITLE: Lower Limb Muscle Assessment Using Diffusion Tensor and Blood Oxygen-Level Dependent Imaging

AUTHOR: Alyaa H. Elzibak, Hon. B.Sc.(McMaster University), M.Sc.(McMaster University)

SUPERVISOR: Professor Michael D. Noseworthy, Ph.D.

COMMITTEE MEMBERS: Dr. Dinesh A. Kumbhare, MSc, MD, FRCPC.,
Dr. Srinivasan Harish, MBBS. FRCPC., Dr. Thomas J. Farrell, Ph.D.

NUMBER OF PAGES: xix, 230

Abstract

Diffusion tensor (DT) and blood oxygen-level dependent (BOLD) imaging are two noninvasive magnetic resonance (MR) techniques that have been used to probe skeletal muscle microstructure and microvasculature, respectively. Over a series of four studies, the work in this thesis aimed at furthering our understanding of baseline DT metrics and BOLD signals in lower limb muscles (calf and foot) of healthy young subjects. Since postural changes have been shown to alter numerous quantities, including fluid volumes and muscle cross sectional area, DT indices and BOLD signal characteristics were examined in response to movement from upright to supine position.

Reductions of 3.2-6.7% and 3.4-7.5% were measured in calf DT eigenvalues and apparent diffusion coefficient (ADC) in the various muscles, following 34 and 64 minutes of supine rest, respectively ($P < 0.05$). The changes observed between 34 minutes and 64 minutes of rest were not significant, indicating that a supine resting period of approximately thirty minutes is necessary to allow calf diffusion indices to stabilize in healthy young subjects (**chapter 4**). Investigating BOLD time series using fractals revealed a power law scaling in calf muscles, and most signals had a fractal dimension (FD) around 1.87. Spectral analysis showed that low frequency peaks (below 0.1 Hz) were the major contributors to the spectrum, with most of the fluctuations at frequencies lower than 0.01 Hz. None of the BOLD characteristics (mean signal intensity, standard deviation, FD, and underlying frequency components) seemed to be sensitive to subtle difference in muscle use between the two postural states (**chapter 5**).

Establishment of baseline diffusion metrics in the foot region was feasible (**chapter 6**). Examination of foot DT indices in response to positional change showed that the metrics decreased from 2.7-4.6% following 34 minutes of supine rest ($P < 0.05$) (**chapter 7**), further validating the need for a supine resting period prior to DT data collection. The use of DTI and BOLD imaging in muscle diseases or those that show an inflammatory muscle response (like COPD and CRPS) may further our understanding of muscle impairment. However, as potential differences were noted due to posture in DT metrics in healthy subjects, it would be advisable to test this effect in any disease prior to initiation of a full study.

Acknowledgements

My journey through graduate school has been guided by many individuals to whom I wish to express my appreciation. I owe gratitude to my supervisor, Dr. Michael D. Noseworthy, for his support from the start of the project through to its completion. Dr. Noseworthy has offered his time and expertise to generate ideas for the project and guide the research initiative. Under his mentorship, I have become equipped with valuable research skills that will allow me to positively contribute to the scientific community. I also wish to thank my supervisory committee members: Dr. Dinesh Kumbhare, Dr. Srinivasan Harish and Dr. Thomas Farrell. Their insightful input and kind support have enriched the thesis and have contributed to my academic growth. Discussions with Dr. Kumbhare have opened up avenues to explore and opportunities to pursue. I am especially grateful to Mr. Norm Konyer for patiently sharing his technical and practical MR expertise with me.

This thesis would not have been possible without the MR technologists, whom I wish to thank for their help during imaging sessions and for contributing to my understanding of the practical aspects of MRI. A special thank you to Cheryl Constant and Julie Lecomte. Many thanks to my friends and colleagues at the imaging research center, who provided suggestions and encouragement over the past few years. A special thank you to Andrew Davis and Conrad Rockel for sharing their expertise on muscle MR imaging. To the Medical Physics and Applied Radiation Sciences department, I am appreciative of your time and assistance when answering my administrative questions, guiding me towards resources and providing emotional support. I am also grateful to the Natural Sciences and Engineering Research Council of Canada (NSERC) for providing generous funding support for my project.

Thank you all for making my experiences at McMaster University enriching and memorable.

Last, but certainly not least, my family deserves special mention. I am indebted to my parents for their never-ending support and for showing me how to be resilient and patient. Without these traits, I would never have made it to the finish line. To my beloved husband, I am forever grateful for your encouragement and understanding. You have helped me organize my time at home and have supported me through the most difficult parts of my journey. My loving thanks to my siblings for being there for me and for their acts of kindness that have always lifted me up. To my little angel, although you have mostly distracted me from my thesis work, these distractions and your innocent smile have always re-energized me and have inspired me to remain focused. Thank you for bringing joy into my life!

Table of Contents

Abstract	iii
Acknowledgements	v
List of Figures	ix
List of Tables	xv
List of Notations and Abbreviations	xvii
Thesis Format	xix
Chapter 1 Introduction	1
1.1 Skeletal Muscles	2
1.1.1 Muscle Structure	2
1.1.2 Muscle Contraction	5
1.1.3 Muscle Fibers	8
1.1.4 Muscles of the Lower Limb	10
1.2 Diffusion Tensor Imaging of Skeletal Muscles	13
1.3 Blood Oxygen-Level Dependent Imaging of Skeletal Muscles	21
Chapter 2 Technical Details	34
2.1 Basic MRI Physics	35
2.1.1 Nuclear Properties	35
2.1.2 Nuclei in a Magnetic Field	37
2.1.3 Magnetization of a Sample	43
2.1.4 RF Excitation	46
2.1.5 Relaxation Mechanisms	51
2.1.6 Spatial Localization	55
2.1.7 Pulse Sequences	58
2.2 Diffusion Tensor Imaging	61
2.3 Blood Oxygen Level-Dependent Imaging	70
Chapter 3 Problem Definition and Thesis Objectives	80
3.1 Summary of Objectives	83

Chapter 4 Assessment of Diffusion Tensor Imaging Indices in Calf Muscles Following Postural Change from Standing to Supine Position	85
4.1 Context of the Paper	85
4.2 Declaration Statement	86
4.3 Paper	87
4.3.1 Abstract	88
4.3.2 Introduction	90
4.3.3 Materials and methods	92
4.3.4 Results	99
4.3.5 Discussion	102
4.3.6 Conclusion	114
4.3.7 Acknowledgements	114
4.3.8 References	115
Chapter 5 Analysis of Calf Blood Oxygen-Level Dependent (BOLD) Signal after Supine Posture	122
5.1 Context of the Paper	122
5.2 Declaration Statement	123
5.3 Paper	124
5.3.1 Abstract	125
5.3.2 Introduction	127
5.3.3 Materials and Methods	130
5.3.4 Results	134
5.3.5 Discussion	138
5.3.6 References	149
Chapter 6 Diffusion tensor imaging of the normal foot at 3T	158
6.1 Context of the Paper	158
6.2 Declaration Statement	159
6.3 Paper	160
6.3.1 Abstract	162

6.3.2	Introduction	164
6.3.3	Materials and Methods	167
6.3.4	Results	172
6.3.5	Discussion	177
6.3.6	References	181
Chapter 7 Foot Diffusion Tensor Metrics: Response to Supine Posture		190
7.1	Context of the Paper	190
7.2	Declaration Statement	191
7.3	Paper	192
7.3.1	Abstract	193
7.3.2	Introduction	195
7.3.3	Materials and Methods	197
7.3.4	Results	200
7.3.5	Discussion	201
7.3.6	References	207
Chapter 8 Conclusions and Future Directions		214
8.1	Summary of Findings	214
8.2	Contributions of this Work	218
8.3	Future Work	219

List of Figures

1.1	The structure of skeletal muscle.	4
1.2	Glycolysis and aerobic respiration are two pathways used to generate the ATP required for muscle contraction.	6
1.3	Axial slice (T1-weighted) through the calf. Shown are the muscles examined in the thesis: 1- anterior tibialis, 2- posterior tibialis, 3- soleus, 4- lateral gastrocnemius and 5- medial gastrocnemius.	11
1.4	Coronal slice (T1-weighted short axis image) through the foot. Shown are the muscles examined in the thesis: 1- quadratus plantae, 2- abductor hallucis, 3- flexor hallucis brevis, 4- flexor digitorum brevis, and 5- abductor digiti mini.	13
1.5	Typical BOLD time course from an ischemia-hyperemia paradigm of healthy subjects. Numbers show the key parameters that are commonly measured in such experiments: 1. time to half of ischemic minimum or ischemic declining slope 2. minimum signal value during ischemia 3. time between cuff deflation and maximum signal during hyperemia 4. hyperemic signal peak value 5. slope of declining portion of the curve, measured for various intervals 6. mean signal during the last few seconds of data collection.	24
2.1	A spinning charge can be thought of as a small magnet that generates a magnetic field.	38
2.2	The angle between the magnetic moment and the applied external field is defined as θ and is calculated using equation 2.6.	40
2.3	In the absence of \vec{B}_0 , the direction of the magnetic moment vectors is random. Application of a \vec{B}_0 field causes the magnetic moments for $I=1/2$ nuclei to align with or against the field at an angle of 54.74° relative to the direction of $\pm B_0$	41
2.4	For a spin-1/2 system in the presence of an external field, B_0 , the spins precess about the B_0 in one of two possible orientations: either parallel or antiparallel to the field. Although they spin with the same frequency, they are out of phase with each other (i.e. the precession is incoherent).	41

2.5	The precession frequency of the nucleus, ω_0 , also known as the Larmor frequency. For the ^1H nucleus and in a 1.5T field, $\omega_0 = 63.86$ MHz.	42
2.6	For a system with $I = 1/2$, Zeeman splitting results in two energy states, where the low energy state corresponds to the parallel orientation of the magnetic moments with the B_0 field.	44
2.7	The motion of the bulk magnetization vector following excitation is complex when viewed from a stationary frame. If viewed from a frame that rotates at ω_0 , the magnetization vector is simply <i>tipped</i> into the xy plane as a result of the RF application.	48
2.8	The magnetization vector is <i>tipped</i> through an angle of α , given by equation 2.28 due to the application of the B_1 field.	51
2.9	T_1 recovery curve.	53
2.10	T_2 decay curve	54
2.11	Pulse sequence for a spin echo along with the corresponding effect on an ensemble of spins.	59
2.12	Pulse sequence for a gradient echo along with the corresponding effect on an ensemble of spins.	60
2.13	Simplified pulse sequence diagram used to capture diffusion. The b-value depends on the interval between the two gradients, Δ , the duration, δ , and amplitude, G , of the gradients.	64
2.14	Diffusion can be isotropic (top row), where the molecule moves freely in all directions and the diffusion is modeled as a sphere. This motion occurs if the environment is unrestricted or contains random barriers. In the case of anisotropic diffusion (bottom row), the molecular motion is hindered by the presence of ordered structures, resulting in a diffusion ellipsoid.	67
2.15	Koch's curve is an example of a geometrical fractal with a dimension of 1.26189. Shown are four iterations of the curve. At each iteration, replacement of the shape in step one in place of the line segments produces the curve of the next iteration.	72

2.16 Flow chart showing the analysis steps once a signal has been determined to be fractal, according to the procedure of Eke and colleagues (Eke et al., 2000). Depending on the obtained value of $\hat{\beta}$ from the $^{low}PSD_{we}$ technique, the signal may be classified as fGn or fBm. For an fGn signal, dispersional (Disp) analysis can be used to compute the fractal dimension. For an fBm signal, the fractal dimension is calculated using the bridge detrended scaled windowed variance (bdSWV) method. If a signal falls in the middle region, signal summation conversion (SSC) has to be used to find the class of the signal and then perform the appropriate analysis. 78

4.1 Wooden footrest used to suspend the calf muscles (*arrow*). Each foot is placed on the designated spot within the footrest and an 8-channel knee coil (shown in *front* of the footrest) surrounds the thickest part of the calf of the dominant leg. 93

4.2 Axial T1-weighted image showing the calf muscles investigated in this study: anterior tibialis (ANT), posterior tibialis (POST), soleus (SOL), medial gastrocnemius (MG) and lateral gastrocnemius (LG). In the *upper corner*, a sagittal localizer is shown, from which twenty axial slices were prescribed. 98

4.3 **a** The mean of the first eigenvalue, λ_1 , for each of the five calf muscles at the three imaging sessions. *Vertical error bars* represent the standard error among subjects. *Significant reductions ($P < 0.05$) were observed between baseline (i.e. session 1) and 34 min of supine rest and between baseline and 64 min of supine rest. We did not see any measurable changes between the latter two imaging sessions. (*ANT* anterior tibialis, *POST* posterior tibialis, *SOL* soleus, *MG* medial gastrocnemius, *LG* lateral gastrocnemius). **b** The averaged second eigenvalue, λ_2 (n=10 subjects, *error bars* represent SE) for all muscle groups following 34 and 64 min of supine rest. *Significant decreases ($P < 0.05$) between baseline and 34 min of supine rest and between baseline and 64 min of supine rest were noted for all muscles. (*ANT* anterior tibialis, *POST* posterior tibialis, *SOL* soleus, *MG* medial gastrocnemius, *LG* lateral gastrocnemius). **c** The mean of the third eigenvalue, λ_3 , for each of the five calf muscles at the three imaging sessions. *Vertical error bars* represent the standard error among subjects. *Significant reductions ($P < 0.05$) were observed between baseline (i.e. session 1) and 34 min of supine rest and between baseline and 64 min of supine rest. (*ANT* anterior tibialis, *POST* posterior tibialis, *SOL* soleus, *MG* medial gastrocnemius, *LG* lateral gastrocnemius) 101

4.4 The averaged ADC (n=10 subjects, *error bars* represent SE) for all muscle groups following 34 and 64 minutes of supine rest. *Significant decreases ($P < 0.05$) between baseline and 34 minutes of supine rest and between baseline and 64 minutes of supine rest were noted for all muscles. (*ANT* anterior tibialis, *POST* posterior tibialis, *SOL* soleus, *MG* medial gastrocnemius, *LG* lateral gastrocnemius). 104

4.5 The mean FA for each of the five calf muscles at the three imaging sessions. *Vertical error bars* represent the standard error among subjects. No significant changes were observed in FA for any muscles (anterior tibialis $P=0.91$; posterior tibialis $P=0.87$; medial gastrocnemius $P=0.07$; lateral gastrocnemius $P=0.33$; soleus $P=0.31$). (*ANT* anterior tibialis, *POST* posterior tibialis, *SOL* soleus, *MG* medial gastrocnemius, *LG* lateral gastrocnemius). 105

5.1	Sample T1-weighted axial anatomical slice and the corresponding T2* weighted image.	135
5.2	Power spectral density plots of an ROI from the medial gastrocnemius muscle (top) and one from the image noise (bottom). Power law scaling relationship was observed in the muscle ROI (top) but not in the noise ROI (bottom).	137
5.3	Sample spectra of the BOLD time course from the lateral gastrocnemius ROIs. Low frequency contributions (< 0.1 Hz) dominated the spectra. Similar frequency contributions were observed in spectra from all other muscles.	139
5.4	Sample spectra of the BOLD time course from the soleus muscle of one of the subjects during the first (top), second (middle) and third (last) imaging sessions. No trend was observed when comparing spectra of various subjects (see Fig. 5.5 and Fig. 5.6).	140
5.5	Sample spectra of the BOLD time course from the soleus muscle of one of the subjects during the first (top), second (middle) and third (last) imaging sessions. No trend was observed when comparing spectra of various subjects (see Fig. 5.4 and Fig. 5.6).	141
5.6	Sample spectra of the BOLD time course from the soleus muscle of one of the subjects during the first (top), second (middle) and third (last) imaging sessions. No trend was observed when comparing spectra of various subjects (see Fig. 5.4 and Fig. 5.5).	142
6.1	Coronal (short axis) T1-weighted image showing the foot muscles that were investigated in this study: quadratus plantae (QP), abductor hallucis (AH), flexor hallucis brevis (FHB), flexor digitorum brevis (FDB), and abductor digiti mini (ADM).	171
6.2	Sample anatomical images at two slice locations (a, c) and the corresponding $b=0s/mm^2$ DTI images (b, d) of one of the subjects.	173
6.3	Sample anatomical slice (a) along with the tensor eigenvalues: λ_1 (b), λ_2 (c), and λ_3 (d) from one of the subjects.	173

6.4	The averaged fractional anisotropy, FA (n=10 subjects, error bars represent standard deviation) for each of the five muscle groups: quadratus plantae (QP), abductor hallucis (AH), flexor hallucis brevis (FHB), flexor digitorum brevis (FDB), and abductor digiti mini (ADM).	176
7.1	Sagittal localizer showing the position of the twenty coronal slices (short axis) acquired in this study. Image collection started from the neck of the talus bone.	199
7.2	Mean DT metrics in the quadratus plantae muscle at the two measurement times (error bars represent SE). We noted significant decreases ($P < 0.05$) between the first and second measurement for all DT indices, except FA. A similar pattern was observed in all other muscle groups (Table 7.1).	201

List of Tables

1.1	Some organelles in a myocyte along with their major function. . .	3
1.2	Mean percentage of type I and type II fibers in some of the skeletal muscles in the body. Data adapted from (Johnson et al., 1973) and is based on autopsy samples of young male subjects (17-30 years of age).	10
2.1	Some properties of the proton and the neutron.	36
2.2	Rules to deduce the nuclear spin, I , based on the mass and charge numbers of the nucleus of interest. Recall that the mass number is the number of nucleons (protons and neutrons) whereas the charge number is the number of protons.	37
2.3	T_1 and T_2 values of some tissues measured in humans at 3T. ¹ Data from (Gold et al., 2004) (shown are mean \pm standard deviation). ² Data from (Wansapura et al., 1999), showing mean \pm standard error. ³ Data from (Lin et al., 2001) (mean \pm standard deviation).	55
4.1	The fifteen gradient directions used in the DTI acquisition	95
4.2	Baseline eigenvalues and ADC (mean \pm SE $\times 10^{-3}$ mm ² /s; n=10 subjects) for all muscle groups and % decrease in baseline value following 34 and 64 min of supine rest	103
5.1	BOLD signal was evaluated in 2400 serially acquired images (4 per second) over 10 minutes. Mean temporal BOLD signal intensity (SI, in arbitrary units) and standard deviation (SD), over the 10-minute scan are shown. The three measurements represent the data from each of the three imaging sessions, separated by 30 minutes of supine rest. Values for each measurement are mean \pm SE averaged over all subjects (n=10). Statistical analysis revealed that any observed variations between imaging sessions were random or due to chance ($P > 0.05$).	136

5.2	Fractal dimension of the BOLD signal in the various muscles. The three measurements represent the data from each of the three imaging sessions, separated by 30 minutes of supine rest. Values for each measurement are mean \pm SE averaged over all subjects (n=10). No significant differences were observed between the three measurements for any of the muscle groups (anterior tibialis P=0.35; posterior tibialis P=0.23; medial gastrocnemius P=0.11; lateral gastrocnemius P=0.58; soleus P=0.10).	138
6.1	DTI eigenvalues ($\lambda_1, \lambda_2, \lambda_3$) and apparent diffusion coefficient (ADC) for muscles in the foot (mean \pm SD). Units of eigenvalues and ADC are expressed as $\times 10^{-3}$ mm ² /s.	174
6.2	Statistical analysis (repeated measured analysis of variance (ANOVA) with Tukey honestly significant difference (HSD) post hoc test) between pairs of muscle groups for DTI metrics. * Statistical significance defined at P < 0.05 between muscles. QP= quadratus plantae, AH= abductor hallucis, FHB= flexor hallucis brevis, FDB= flexor digitorum brevis, and ADM= abductor digiti mini.	175
6.3	The measured signal to noise ratio (SNR) for each of the investigated foot muscles. Values shown are mean \pm SD averaged over all subjects (n=10). SNR was calculated using the difference method (38) as given by Equation 6.1.	177
7.1	Mean of eigenvalues, ADC and FA for the two measurement times in each of the five muscles (n= 9 subjects; mean \pm SE; eigenvalues and ADC are $\times 10^{-3}$ mm ² /s). Significant decreases (P < 0.05) were observed between the first and second measurement for all DT indices (Table 7.2), except the FA.	202
7.2	% decrease in the DT metrics that showed significant differences between the two measurement time. Data are mean \pm SE. . .	203

List of Notations and Abbreviations

α	Flip angle
ADC	Apparent diffusion coefficient
ADM	Abductor digiti mini muscle
AH	Abductor hallucis muscle
ANOVA	Analysis of variance
ANT	Anterior tibialis muscle
ATP	Adenosine triphosphate
BOLD	Blood oxygen level dependent
CSA	Cross sectional area
CT	Computed tomography
DeoxyHb	Deoxyhemoglobin
Disp	Dispersional
DTI	Diffusion tensor imaging
DWI	Diffusion weighted imaging
EEG	Electroencephalography
EPI	Echo planar imaging
ETL	Echo train length
FA	Fractional anisotropy
FD	Fractal dimension
FDB	Flexor digitorum brevis muscle
FHB	Flexor hallucis brevis muscle
FID	Free induction decay
fMRI	Functional magnetic resonance imaging
FOV	Field of view
FSE	Fast spin echo
FSL	FMRIB's software library
GE	General Electric
GPA	Granulomatosis with polyangiitis
GRE	Gradient recalled echo
<i>H</i>	Hurst exponent
HSD	Honestly significant difference
LG	Lateral gastrocnemius muscle
MD	Mean diffusivity
MG	Medial gastrocnemius muscle
MR	Magnetic resonance
MRI	Magnetic resonance imaging
NEX	Number of excitations

NMR	Nuclear magnetic resonance
OxyHb	Oxyhemoglobin
PAOD	Peripheral arterial occlusive disease
PCr	Phosphocreatine
POST	Posterior tibialis muscle
PSD	Power spectral density
QP	Quadratus plantae muscle
RF	Radiofrequency
ROI	Region of interest
SD	Standard deviation
SE	Standard error
SNR	Signal to noise ratio
SOL	Soleus muscle
SSC	Signal summation conversion
SSc	Systemic sclerosis
T	Tesla
T_1	Longitudinal relaxation parameter
T_2	Transverse relaxation parameter
T_2^*	Transverse relaxation parameter (effective)
T_E	Echo time
T_R	Repetition time
bdSWV	bridge detrended scaled windowed variance
fBm	Fractional Brownian motion
fGn	Fractional Gaussian noise
min	Minute
ml	Milliliter
s	Second

Thesis Format

This thesis has been written in the “sandwich format”, as described in the “guide for the preparation of theses” by the school of graduate studies. It contains four original research papers (chapters 4- 7) preceded by a general introduction (chapters 1- 3) and followed by a general conclusion (chapter 8). Chapter 4 has been accepted for publication in *Magnetic Resonance Materials in Physics, Biology and Medicine (Magn Reson Mater Phy)*. Chapter 6 has been accepted for publication in *Journal of Computed Assisted Tomography (JCAT)*. The remaining two chapters (5 and 7) are manuscripts that have been prepared in final format for submission to physiology journals.

Chapter 1

Introduction

In the past decade, researchers have demonstrated a lot of interest in the non-invasive evaluation of skeletal muscle using MR imaging techniques that examine microstructure (diffusion tensor imaging, DTI) and oxygenation (blood oxygen-level dependent (BOLD) imaging). By probing the diffusion of water molecules within an imaged region, DTI can give information about the underlying tissue architecture. The technique has been used to gain insight into skeletal muscles in various regions (Galbán et al., 2004; Froeling et al., 2010; Sinha et al., 2011; Jones et al., 2013) since skeletal muscle fibers have an anisotropic structure. BOLD imaging, on the other hand, allows for the evaluation of skeletal muscle function by probing tissue oxygenation (Jacobi et al., 2012). The technique has been used for over a decade to investigate muscle microvasculature both in healthy (Noseworthy et al., 2003; Meyer et al., 2004; klarhofer et al., 2008) and diseased (Ledermann et al., 2006a; Partovi et al., 2012) populations. This chapter gives a brief description of skeletal muscles and then reviews the current knowledge regarding DTI and BOLD imaging of skeletal muscles, focusing on the lower limb.

1.1 Skeletal Muscles

Skeletal muscles are tissues that are attached to bones via tendons. They are responsible for the voluntary movement of the body due to their contractile properties. Skeletal muscles are also important for maintaining posture and performing daily tasks.

1.1.1 Muscle Structure

The basic unit of a skeletal muscle is the muscle cell, which is also known as a muscle fiber or a myocyte. Muscle fibers have diameters that range from 10 to 120 μm (Exeter and Connell, 2010) and are typically 2 to 10 cm long (Galbán et al., 2004). The sarcolemma is the plasma membrane that encloses a muscle fiber and regulates the passage of molecules between the intracellular and extracellular compartment (Exeter and Connell, 2010). Each muscle fiber is multinucleated and like any other cell, a myocyte contains essential organelles as listed in table 1.1. These include the mitochondria, where energy production takes place, and the sarcoplasmic reticulum, which facilitates molecular transport due to its tubular network. A muscle fiber also has another set of channels, known as the transverse tubules. These are infoldings of the sarcolemma and they contain extracellular fluid (Exeter and Connell, 2010).

Organelle	Function
Nucleus	Controls the activities of the cell as it contains the genetic material
Mitochondria	Produces energy
Myofibril	Contains contractile units
Sarcoplasmic reticulum	Allows for substances to be transported via its tubular network and its vesicles
Transverse tubule	Allows for substances to be transported via its tubular network

Table 1.1: Some organelles in a myocyte along with their major function.

The contractile properties of a muscle arise from the myofibril, which is made up of subunits referred to as sarcomeres. Each sarcomere is composed of two filaments: thick myosin filaments and thin actin filaments that form the area between two Z lines (Exeter and Connell, 2010). The M line divides the sarcomere in half. The A band refers to the region where the myosin and actin overlap. The H zone is the smaller central region containing myosin only, while the I band is the outer region containing actin only (figure 1.1). The sarcoplasmic reticulum runs parallel to a myofibril and the T tubules run perpendicular to the direction of the myofibril. Each muscle fiber is enclosed by an endomysium. The grouping of adjacent muscle fibers results in a bundle known as a fascicle, which is surrounded by a perimysium (Exeter and Connell, 2010). The muscle is the binding of fascicles by a connective tissue known as the epimysium (figure 1.1).

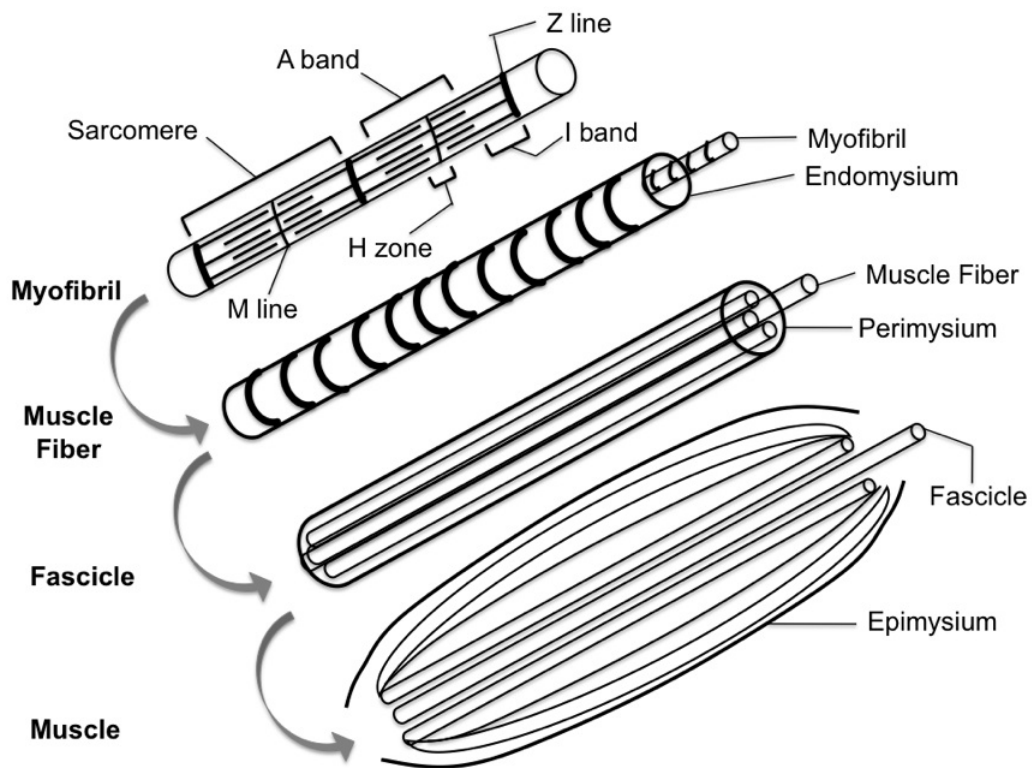


Figure 1.1: The structure of skeletal muscle.

1.1.2 Muscle Contraction

Muscle contraction begins when a motor neuron releases a neurotransmitter in response to a nerve impulse. After crossing the neuromuscular junction, the neurotransmitter binds to receptors on the sarcolemma. This initiates a cascade of events involving sodium and potassium channels that lead to the conduction of a muscle impulse. The impulse moves through the T tubules and reaches the sarcoplasmic reticulum, where it results in the release of calcium ions. This exposes binding sites on the actin filaments, thereby beginning the muscle contraction cycle, which follows a sliding filament model (Exeter and Connell, 2010). Briefly, myosin cross-bridges attach to binding sites on the actin filament. The bending of the myosin results in the movement of the actin filaments. Release of the myosin head and repetition of the process shortens the sarcomere and the muscle contracts. Muscle contraction requires the presence of energy in the form of adenosine triphosphate (ATP).

Although ATP is present in the muscle fiber, the stored supply is only enough to sustain contractions for a very short time (on the order of 3 to 6 seconds). Once the initial supply is depleted, the muscle must quickly regenerate ATP. There are three pathways in which ATP is synthesized: the first involves phosphocreatine (PCr or creatine phosphate), the second relies on anaerobic glycolysis and the third uses aerobic respiration (Shier et al., 2006).

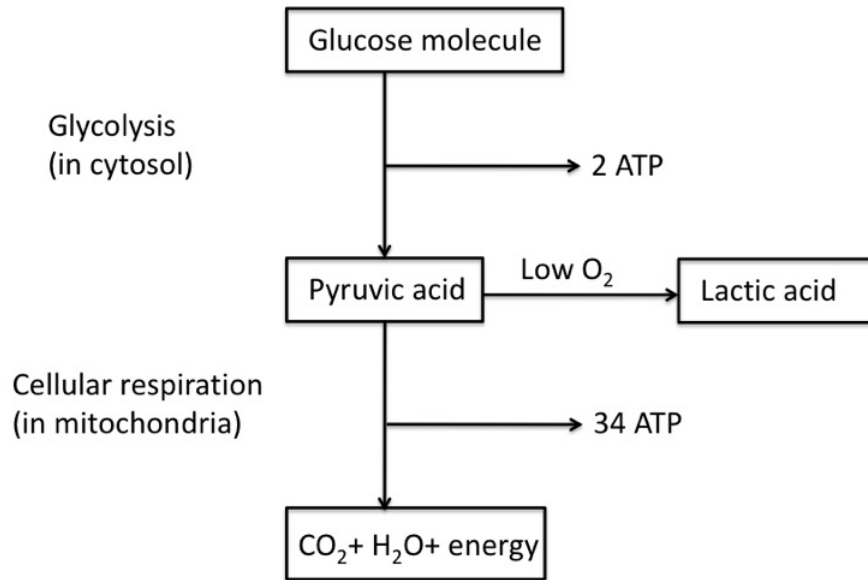


Figure 1.2: Glycolysis and aerobic respiration are two pathways used to generate the ATP required for muscle contraction.

In the first pathway that involves PCr, adenosine diphosphate (ADP) is converted into adenosine triphosphate (ATP) when PCr gives up one of its phosphate groups, in the presence of the creatine phosphokinase enzyme (Shier et al., 2006). This is an anaerobic pathway, which means that it does not require oxygen to be present. Since muscle fibers do not have a very large supply of PCr, this pathway is short lived (resulting in about 5 to 15 seconds of activity). Once PCr is exhausted, glycolysis and cellular respiration are used to generate ATP (figure 1.2).

Glycolysis occurs in the cytosol and can take place when oxygen is not present. In glycolysis, a glucose molecule is broken down into pyruvic acid and 2 ATP molecules are synthesized. If oxygen supply remains low, pyruvic acid produces lactic acid, which may accumulate in the muscle. This anaerobic pathway provides enough energy to sustain exercise for about 40 to 60 seconds.

The final pathway, or cellular respiration, takes place in the mitochondria and requires oxygen to be present in order to produce ATP. The oxygen can come from hemoglobin or myoglobin, which are proteins that bind to oxygen and that are found in red blood cells and muscle cells, respectively. In this pathway, pyruvic acid undergoes numerous complex reactions that result in the production of water, carbon dioxide and 34 ATP molecules. This pathway can be used to supply energy for a long time (on the order of hours).

The pathway used to produce ATP depends on the type of exercise being performed. If the exercise requires a quick burst of energy for a short period of time (high intensity, short term exercise, such as weightlifting), then creatine phosphate and anaerobic glycolysis are the pathways used to provide the needed energy. If, on the other hand, endurance exercise (low to moderate intensity, long term exercise) is being performed, then aerobic respiration will provide the required energy to sustain muscle activity after the other two pathways have been used up.

There are a few ways in which muscles contract. If a muscle shortens as it generates force, as the biceps do when lifting a weight during a curl, then the contraction is referred to as a concentric or isotonic contraction (Exeter and Connell, 2010). If the muscle does not change its length, as the arm muscles do when an object is being carried in front of the carrier, then the contraction is referred to as an isometric contraction. Finally, if the muscles lengthen while producing the force, as the biceps do when lowering a weight during a curl, then the contraction is referred to as an eccentric contraction (Exeter and Connell, 2010).

1.1.3 Muscle Fibers

Muscle fibers are generally divided into two categories: slow twitch (type I) and fast twitch (type II). The fast twitch fibers are further broken down into type IIa (fast oxidative/glycolytic) and IIx (fast glycolytic)(Exeter and Connell, 2010). The distinction between *slow* and *fast* is based on the time it takes the fiber to contract. Slow twitch fibers take longer to contract (110 ms) than do fast twitch fibers (50 ms) (Exeter and Connell, 2010). The former are also fatigue resistant as they rely on aerobic metabolism. That is why type I fibers are sometimes referred to as slow oxidative fibers. These fibers are rich in mitochondria and have extensive capillary networks to support the oxygen delivery needed to sustain aerobic respiration (Shier et al., 2006).

They are also sometimes referred to as red fibers (Galbán et al., 2004) because they contain large amounts of myoglobin, which gives muscle a reddish-brown color (Shier et al., 2006). Type I fibers are used in endurance type activities that are of low to moderate intensity such as marathon running because they are fatigue resistance and can thus support prolonged exercise.

Type II fibers use anaerobic metabolism to generate ATP. They are able to contract quickly, but at the same time, they fatigue quickly. They are larger than type I fibers (Exeter and Connell, 2010). Fast twitch fibers are sometimes referred to as white fibers (Galbán et al., 2004) because they do not contain large amounts of myoglobin. Type IIx fibers (glycolytic) are used in exercises that require a quick burst of energy for a short period of time, such as weightlifting or sprinting. Type IIa fibers (oxidative/glycolytic) use both anaerobic and aerobic metabolism and are thus used in activities such as middle distance running (Exeter and Connell, 2010).

Human skeletal muscles are made up of both type I and type II fibers and in general, there is an equal proportion of these two types in most skeletal muscles in the body of an untrained, healthy adult individual (Exeter and Connell, 2010; Johnson et al., 1973). However, there are a few muscles that show predominance of one type of fiber over another as shown in table 1.2 (Johnson et al., 1973). The orbicularis oculi is one of the muscles of the eye

Muscle	% of Type I fibers	% of Type II fibers
Abductor digiti mini (foot)	51.8	48.2
Flexor digitorum brevis (foot)	44.5	55.5
Gastrocnemius (calf, lateral head surface)	43.5	56.5
Gastrocnemius (calf, lateral head deep)	50.3	49.7
Gastrocnemius (calf, medial head)	50.8	49.2
Soleus (calf, surface)	86.4	13.6
Soleus (calf, deep)	89.0	11.0
Tibialis anterior (calf, surface)	73.4	26.6
Tibialis anterior (calf, deep)	72.7	27.3
Orbicularis oculi (eye)	15.4	84.6
Vastus lateralis (thigh, deep)	46.9	53.1
Vastus medialis (thigh, deep)	61.5	38.5

Table 1.2: Mean percentage of type I and type II fibers in some of the skeletal muscles in the body. Data adapted from (Johnson et al., 1973) and is based on autopsy samples of young male subjects (17-30 years of age).

and it controls blinking. As such, it has a high proportion of type II fibers to support the act of blinking, which requires a short burst of energy. The soleus and tibialis anterior muscles, on the other hand, are involved in maintaining posture and thus contain a higher proportion of type I fibers so they can provide low amounts of energy for long periods of time. It has been shown that different types of training exercises may change the proportion of muscle fibers in the trained muscles (Exeter and Connell, 2010).

1.1.4 Muscles of the Lower Limb

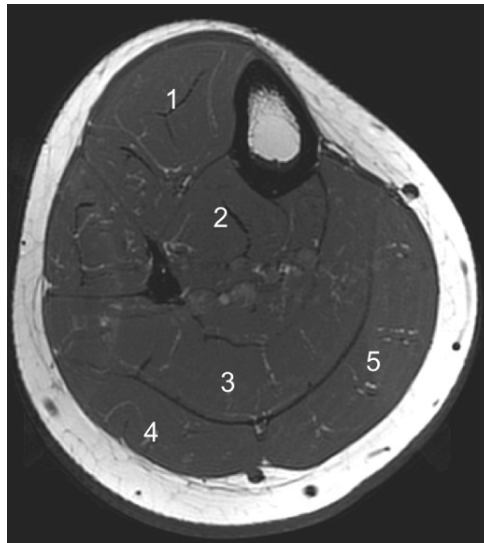


Figure 1.3: Axial slice (T1-weighted) through the calf. Shown are the muscles examined in the thesis: 1- anterior tibialis, 2- posterior tibialis, 3- soleus, 4- lateral gastrocnemius and 5- medial gastrocnemius.

Muscles of the lower limb, specifically those in the calf and foot region, were examined in the thesis. The calf muscles that were assessed are the anterior tibialis (also known as the tibialis anterior), the posterior tibialis (or tibialis posterior), the soleus and the medial and lateral gastrocnemius (figure 1.3). The anterior tibialis is located at the front of the leg and is involved in dorsiflexion (bending the foot up towards the shin) and inversion (twisting the foot so that the sole faces the medial part of the body) of the foot (Shier et al., 2006). The posterior tibialis muscle is involved in plantar flexion (opposite of dorsiflexion) and inversion of the foot. The triceps surae refers to the three

muscles located in the posterior compartment of the calf (the back of the leg). These are the soleus and the two heads of the gastrocnemius. The triceps surae muscles are also involved in plantar flexion of the foot.

The foot muscles that were examined in the thesis are the quadratus plantae muscle, the abductor hallucis muscle, the flexor hallucis brevis muscle, the flexor digitorum brevis muscle and the abductor digiti mini muscle (figure 1.4). The abductor hallucis muscle and the abductor digiti mini muscle are found on the medial and lateral sides of the foot, respectively. They are involved in the abduction (movement of digits away from the centerline of the foot) of the small toe (the abductor digiti mini muscle) and the big toe (the abductor hallucis muscle). The flexor digitorum brevis muscle is found in the middle portion of the sole of the foot, between the abductor digiti mini muscle and the abductor hallucis muscle. It is involved in the flexion of the middle three toes. The flexor hallucis brevis muscle is also found in the sole of the foot, between the flexor digitorum brevis muscle and the abductor hallucis muscle. It is involved in the flexion of the big toe. Finally, the quadratus plantae muscle is found in the intermediate layer of the foot sole, deep to the flexor digitorum brevis muscle. It is involved in the flexion of the four lateral toes.



Figure 1.4: Coronal slice (T1-weighted short axis image) through the foot. Shown are the muscles examined in the thesis: 1- quadratus plantae, 2- abductor hallucis, 3- flexor hallucis brevis, 4- flexor digitorum brevis, and 5- abductor digiti mini.

1.2 Diffusion Tensor Imaging of Skeletal Muscles

Diffusion imaging assesses the displacement of water molecules in an investigated region of interest. When molecules move in an unrestricted environment, the resulting displacement is isotropic (Bihan et al., 2001). In muscle fibers or other systems that show ordered orientations, anisotropic diffusion is evident, since the motion of water molecules is constrained by barriers. In such a case, the diffusive movement of water molecules along the myofiber's axis is much easier and greater diffusion is seen along this axis than that observed along the transverse direction.

Following early applications of diffusion imaging to investigate skeletal muscles in vitro (Basser et al., 1994), the technique has become a promising imaging tool, enabling researchers to gain insight about muscle microstructure in vivo. DTI studies have now been applied to examine a wide range of skeletal muscles in the body. These include muscles of the forearm (Froeling et al., 2010), the lumbar (Jones et al., 2013), the thigh (Budzik et al., 2007; Qi et al., 2008; Kan et al., 2009; Gondin et al., 2010; Cermak et al., 2012) and the calf (Sinha and Yao, 2002; Galbán et al., 2004; Zaraiskaya et al., 2006; Galbán et al., 2005, 2007; Heemskerk et al., 2010; Sinha and Sinha, 2011).

The diffusion of water within a given region can be described using various indices. Eigenvalues (λ_1 , λ_2 and λ_3) and eigenvectors provide information about the magnitude and direction of the diffusion, respectively (refer to section 2.2 for the technical DTI details). The principle eigenvalue, λ_1 , characterizes the diffusion along the axis of the muscle fiber. However, no conclusion has been reached when it comes to the meaning of the two remaining eigenvalues. In one study, it was suggested that λ_2 could represent diffusion along sheets of fibers, while λ_3 might characterize the diffusion within muscle fiber cross-section (Galbán et al., 2004). It has been shown that the diffusive properties of the calf muscles differ between the various muscle groups (Galbán et al., 2004; Sinha et al., 2006) presumably due to differing muscle architec-

ture (Galbán et al., 2004). The observed differences between calf muscles in terms of the measured DTI parameters have been attributed to the function of the specific muscle with regards to foot action. As such, water diffusivity of muscles involved in foot extension (soleus, medial and lateral gastrocnemius muscles) appeared to be statistically different from that of adjacent calf muscles involved in other foot actions (Galbán et al., 2004). The apparent diffusion coefficient (ADC), which is also referred to as the mean diffusivity (MD), is a measure of the mean of the three eigenvalues. Fractional anisotropy (FA) is another DTI metric that conveys information about the appearance of the diffusion ellipsoid. It takes values between zero and one. An FA of zero represents perfectly isotropic diffusion, as in the case of a sphere. An FA of one represents perfect anisotropic diffusion.

Numerous DTI studies have set out to investigate whether differences exist in water diffusion in skeletal muscles of people of different age, gender or physical characteristics such as weight and height (Galbán et al., 2005, 2007; Okamoto et al., 2010; Kermarrec et al., 2010; Jones et al., 2013). Age related changes were observed in the eigenvalues of the plantar flexor muscles (soleus, medial and lateral gastrocnemius) between young (< 46.4 years of age) and old (≥ 46.4 years of age) subjects in one study (Galbán et al., 2007). The reported reduction of approximately 7% in the eigenvalues of the plantar

flexors was attributed to the reduction in the size of the fiber that accompanies aging, which would result in more restricted diffusion in the older population (Galbán et al., 2007). The group also found a decrease of approximately 10% in the FA of the anterior tibialis muscle in the older subjects, with the reduction mostly due to the variation in λ_3 of that muscle between young and old subjects. Although the group reported strong correlations between the various DTI metrics in calf muscles such that the parameters tended to decrease with age, no correlations were found between height, weight or body mass index and the DTI indices (Galbán et al., 2007).

While Galban and colleagues demonstrated the dependence of diffusivity measures on age (Galbán et al., 2007), others looking at fiber tractography visualization in the calf (Okamoto et al., 2010), DTI metrics in the thigh (Kermarrec et al., 2010) or DTI indices in the lower back musculature (Jones et al., 2013) failed to establish correlations with aging. With regards to gender differences, literature observations are mixed, with some studies demonstrating differences in water diffusion (Galbán et al., 2005) and tractography visualization of fibers (Okamoto et al., 2010) between the sexes, while others failing to demonstrate any differences (Kermarrec et al., 2010; Jones et al., 2013). In the studies that show differences between males and females, the eigenvalues and ADC are generally higher in females than in males, while the FA is

generally lower in females (Galbán et al., 2005). In addition, the differences in the DTI metrics between the sexes range from approximately 2%-13% for the various metrics and calf muscle groups (Galbán et al., 2005). The source of the observed gender-related differences in DTI metrics is not clear (Galbán et al., 2005).

Besides studies that assess muscle structure and architecture in healthy subjects, diffusion imaging has also been applied to evaluate muscle injuries and pathologies (Zaraiskaya et al., 2006; Heemskerk et al., 2006, 2007; Qi et al., 2008). In injured calf muscles, where the injury is a muscle tear or an intramuscular hematoma, increases in the eigenvalues and ADC have been reported, with reductions in the FA, in comparison to healthy calf muscles (Zaraiskaya et al., 2006). The observed differences in the DTI metrics between healthy and injured calf muscles were approximately 30%- 60% for the various parameters (Zaraiskaya et al., 2006). The diffusive changes that accompany muscle lesions were presumed to stem from modifications of muscle microstructure that accompany muscle injury (Zaraiskaya et al., 2006). The structural abnormalities associated with the injury were also evident when muscle fibers were tracked in the damaged muscle regions (Zaraiskaya et al., 2006).

Diffusion imaging has been shown to be capable of monitoring skeletal muscle injury following ischemic damage (Heemskerk et al., 2006, 2007).

Ischemia induced by fifty minutes of occlusion of mouse hindlimb was accompanied by a decrease in ADC of approximately 15% in the tibialis anterior muscle, while no change was observed in the gastrocnemius muscle (Heemskerk et al., 2006). During reperfusion, the ADC increased in both muscles, however, although it renormalized to its initial values in the tibialis anterior after twenty-four hours, it remained enhanced in the gastrocnemius muscle following twenty-four hours (Heemskerk et al., 2006). The reason behind the nonuniform changes observed between the muscle groups was attributed to the differences in fiber composition of the two muscles. Similar observations have been found in another study tracking ischemic skeletal muscle injury and repair using DTI (Heemskerk et al., 2007).

Diffusion imaging has also been used in evaluating muscle myopathies and tracking disease progression. In inflammatory myopathies, higher diffusivity values are obtained in the inflamed muscle compared to healthy muscles, with a 24% increase in the diffusivity of the inflamed muscle (Qi et al., 2008). This is likely due to the expansion of the extracellular space that accompanies the inflammatory state, resulting in greater diffusion (Qi et al., 2008). Severe fat infiltration results in the reduction of the water content in the muscle and as such, reductions in diffusivity of approximately 30% are observed in fat-infiltrated muscles compared to unaffected muscles (Qi et al., 2008).

Numerous studies have examined the diffusion metrics following changes in muscle microstructure due to various ankle positions (Deux et al., 2008; Hatakenaka et al., 2008; Schwenzer et al., 2009; Okamoto et al., 2010; Sinha and Sinha, 2011; Sinha et al., 2011). Compared to plantarflexion, dorsiflexion resulted in an increase in λ_2 and λ_3 of the anterior tibialis muscle with an accompanying increase in the mean diffusivity and a decrease in the fractional anisotropy in one study (Schwenzer et al., 2009). The opposite diffusional effect was observed in the antagonist muscles. In another study, increases were seen in λ_1 with plantar flexion and no changes were reported in λ_3 in the medial gastrocnemius muscle (Okamoto et al., 2010). Although the sources of discrepancies between the studies are not clear, it is evident from all evaluations that muscle fiber architecture affects the measured DTI indices.

Since the DTI metrics have been shown to be sensitive to subtle microstructural changes in skeletal muscles, it is not surprising that the application of external pressure to calf muscles would result in observable changes in the various DTI parameters (Hata et al., 2012). In one study that applied pressure using a cuff and measured the DTI indices in the soleus and anterior tibialis muscles at varying levels of pressure (0, 100 and 200 mmHg), significant increases were observed in the FA with the increase in pressure (Hata et al., 2012). These increases were approximately 8% in the anterior tibialis muscle

and 17% in the soleus muscle at 200 mmHg compared to baseline. Significant reductions, on the order of 8% compared to baseline, were also observed in λ_3 with pressure application (Hata et al., 2012).

Changes in diffusion indices of skeletal muscles have also been reported following exercise (Okamoto et al., 2008; Yanagisawa et al., 2009; Cermak et al., 2012). In one study that involved unilateral exercise of the right calf by plantar flexion and dorsiflexion of the foot, significant decreases were observed in the FA in the soleus and gastrocnemius muscles of the exercise-loaded leg following the exercise (Okamoto et al., 2008). It was also observed that the FA took seventy-two hours to recover to baseline following the exercise in the subject that was loaded for thirty minutes, while it took one week to recover in the subject that had a stronger loading (sixty minutes of exercise) (Okamoto et al., 2008). Another study explored the use of DTI to detect microstructural changes in the vastus lateralis muscle following strenuous unaccustomed exercise (Cermak et al., 2012). The group observed that the FA values decreased twenty-four hours after the exercise, while the ADC values increased post-exercise compared to the baseline measurements (Cermak et al., 2012). These changes were suggested to reflect a more disorganized fiber geometry due to the exercise induced muscle damage (Cermak et al., 2012). An increase in ADC has also been reported following exercise by another group of

researchers (Yanagisawa et al., 2009). Besides studying the effects of exercise on water diffusion, the group also investigated the effect of cooling skeletal muscles using diffusion imaging (Yanagisawa et al., 2009). They reported a decrease in ADC with muscle cooling (Yanagisawa et al., 2009).

1.3 Blood Oxygen-Level Dependent Imaging of Skeletal Muscles

For over a decade, researchers have tried to gain insight into skeletal muscle function by probing tissue oxygenation using BOLD contrast (Partovi et al., 2012; Jacobi et al., 2012; Noseworthy et al., 2003, 2010). The BOLD signal within a region is related to the ratio of oxyhemoglobin (oxyHb) to deoxyhemoglobin (deoxyHb). Changes in tissue oxygenation result in changes in local signal dephasing, detected using gradient echo T2* weighted images (refer to section 2.3 for BOLD imaging details).

Most BOLD muscle examinations involve the use of a stimulus or a paradigm to perturb the blood oxygenation status within the muscle and induce a measurable change in the detected BOLD signal (Partovi et al., 2012). Assessment of the BOLD time course by evaluating the various characteristics of the BOLD signal, such as the time it takes the signal to peak after the paradigm or the maximal BOLD signal reached, provide insight into muscle

microcirculation and its functional status. To date, various paradigms have been used to provoke changes in the local ratio of oxyHb to deoxyHb in skeletal muscle. These include ischemia induced by cuff compression (Lebon et al., 1998; Ledermann et al., 2006,b; Duteil et al., 2006; Schulte et al., 2008; Kos et al., 2009; Sanchez et al., 2010; Partovi et al., 2012), electrical stimulation (Jordan et al., 2004), exercise challenges (Meyer et al., 2004; Jordan et al., 2004; Wigmore et al., 2004; Bulte et al., 2006; Damon et al., 2007), and the intake of vasoactive substances (Bulte et al., 2006). Of the various paradigms used to perturb muscle oxygenation, the cuff compression protocol is one of the earliest used techniques to assess the muscle BOLD effect (Lebon et al., 1998).

In ischemia-reactive hyperemia protocols, a cuff is used to compress the leg at the mid thigh region, thereby temporary occluding blood supply to the lower leg (Partovi et al., 2012). Such paradigms usually require subjects to lay in the supine position for five to fifteen minutes before the examination begins (Partovi et al., 2012, 2013). This is because venous filling and draining have been shown to influence the BOLD response in ischemia-hyperemia paradigms (Duteil et al., 2006). Specifically, vascular filling, induced by dangling the leg for a period of twenty minutes, results in a higher BOLD signal intensity compared with vascular draining or a standard supine position (Duteil et al.,

2006). Thus, since the BOLD contrast during reactive hyperemia is affected by the degree of vascular filling, most ischemia-hyperemia protocols require a resting period before beginning data collection.

A typical paradigm involving cuff compression begins with one minute of rest, followed by fast cuff inflation to produce leg ischemia, which lasts anywhere from three to six minutes (Partovi et al., 2013, 2012). Cuff deflation then results in reactive hyperemia/ post occlusive recovery. To characterize the BOLD time course of the various calf muscles from such experiments, numerous parameters have been used (Jacobi et al., 2012; Partovi et al., 2012) . For the ischemic portion of the curve (figure 1.5), the minimal BOLD signal during ischemia, the time to half of the ischemic minimum and the ischemic declining slope have been measured to characterize the ischemic period of the paradigm. The hyperemic portion of the curve (figure 1.5) has been studied by measuring the peak BOLD signal during hyperemia, the time it takes the BOLD signal to reach its maximal value following cuff deflation (time to peak), the hyperemic declining slope and the mean BOLD signal during the last few seconds of data collection (end value) (Jacobi et al., 2012; Partovi et al., 2012). These parameters have been mostly manually determined from the signal intensity time course by an operator and no standard methods were used to measure these values. However, recently, a fitting algorithm has been developed to

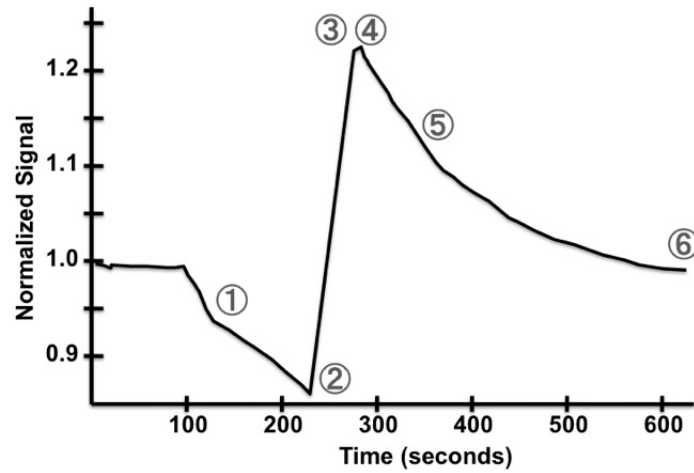


Figure 1.5: Typical BOLD time course from an ischemia-hyperemia paradigm of healthy subjects. Numbers show the key parameters that are commonly measured in such experiments: 1. time to half of ischemic minimum or ischemic declining slope 2. minimum signal value during ischemia 3. time between cuff deflation and maximum signal during hyperemia 4. hyperemic signal peak value 5. slope of declining portion of the curve, measured for various intervals 6. mean signal during the last few seconds of data collection.

model the reactive hyperemia portion of the curve based on a gamma variate and a sigmoidal function (Schewzow et al., 2012).

The ischemia-hyperemia technique has been used to understand the effects of aging (Schulte et al., 2008; Kos et al., 2009) and to assess patients with various diseases, including peripheral arterial occlusive disease (Ledermann et al., 2006b; Potthast et al., 2009; Huegli et al., 2009), systemic sclerosis (Partovi et al., 2012, 2013) and granulomatosis with polyangiitis (Jacobi et al., 2013). With regards to aging, notable differences have been observed between

the BOLD signal of young volunteers (30.3 ± 6.5 years) and elderly subjects (64 ± 6.4 years) (Schulte et al., 2008). These include a reduced hyperemic peak value in the elderly, which peaks quickly and has a higher end value reflecting a slower declining signal (Schulte et al., 2008). Another study also found a reduced minimum ischemic signal in the elderly (Kos et al., 2009). The observed differences in the BOLD time course of young and older subjects are presumed to stem from more rigid vessel walls and reduced capillary density that accompany aging (Schulte et al., 2008).

Peripheral arterial occlusive disease (PAOD) is characterized by a decrease in blood flow to the limb due to occlusions in the arteries of the extremity (Ledermann et al., 2006b). This results in impaired perfusion to the dependent musculature. To gain insight into micro-circulation and muscle oxygenation status of sufferers from PAOD, the ischemia-hyperemia BOLD paradigm has been applied with notable differences observed between healthy controls and PAOD patients (Ledermann et al., 2006b; Potthast et al., 2009). Both healthy and diseased subjects show an initial exponential decrease of the BOLD signal due to cuff inflation (Potthast et al., 2009). However, unlike the continuous decrease in $T2^*$ of the control group over the full ischemic period, the PAOD muscle BOLD signal seems to decrease more slowly and stabilize after the initial rapid reduction, resulting in a lower $T2^*$ end value in PAOD

patients (Potthast et al., 2009). The observed differences between the two groups during the ischemic portion have been attributed to a reduced oxygen consumption (Potthast et al., 2009), likely stemming from the various muscle alterations (reduced capillary density or metabolic changes) that accompany PAOD (Ledermann et al., 2006b). Post-ischemia, PAOD patients show a decreased hyperemic peak that takes longer to peak (Ledermann et al., 2006b). The reduced time to peak of the $T2^*$ signal is presumed to arise from the lack of inflow of freshly oxygenated blood (Ledermann et al., 2006b). With regards to PAOD, the ischemia BOLD paradigm has also been applied to assess the gastrocnemius muscle one day before and six weeks following percutaneous transluminal angioplasty of the femoral artery (Huegli et al., 2009). Since stenosis treatment improves circulation, evaluations of the BOLD response of the muscle could be useful in assessing treatment success (Huegli et al., 2009). It was noted that post intervention, the BOLD signal of PAOD patients shows an increase in the hyperemic peak value and a decrease in the time that the signal takes to peak (Huegli et al., 2009). Thus, the angioplasty treatment tended to shift the BOLD signal parameters towards those of healthy volunteers (Jacobi et al., 2012), although the observed changes with the intervention did not reach significance but did demonstrate a hemodynamic change (Huegli et al., 2009).

Systemic sclerosis (SSc) involves damage to the endothelium (cells that line vessel walls) and vessel modifications leading to impairments in small blood vessels (Partovi et al., 2012). The ischemia-hyperemia BOLD paradigm has been used to probe skeletal muscle micro circulation in SSc sufferers and notable differences were observed between healthy subjects and SSc patients (Partovi et al., 2012). These include a reduced minimum ischemic signal, longer time to peak and a decreased hyperemic peak value in the SSc subjects in comparison to healthy controls (Partovi et al., 2012). The observed differences in the BOLD time course are likely due to precapillary occlusion, reduced capillary density or reduced vasodilator reserve in SSc patients (Partovi et al., 2012).

Recently, in a case study looking at calf BOLD response of a patient suffering from granulomatosis with polyangiitis (GPA) (an inflammation of small vessels), alterations were observed in the BOLD signal time course of the GPA patient when compared to a healthy subject (Jacobi et al., 2013). These included a reduced minimum ischemic signal, lower hyperemic peak signal and a higher end value reflecting slower decline of the signal in the GPA patient (Jacobi et al., 2013). The observed signal modifications were speculated to stem from a decreased flow in muscle microvessels and higher

oxygen consumption in the GPA patient, leading to a reduced hyperemic peak and a lower minimum ischemic signal, respectively (Jacobi et al., 2013).

Although most studies that use the ischemia-hyperemia protocol have been performed in the calf region, extension of the technique to examine muscles in the foot region has been recently explored (klarhofer et al., 2008; Kos et al., 2009). Compared to the soleus muscle, the adductor hallucis muscle in the foot showed a lower signal change during reactive hyperemia and this change was observed to occur over a longer time interval in healthy subjects (klarhofer et al., 2008). In addition, comparisons of the BOLD response of foot muscles in young (26.1 ± 3.9 years) and old (69.0 ± 7.4 years) subjects revealed that the minimum ischemic value was lower in the older subjects and that the signal took longer to peak in this group, reaching a lower hyperemic peak value compared to young subjects (Kos et al., 2009). The noted differences were attributed to stem from modifications in reserve capacity with aging, leading to quicker deoxygenation during ischemia (Kos et al., 2009).

Besides the ischemia-hyperemia protocol to investigate the BOLD response, hyperoxia induced BOLD signal changes have been observed in calf muscles due to the inhalation of 100% O_2 (Noseworthy et al., 2003; Bulte et al., 2006). Using a square ideal waveform to represent the cycles of normal air and 100% O_2 , correlations have been observed between the measured BOLD signal

and the predicted model in the soleus and gastrocnemius muscles (Noseworthy et al., 2003). The performance of strenuous exercise has been shown to result in variations in the BOLD response of these two muscles. In addition, ingestion of vasoactive substances has been observed to affect the BOLD signal of the two muscle regions differently due to their differing fiber types (Bulte et al., 2006).

Numerous studies have used exercise as a paradigm to investigate muscle oxygenation and examine the BOLD response (Meyer et al., 2004; Wigmore et al., 2004; Towse et al., 2005; Damon et al., 2007; Towse et al., 2011; Slade et al., 2011). A positive transient BOLD effect has been observed in the anterior tibialis muscle after the performance of a single, brief (one second in duration) muscle contraction (Meyer et al., 2004). A mean signal intensity increase of $2.6 \pm 0.6\%$ was measured after muscle contraction, which took approximately 8 s to peak post the contraction (Meyer et al., 2004). The group also noted that the magnitude of change in the signal intensity was higher at a larger field strength (Meyer et al., 2004). Another study looked at the BOLD effect following single contractions in the anterior tibialis muscle of healthy physically active subjects and sedentary individuals (Towse et al., 2005). The group noted that the transient BOLD peak magnitude was significantly higher in active subjects ($5.5 \pm 1\%$ change in signal intensity) compared to sedentary

individuals ($1.5 \pm 0.4\%$ change in signal intensity) (Towse et al., 2005). The post contraction BOLD technique has been used to assess the response of patients with diabetes and investigate the effects of aging (Slade et al., 2011). No differences were observed in the average peak BOLD response between controls and sufferers from diabetes (Slade et al., 2011). In addition, a negative relation was found between muscle BOLD response and age (Slade et al., 2011). Although this study found that contraction-induced BOLD was similar between healthy individuals and people diagnosed with diabetes, the researchers recommended that the utility of the muscle BOLD technique should be further investigated in compromised populations, as their study had only a small set of individuals with diabetes (n=31) (Slade et al., 2011).

A few studies have attempted to understand the physical mechanism responsible for the observed BOLD transient response following brief contractions (Wigmore et al., 2004; Damon et al., 2007; Towse et al., 2011). In one study, positive BOLD transients were observed following single contractions using short echo time, TE (6 ms) and long echo time(46 ms) (Damon et al., 2007). By comparing the BOLD results with data from near infrared spectroscopy (NIRS), it was concluded that changes in blood volume are primarily reflected when a short TE is used in the BOLD acquisition, whereas the use of longer TE reflects blood oxygenation (Damon et al., 2007). Recently, re-

searchers acquired blood flow, blood volume and saturation measurements to try and explain the contribution of each of the measured metrics to the post contractile BOLD signal time course (Towse et al., 2011). The study confirmed that the BOLD signal is not just related to blood flow, as a weak relationship was found between peak post contractile anterior tibial artery flow and anterior tibialis BOLD signal. It was concluded that the post contractile BOLD peak was dependent on both blood volume and oxygen saturation (Towse et al., 2011).

Although BOLD MRI studies of skeletal muscles are mostly paradigm based, interest has been recently shown in assessing skeletal muscles in the resting state (Zuo et al., 2012). This is because in a clinical setting, patients tend to have poor health conditions or show physical weakness, making a resting state approach to examine muscles more tolerable than one that requires the performance of a task (Zuo et al., 2012). Resting state analysis of BOLD signals has become a widely applied technique for analyzing brain BOLD signals (Maxim et al., 2005; Kiviniemi, 2009; Wang et al., 2011). Although numerous methods can be used to examine the resting signal of functional MRI time series exhibiting BOLD contrast, in recent years, researchers have shown interest in applying fractal analysis to such time series. Most papers have examined the fractal nature of the BOLD signal of the brain (Maxim et al., 2005;

Kiviniemi, 2009; Wang et al., 2011; Warsi et al., 2012). However, BOLD signals of tumors (Wardlaw et al., 2008) and skeletal muscle (Noseworthy et al., 2010) have also been investigated using fractals. The fractal method of analyzing biological time series is not a new technique (Schepers et al., 2002); it has been used in the past decades to characterize electroencephalographic (EEG) signals (Paramanathan and Uthayakumar, 2008). Fractals do not just represent dynamic signals (as are many physiological time series), they can also represent geometrical structures (Lopes and Betrouni, 2009; Kalliokoski et al., 2003). For instance, the bronchial tree (Goldberger and West, 1987) or Koch's curve, shown in figure 2.15, both represent fractal structures.

Several methods are available to calculate the fractal dimension (FD) or the Hurst exponent, H , of a time series (Eke et al., 2000, 2002; Schepers et al., 2002; Delignières et al., 2005; Lopes and Betrouni, 2009; Eke et al., 2012) (refer to section 2.3 for a detailed explanation of fractals). They all rely on the fact that a signal that may seem random can be represented by a complex pattern of correlations when examined using various time scales. Thus, such a randomly seeming signal could exhibit self similarity. Assessing signal complexity, by computing the FD index, has been shown to be useful in highlighting regions that demonstrate changes in microvasculature, such as

tumors (Wardlaw et al., 2008) and healthy muscles following moderate exercise (Noseworthy et al., 2010).

Besides analyzing the BOLD signal using fractals, another technique to analyze the time series is by looking at the frequency distribution in the signal. This method was used to assess muscle BOLD data from a patient affected with compartment syndrome and a lack of physiological signals was noted in the affected muscle (Noseworthy et al., 2010).

Chapter 2

Technical Details

Magnetic resonance imaging (MRI) is a technique that produces images of the body by probing the magnetic properties of certain nuclei. In most clinical MR imaging, the nucleus of the hydrogen atom is responsible for the signal that is detected. There are applications where nuclei of other elements, such as phosphorus or sodium, are used to gain further insight into specific pathological and physiological conditions. However, since most of the human body contains water molecules (H_2O) and fat chains ($-\text{CH}_2-$), the hydrogen nucleus is abundant in the body. Thus, imaging using the ^1H atom is favorable since it enables strong MR signals to be easily collected from a given region of interest. It should be noted that most scanners that are available on the market for clinical use do not come with the additional hardware or software that may be necessary to image and analyze nuclei other than hydrogen. Therefore, the following description of MRI will focus on the properties of the hydrogen nucleus. A discussion of other nuclei is beyond the scope of this thesis and interested readers are encouraged to look for appropriate textbooks. Most of the content about MR physics in this chapter has been adapted from (Liang

and Lauterbur, 2000; de Graaf, 2007; Hashemi et al., 2004; McRobbie et al., 2003; Bernstein et al., 2004; Prince and Links, 2006).

Although anatomical images are the conventional way to assess disease status, as such images provide depictions of the structure of the tissue being examined, functional MR imaging approaches are becoming popular in clinical settings as they are sometimes able to detect subtle changes within a tissue and assess abnormalities before they manifest themselves and become visible on conventional anatomical images. Diffusion tensor imaging (DTI) and blood oxygen level dependent (BOLD) MRI are two functional imaging techniques that were investigated in this project, thus an introduction to these approaches is given in the chapter.

2.1 Basic MRI Physics

2.1.1 Nuclear Properties

MRI is derived from nuclear magnetic resonance (NMR). Thus, an understanding of the nucleus and its interactions within a magnetic field is essential in order to comprehend how MRI works. The nucleus of a given atom is made up of a certain number of protons and neutrons. Some of the properties of these particles are listed in table 2.1. The spin property, which will

Property	Particle	
	Neutron	Proton
Charge (C)	0	1.602×10^{-19}
Mass (kg)	1.6749×10^{-27}	1.6726×10^{-27}
Spin	1/2	1/2

Table 2.1: Some properties of the proton and the neutron.

be denoted by the letter s for a given particle, needs some explanation as it is not as intuitive as mass or charge. From a classical representation, spin can be thought of as the physical rotation of a particle about its axis. Since the components of a given nucleus (the neutrons and protons) each have an intrinsic spin, s , the nucleus has a net spin that can be described by a nuclear spin quantum number, I . The general rules for determining the net spin of a nucleus are given in table 2.2. Nuclei with a zero nuclear spin quantum number, such as ^{12}C or ^{16}O , are NMR inactive. For the ^1H nucleus, which has a single proton, the associated nuclear spin quantum number is $I = 1/2$. Other nuclei with an $I = 1/2$ are ^{31}P and ^{13}C . ^{23}N is an example of a nucleus with a spin quantum number of $3/2$. Nuclei of the same type, such as a collection of ^1H nuclei, are commonly referred to as a nuclear spin system.

Moving particles possess momentum. Essentially, momentum can be thought of as the tendency of a particle to continue its motion. Linear mo-

Nuclear Composition		
Mass Number	Charge Number	Nuclear Spin, I
Even	Even	0
Even	Odd	Integer
Odd	Even or Odd	Half an integer

Table 2.2: Rules to deduce the nuclear spin, I , based on the mass and charge numbers of the nucleus of interest. Recall that the mass number is the number of nucleons (protons and neutrons) whereas the charge number is the number of protons.

momentum is a vector quantity that is defined as the product of the mass and velocity for a particle undergoing linear motion. Consequently, spinning particles have angular momentum. The angular momentum, \vec{L} , associated with a nuclear spin has a magnitude given by:

$$L = \frac{h}{2\pi} \sqrt{I(I+1)} \quad (2.1)$$

where h is Planck's constant (6.626068×10^{-34} m²kg/s) and I is the nuclear spin quantum number (see table 2.2).

2.1.2 Nuclei in a Magnetic Field

Nuclei that have nonzero spin are able to interact with a magnetic field. This is because such nuclei possess a magnetic moment, $\vec{\mu}$. Basically, magnetic moment describes the magnetic field that is generated by a nucleus. It is known

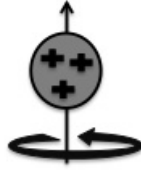


Figure 2.1: A spinning charge can be thought of as a small magnet that generates a magnetic field.

from electromagnetic theory that a moving charge generates a magnetic field. Thus, a nucleus with a nonzero spin can be classically thought of as a spinning charged entity that creates a magnetic field (figure 2.1). The magnetic moment and angular momentum of a given particle are related through:

$$\vec{\mu} = \gamma \vec{L} \quad (2.2)$$

where γ is a nucleus-dependent constant known as the gyromagnetic ratio. For the ^1H nucleus, $\gamma/2\pi = 42.57 \text{ MHz/T}$.

In the absence of an external magnetic field, the direction of the magnetic moment vectors within a sample is random. If an external magnetic field, commonly referred to as the \vec{B}_0 field, is applied as is done in MRI, the magnetic moment vectors try to align with the field. Typical clinical MRI scanners have B_0 field strength of 1.5 or 3T. In comparison with the Earth's magnetic field (which is approximately 0.05mT), the magnetic field of a 1.5T

scanner is about 30,000 times stronger. The external magnetic field, \vec{B}_0 , is conventionally applied along the z-direction, which is typically along the bore of the MR scanner. Thus,

$$\vec{B}_0 = B_0 \vec{z} \quad (2.3)$$

Application of \vec{B}_0 results in the alignment of the magnetic moment vectors with the field. However, the magnetic moments only assume a certain set of orientations because of the laws of quantum mechanics. The z-component of the angular momentum vector, L_z , is given by:

$$L_z = \frac{h}{2\pi} m \quad (2.4)$$

where m is the magnetic moment quantum number and can have $2I + 1$ values ranging from $-I \leq m \leq +I$. From equations 2.2 and 2.4, the z-component of the magnetic moment vector becomes:

$$\mu_z = \gamma L_z = \gamma \frac{h}{2\pi} m \quad (2.5)$$

The $2I + 1$ orientations that the magnetic moments can assume with respect to the external magnetic field are such that the angle, θ , between $\vec{\mu}$ and \vec{B}_0 (see figure 2.2) is given by:

$$\cos \theta = \frac{\mu_z}{\mu} = \frac{m}{\sqrt{I(I+1)}} \quad (2.6)$$

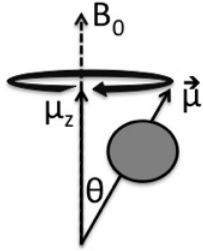


Figure 2.2: The angle between the magnetic moment and the applied external field is defined as θ and is calculated using equation 2.6.

Hence, for nuclei with $I = 1/2$, like the ^1H nucleus, $m = \pm 1/2$ and the nucleus has two allowed spin states, where the magnetic moment vectors are at $\theta = 54.74^\circ$ relative to the $\pm z$ -axis in the presence of an external magnetic field (figure 2.3).

Placement of the magnetic moments in an external magnetic field has thus far resulted in the distribution of the moments at discrete angles, θ , on the surface of $2I + 1$ cones (where for a spin-1/2 system, the spins are distributed on two cones as seen in figure 2.4). Since $\vec{\mu}$ does not perfectly align with the field, it continues to experience a torque (i.e. a rotating force), given by:

$$\vec{\tau} = \vec{\mu} \times B_0 \vec{z} \quad (2.7)$$

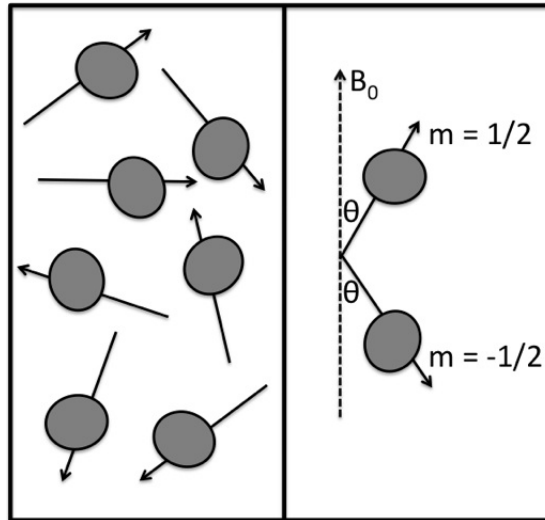


Figure 2.3: In the absence of \vec{B}_0 , the direction of the magnetic moment vectors is random. Application of a \vec{B}_0 field causes the magnetic moments for $I = 1/2$ nuclei to align with or against the field at an angle of 54.74° relative to the direction of $\pm B_0$.

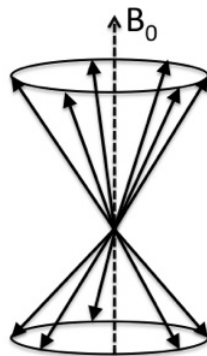


Figure 2.4: For a spin-1/2 system in the presence of an external field, B_0 , the spins precess about the B_0 in one of two possible orientations: either parallel or antiparallel to the field. Although they spin with the same frequency, they are out of phase with each other (i.e. the precession is incoherent).

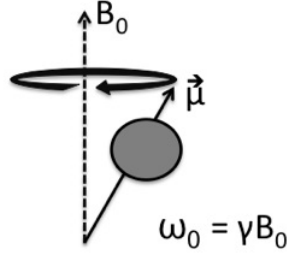


Figure 2.5: The precession frequency of the nucleus, ω_0 , also known as the Larmor frequency. For the ^1H nucleus and in a 1.5T field, $\omega_0 = 63.86$ MHz.

Using equation 2.2, and from the definition of torque, which is the rate of change of the angular momentum, the equation for the motion of a spin in an external magnetic field becomes:

$$\frac{d\vec{\mu}}{dt} = \gamma\vec{\mu} \times B_0\vec{z} \quad (2.8)$$

Setting $\omega_0 = \gamma B_0$ and solving the differential equation yields:

$$\begin{aligned} \mu_x(t) &= \mu_x(0) \cos(\omega_0 t) + \mu_y(0) \sin(\omega_0 t) \\ \mu_y(t) &= \mu_y(0) \cos(\omega_0 t) - \mu_x(0) \sin(\omega_0 t) \\ \mu_z(t) &= \mu_z(0) \end{aligned} \quad (2.9)$$

where $\mu_x(0)$, $\mu_y(0)$ and $\mu_z(0)$ are the initial conditions. Thus, the magnetic moment precesses around the z-axis (figure 2.5) with a frequency known as the Larmor frequency, given by:

$$\omega_0 = \gamma B_0 \quad (2.10)$$

2.1.3 Magnetization of a Sample

When a sample or object is placed in an external magnetic field, the behavior of the spin system is described using a magnetization vector, \vec{M} , which is the vector sum of all the individual magnetic moments and may be referred to as the bulk or net magnetization. Thus,

$$\vec{M} = \sum_{i=1}^N \vec{\mu}_i \quad (2.11)$$

where N is the total number of magnetic moments. For a spin-1/2 nucleus, the spins may take one of two possible orientations, parallel or antiparallel, when placed in an external magnetic field (figure 2.3). Each of these spin states has an associated energy, E , given by:

$$E = -\mu_z B_0 \quad (2.12)$$

Using equation 2.5 for μ_z , the energy of the spins becomes:

$$E = -\gamma \frac{h}{2\pi} m B_0 \quad (2.13)$$

Since $m = \pm 1/2$ for spin-1/2 systems, the two energy levels that a particle can occupy in the presence of an external magnetic field are:

$$\begin{aligned} E_{m=+1/2} &= E_{\uparrow} = -\gamma \frac{h}{4\pi} B_0 \\ E_{m=-1/2} &= E_{\downarrow} = \gamma \frac{h}{4\pi} B_0 \end{aligned} \quad (2.14)$$

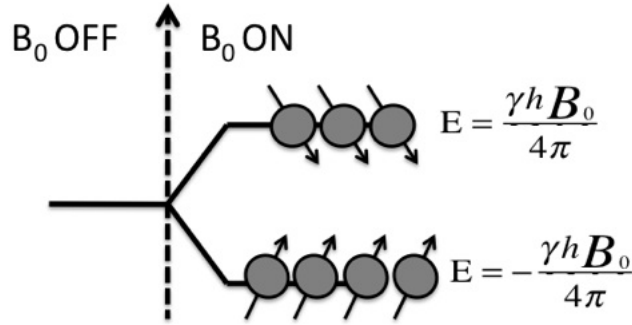


Figure 2.6: For a system with $I = 1/2$, Zeeman splitting results in two energy states, where the low energy state corresponds to the parallel orientation of the magnetic moments with the B_0 field.

The energy difference between these two alignment states is referred to as the Zeeman splitting (figure 2.6) and is calculated to be:

$$\Delta E = E_{\downarrow} - E_{\uparrow} = \gamma \frac{h}{2\pi} B_0 \quad (2.15)$$

Whether a spin is aligned in the parallel or antiparallel direction in the presence of the magnetic field is dependent on the internal energy of the individual spin. Using the Boltzmann distribution, the population difference between the two spin states is given by:

$$\frac{N_{\uparrow}}{N_{\downarrow}} = \exp\left(\frac{\Delta E}{\kappa T}\right) \quad (2.16)$$

where N_{\uparrow} is the number of spins pointing upwards (in the low energy state), N_{\downarrow} is the number of spins in the high energy state, κ is the Boltzmann constant

$(1.38 \times 10^{-23} \text{J/K})$ and T is the absolute temperature. Using expansion and truncation, equation 2.16 becomes:

$$\frac{N_{\uparrow}}{N_{\downarrow}} \approx 1 + \frac{\Delta E}{\kappa T} \approx 1 + \frac{\gamma h B_0}{2\pi \kappa T} \quad (2.17)$$

At body temperature ($37^\circ\text{C} = 310.15\text{K}$) and a field strength of 3T , the ratio of spins in the low energy state to those in the high energy state can be calculated to be:

$$\frac{N_{\uparrow}}{N_{\downarrow}} \approx 1 + \frac{(42.57 \times 10^6 \text{Hz/T})(3\text{T})(6.6 \times 10^{-34} \text{Js})}{(310.15\text{K})(1.38 \times 10^{-23} \text{J/K})} = 1.0000198 \quad (2.18)$$

The result of equation 2.18 implies that for every million spins in the high energy state, there are a million and twenty spins in the low energy state. The small population difference in the spin distribution contributes to an observable net magnetization vector as given by equation 2.11. At equilibrium, this net magnetization is referred to as \vec{M}_0 . It can be seen from figure 2.4 that there is no transverse component of \vec{M}_0 at equilibrium because the spins are out of phase with each other. Thus, $\vec{M}_{xy}=0$. The excess fraction of spins in the low energy state results in a net magnetization that points along the direction of the applied magnetic field, a longitudinal magnetization, \vec{M}_z . Using equa-

tions 2.5, 2.11 and 2.17, the magnitude of the net longitudinal magnetization becomes:

$$M_0 = \frac{NB_0\gamma^2\hbar^2}{16\kappa T\pi^2} \quad (2.19)$$

The small net magnetization vector is on the order of micro tesla. As can be seen from equation 2.19, the magnitude of M_0 depends on the strength of the external field, the temperature of the object being imaged, and the total number of spins that are being probed.

2.1.4 RF Excitation

In order to detect an MR signal, the net longitudinal magnetization vector must be tipped away from the equilibrium position and towards the transverse plane. By applying an RF pulse, denoted as $\vec{B}_1(t)$, \vec{M}_0 rotates towards the xy plane. $\vec{B}_1(t)$ oscillates in the radio-frequency range (MHz) and has a magnetic field strength that is on the order of milli tesla. It is typically turned on for a short period of time (on the order of micro or milli seconds) then turned off. From a quantum mechanical description, the applied RF pulse excites some of the nuclear spins and results in the induction of transitions from the low energy state to the high energy state. This happens if the energy of the excitation pulse matches the energy difference between the spin states. In other words:

$$\hbar\omega_{rf} = \hbar\omega_0 \quad (2.20)$$

Thus, if the resonance condition (equation 2.20) is met, excitation occurs and phase coherence is generated between the spins. Macroscopically, application of the $\vec{B}_1(t)$ field, which is perpendicular to the \vec{B}_0 field, exerts a torque on the longitudinal magnetization, resulting in the rotation of \vec{M}_0 from the z-axis and towards the xy-plane. If observed from the stationary frame, the magnetization vector, which precesses about \vec{B}_0 and rotates towards $\vec{B}_1(t)$ will seem to follow a spiral path known as nutation. It is easier to describe the behavior of the magnetization vector after excitation using a frame that rotates clockwise with angular frequency ω_0 . In this frame, following excitation, the bulk magnetization vector will simply be tipped onto the transverse plane (figure 2.7).

The RF field that is used to tip the bulk magnetization can be linearly polarized or circularly polarized. A linearly polarized field is equivalent to two circularly polarized fields that rotate in opposite directions. However, since one of the components rotates in the direction opposite to that of the spins, it does not effect the spin system and it only results in exposing the patient to more RF energy. The circularly polarized field is given by:

$$\vec{B}_1(t) = B_1^A(t)[\cos(\omega_{rf}t)\vec{x} - \sin(\omega_{rf}t)\vec{y}] \quad (2.21)$$

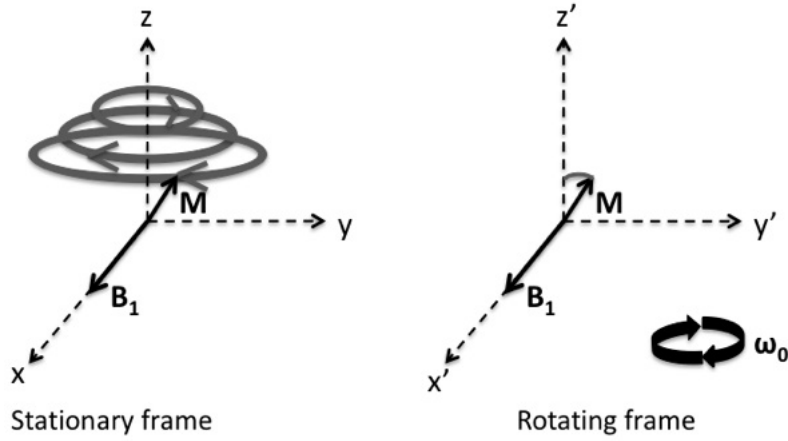


Figure 2.7: The motion of the bulk magnetization vector following excitation is complex when viewed from a stationary frame. If viewed from a frame that rotates at ω_0 , the magnetization vector is simply *tipped* into the xy plane as a result of the RF application.

where $B_1^A(t)$ is the envelope function of the pulse and ω_{rf} is the pulse's carrier frequency. Thus, the overall field felt by the spins when the RF pulse is on is the sum of \vec{B}_0 and $\vec{B}_1(t)$.

The behavior of the net magnetization vector over time in response to the applied RF pulse is described using the Bloch equation, given by:

$$\frac{d\vec{M}}{dt} = \gamma\vec{M} \times \vec{B} + \frac{M_0 - M_z}{T_1}\vec{z} - \frac{M_x\vec{x} + M_y\vec{y}}{T_2} \quad (2.22)$$

where M_0 is the net magnetization before the application of the RF pulse and T_1 and T_2 are relaxation constants that describe the relaxation of the spin

system after the RF is turned off. During RF excitation, the relaxation terms can be ignored. Thus, equation 2.22 becomes:

$$\frac{d\vec{M}}{dt} = \gamma\vec{M} \times \vec{B} \quad (2.23)$$

Since the overall field felt by the magnetization vector when the RF is applied is the sum of \vec{B}_0 (equation 2.3) and $\vec{B}_1(t)$ (equation 2.21), the Bloch equation can be written as:

$$\frac{d\vec{M}}{dt} = \gamma\vec{M} \times (B_1^A(t)[\cos(\omega_{rf}t)\vec{x} - \sin(\omega_{rf}t)\vec{y}] + B_0\vec{z}) \quad (2.24)$$

In a frame that rotates clockwise with ω relative to the stationary frame, equation 2.24 becomes:

$$\left(\frac{d\vec{M}}{dt}\right)_{rot} = \gamma\vec{M} \times \left(B_1^A(t)[\cos(\omega_{rf} - \omega)t\vec{x}' - \sin(\omega_{rf} - \omega)t\vec{y}'] + \left(B_0 - \frac{\omega}{\gamma}\right)\vec{z}'\right) \quad (2.25)$$

If the resonance condition is met (equation 2.20), then equation 2.25 becomes:

$$\left(\frac{d\vec{M}}{dt}\right)_{rot} = \gamma\vec{M} \times B_1^A(t)\vec{x}' \quad (2.26)$$

Thus, on resonance excitation results in the precession of the magnetization vector about the x-axis, where the $\vec{B}_1(t)$ field is applied. The solution to equation 2.26 under initial conditions of $M_{x'}=M_{y'}=0$ and $M_{z'}=M_0$ is:

$$\begin{aligned} M_{x'}(t) &= 0 \\ M_{y'}(t) &= M_0 \sin\left(\gamma \int_0^t B_1^A(t') dt'\right) \\ M_{z'}(t) &= M_0 \cos\left(\gamma \int_0^t B_1^A(t') dt'\right) \end{aligned} \quad (2.27)$$

where the flip angle, α (figure 2.8), is defined as

$$\alpha = \gamma \int_0^t B_1^A(t') dt' \quad (2.28)$$

For a rectangular RF pulse (also referred to as a "hard" pulse), the flip angle is equal to $\gamma B_1 T$, where B_1 is the amplitude of the pulse and T is the duration of the pulse. An RF pulse that tips the magnetization vector by α° is commonly referred to as an α° pulse. Thus, a 90° pulse results in the tipping of the magnetization vector completely onto the xy-plane. If the resonance condition is not met, then equation 2.25 becomes:

$$\left(\frac{d\vec{M}}{dt}\right)_{rot} = \gamma \vec{M} \times \left(B_1^A(t) \vec{x}' + \left(B_0 - \frac{\omega}{\gamma} \right) \vec{z}' \right) \quad (2.29)$$

and the magnetization vector precesses about an effective field given by the bracketed term in equation 2.29.

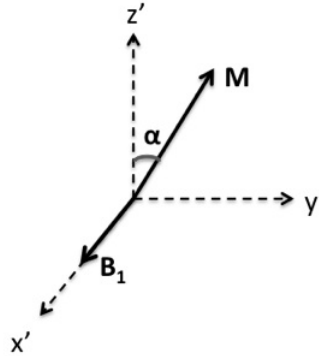


Figure 2.8: The magnetization vector is *tipped* through an angle of α , given by equation 2.28 due to the application of the B_1 field.

Once the magnetization vector has been tipped by the RF pulse towards the transverse plane, its precession causes a changing magnetic flux, Φ , to be experienced by the receiver coil. This changing flux induces an electromotive force, emf , in the coil that surrounds the sample and is given by Faraday's law as:

$$emf = -\frac{d\Phi}{dt} \quad (2.30)$$

2.1.5 Relaxation Mechanisms

Since the spins begin to return to their equilibrium position after the RF field is turned off, loss of phase coherence between the spins results in the exponential decay of the MR signal. Two relaxation processes occur immedi-

ately after the RF pulse is turned off, referred to as longitudinal and transverse relaxation.

2.1.5.1 Longitudinal Relaxation

Longitudinal relaxation, which is also known as T_1 relaxation or spin-lattice relaxation, refers to the transfer of RF energy from the spins back to the surrounding lattice. As the spins lose the deposited energy, they move from the high energy state back to the lower energy one and a recovery of the longitudinal magnetization occurs. The change in longitudinal magnetization is described using:

$$\frac{dM_z}{dt} = \frac{M_0 - M_z}{T_1} \quad (2.31)$$

where T_1 is the time constant that describes the recovery of the magnetization to the equilibrium position along the z-axis. Solving equation 2.31 yields:

$$M_z = M_0 + (M_{z0} - M_0)e^{-\frac{t}{T_1}} \quad (2.32)$$

Figure 2.9 shows the recovery of T_1 .

2.1.5.2 Transverse Relaxation

Transverse relaxation, which is also known as spin-spin relaxation or T_2 relaxation describes the loss of phase coherence that occurs between the spins after they had been tipped onto the xy-plane. This happens because

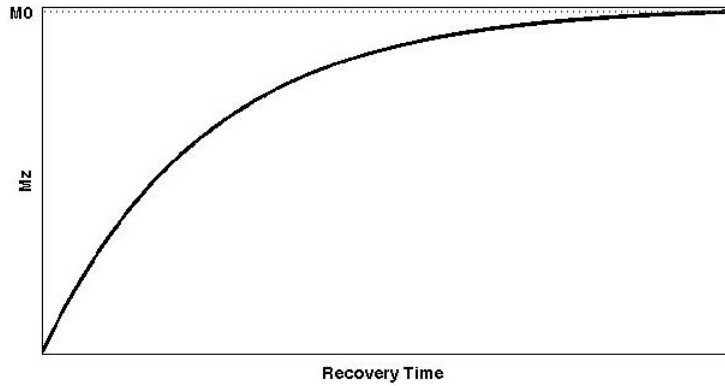


Figure 2.9: T_1 recovery curve.

interactions between the spins result in some of the spins experiencing a higher magnetic field while others experience a lower field. Thus, the precessing spins eventually fan out and phase coherence is lost. The change in transverse magnetization over time can be given by:

$$\frac{dM_{xy}}{dt} = -\frac{M_{xy}}{T_2} \quad (2.33)$$

where T_2 is the time constant that describes the decay of the transverse magnetization in the xy-plane. Solving equation 2.33 gives:

$$M_{xy} = M_{xy0}e^{-\frac{t}{T_2}} \quad (2.34)$$

Figure 2.10 shows the decay of T_2 . The transverse magnetization does not only decay due to the spin-spin interactions. Local magnetic field inhomogeneities also result in a loss of phase coherence between the spins. T_2^* is a

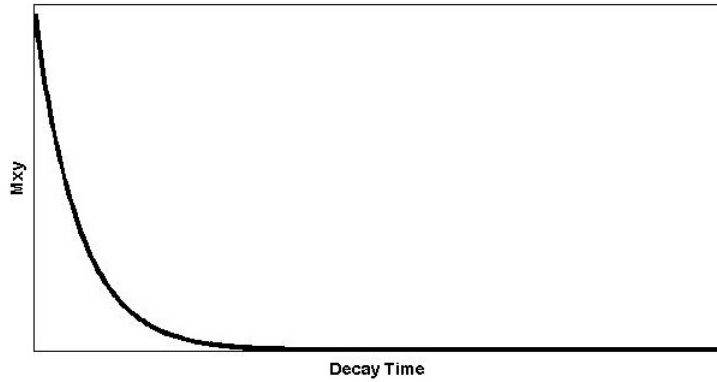


Figure 2.10: T_2 decay curve

decay constant that takes into account both intrinsic (spin-spin interactions) and extrinsic (local field inhomogeneity) effects. T_2^* is given as:

$$\frac{1}{T_2^*} = \frac{1}{T_2} + \frac{1}{T_2'} = \frac{1}{T_2} + \gamma\Delta B_0 \quad (2.35)$$

T_2^* decay is thus always faster than T_2 decay since it includes magnetic field inhomogeneity effects in addition to transverse relaxation.

2.1.5.3 T_1 and T_2 in Tissues

T_1 and T_2 are inherent properties of the specific tissue and T_2 is always shorter than T_1 . In biological tissues, these constants are on the order of milli seconds. Table (2.3) lists values of T_1 and T_2 for some tissues at 3T. Since T_2 describes spin-spin interactions, molecules with structures that allow many interactions to occur between their constituents have short T_2 values.

Tissue	T_1 (ms)	T_2 (ms)
Skeletal muscle ¹	1420 ± 38	31.7 ± 1.9
Synovial fluid ¹	3620 ± 320	767 ± 49
Gray matter ²	1331 ± 13	110 ± 2
White matter ²	832 ± 10	79.6 ± 0.6
Cerebral spinal fluid ³	4163 ± 263	

Table 2.3: T_1 and T_2 values of some tissues measured in humans at 3T. ¹Data from (Gold et al., 2004) (shown are mean \pm standard deviation). ²Data from (Wansapura et al., 1999), showing mean \pm standard error. ³Data from (Lin et al., 2001) (mean \pm standard deviation).

This is because the close proximity of the spins to each other facilitates quick dephasing. For example, solids dephase faster than water-based or fat-based tissues, which dephase faster than fluids. Hence, fluids have longer T_2 values. T_1 describes the ability of the spins to exchange their energy with the lattice. As a general rule, fluids are less efficient at this energy exchange than fat.

2.1.6 Spatial Localization

In order to achieve spatial localization and obtain images from a desired location within an object, gradients are used in MRI. Gradient coils produce linearly varying magnetic fields that can be applied along any desired axis. The magnitude of the gradient is typically on the order of milli Tesla per meter. Application of a gradient field, \vec{G} , results in a linear distribution of

the precessional frequency of spins based on their location along the gradient. The effect of a gradient, \vec{G} , applied along a direction, \vec{r} , on the frequency of precession is such that:

$$\omega(\vec{r}) = \gamma \vec{G} \cdot \vec{r} \quad (2.36)$$

2.1.6.1 Slice Selection

The first step in spatial localization is selecting a specific slice or slab from within the imaged sample. This is achieved using a slice selection gradient in conjunction with an RF pulse. For instance, when axial slices are acquired, a gradient is applied along the z-direction, G_z , resulting in variations in the larmor frequency along the z-axis. This gradient is referred to as the slice select gradient. The application of an RF pulse of a certain frequency at the same time as the slice select gradient results in the selection of a slice from a position along the gradient where the precessional frequency of the spins matches the RF center frequency. Changing the center frequency of the RF pulse results in the selection of a slice from a different position. To vary the slice thickness, gradient strength or RF transmit bandwidth must be changed. Increasing the gradient strength or decreasing the transmit bandwidth of the RF result in the selection of thinner slices.

2.1.6.2 Phase and Frequency Encoding

Following slice selection, spatial localization of the MR signal within a slice is achieved by applying gradients along the two remaining axes, G_x and G_y . Pictorially, application of gradients along each of these axes would result in each voxel within a slice having a unique phase and frequency. However, this is an oversimplification of the spatial encoding process. To comprehend how the signal is localized from a slice, it is important to realize that the raw MR data collected during an imaging session is not the MR image, but a representation of it in terms of spatial frequencies. These frequencies are organized in a grid that is referred to as k -space. This space has coordinates of k_x in the horizontal direction and k_y in the vertical direction, where the units of these coordinates are in inverse length (i.e. cm^{-1}). By performing a 2D Fourier transform on the k -space data, the MR image can be reconstructed and is then displayed on the scanner console.

In order to localize the MR signal from within a slice, gradients have to be applied in such a way that enough information can be collected to fill k -space. The rate at which k -space is sampled in the x and y directions is given by Δx and Δy , respectively. Application of a frequency (readout) encoding gradient while the signal is being collected results in the filling of one line of k -space. To move the readout to a different row in k -space, a phase encoding

gradient is applied. The phase encoding gradient has to be incremented during the imaging sequence so that all of k -space can be filled.

2.1.7 Pulse Sequences

Pulse sequences are timing instructions that layout the steps needed to manipulate the magnetization within a sample. A pulse sequence diagram usually shows the various MR components (gradients, RF pulses) that must be applied at certain times during the scanning session to generate an MR signal. Two commonly used pulse sequences in MR imaging are the spin echo and gradient echo sequences.

2.1.7.1 Spin Echo

In a standard spin echo (SE) sequence (figure 2.11), application of a 90° RF pulse tips the magnetization vector onto the xy-plane. Due to spin-spin interactions, a loss of phase coherence results between the spins and thus, the spins “fan out”. Using a 180° RF pulse, spin rephasing is achieved and an echo (the MR signal) is generated. The interval between the application of the first RF pulse and the production of the echo is known as the echo time, T_E . In order to be able to acquire all of k -space, the spin echo technique has to be repeated while varying the phase encoding gradient. T_R is the time interval

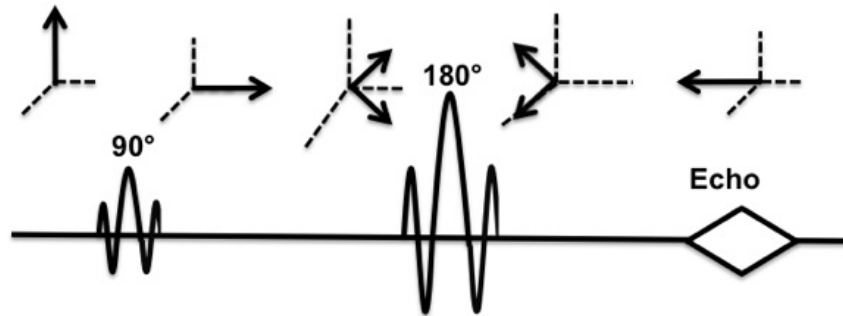


Figure 2.11: Pulse sequence for a spin echo along with the corresponding effect on an ensemble of spins.

between each of the repetitions. In a standard spin echo sequence, one line of k -space is collected during each T_R .

A modification of the conventional spin echo is the fast spin echo (FSE) sequence. In an FSE sequence, multiple lines of k -space are filled during each T_R . Instead of collecting one echo, a number of echoes (referred to as an echo train length, ETL) is acquired. For instance, if an ETL of 8 is used, then 8 lines of k -space are gathered. Thus, for an image with 512 phase encoding steps, the process would only have to be repeated 64 times (i.e. $512/8$) as opposed to 512 times as in the standard SE sequence.

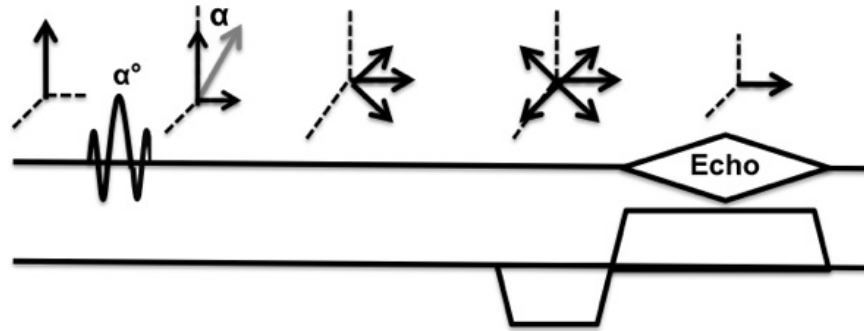


Figure 2.12: Pulse sequence for a gradient echo along with the corresponding effect on an ensemble of spins.

2.1.7.2 Gradient Echo

A standard gradient echo (GRE) sequence (figure 2.12) begins with the application of an excitation RF pulse that typically results in the flipping of the magnetization vector through an angle of less than 90° . The use of a small flip angle allows for fast image acquisition speeds and thus, GRE is commonly applied when fast imaging is desired. Following excitation, a negative gradient lobe, referred to as a dephasing or prephasing lobe, is used to dephase the spins. The application of a readout gradient of opposite polarity results in the spins becoming in phase and an echo is formed.

2.1.7.3 Echo Planar Imaging

A very fast and commonly used MR acquisition technique is echo planar imaging (EPI). This technique is especially useful when monitoring of rapid physiological changes is needed as is the case with functional imaging. In EPI, all of the lines of k -space can be acquired during one repetition time (single shot). However, single shot EPI images usually have lower resolution (less than 128x128). To collect all of k -space in one shot, EPI relies on the use of gradients that rapidly oscillate to allow all of k -space to be traversed in a short time.

2.2 Diffusion Tensor Imaging

Diffusion describes the random microscopic motion that particles undergo when suspended in a fluid. This is sometimes referred to as Brownian motion, after the botanist Robert Brown who observed the movement of pollen grains when they were suspended in fluid. Diffusion can be driven by a concentration gradient, where particles move from a region with a high concentration to one of lower concentration. In this case, Fick's first law is used to model the diffusion process such that (de Figueiredo et al., 2011):

$$\mathbf{J} = -D\nabla C \tag{2.37}$$

where \mathbf{J} gives the rate of flow per unit area (the flux), D is the diffusion coefficient and C is the particle concentration. The diffusion coefficient has dimensions of $\text{length}^2\text{time}^{-1}$ and is usually expressed in mm^2s^{-1} . However it may sometimes be given in m^2s^{-1} or cm^2s^{-1} . The negative sign in the equation shows that the diffusion goes in the opposite direction of the increasing concentration.

Although diffusion commonly refers to the movement of particles down a concentration gradient, diffusion can occur even in the absence of a concentration gradient. In this case, it is referred to as “self diffusion” (Winston, 2012) and the particles’ motion is the result of the thermal energy that they possess. The Einstein equation describes the rate of diffusion in this case, and is given by (Mukherjee et al., 2008):

$$\langle R^2 \rangle = 6Dt \quad (2.38)$$

where $\langle R^2 \rangle$ is the mean squared displacement, t is the diffusion time and D is the diffusion coefficient. The self-diffusion coefficient of pure water is $2.02 \times 10^{-3} \text{ mm}^2/\text{s}$ and $2.92 \times 10^{-3} \text{ mm}^2/\text{s}$ at 20°C and 35°C , respectively (Dietrich et al., 2010).

The inclusion of the diffusive mechanisms into the Bloch equation (equation 2.22) was made by Torrey, and the Bloch equation is sometimes

referred to as the Bloch-Torrey equation to indicate the addition of diffusion (Basser and Jones, 2002). Stejskal and Tanner proposed a way to measure the diffusion coefficient with MRI using a pair of diffusion sensitizing gradients (de Figueiredo et al., 2011) or motion probing gradients (Mukherjee et al., 2008). These gradients are also sometimes referred to as the Stejskal-Tanner diffusion gradients (Dietrich et al., 2010). Figure 2.13 shows a spin echo scheme with diffusion gradients used to produce diffusion weighted images. Following excitation, the spins are tipped by 90° . Application of the first diffusion encoding gradient results in the introduction of a phase difference between the spins, depending on their location along the gradient. When the 180° pulse is applied, it reverses the phase of the spins. Application of the second gradient then induces a phase shift. For spins that are stationary, the amount of dephasing and rephasing caused by the gradient lobes is identical and thus, the transverse magnetization is not affected. For spins that move along the direction of the gradient, the random motion that they undergo causes them to move to a different position during the time between the gradients, Δ . When the rephasing gradient is then applied, the spins experience a different field than the one that was introduced by the initial dephasing gradient. Thus, complete refocusing does not occur when the second gradient is applied and the observed transverse magnetization is decreased, which is the same as say-

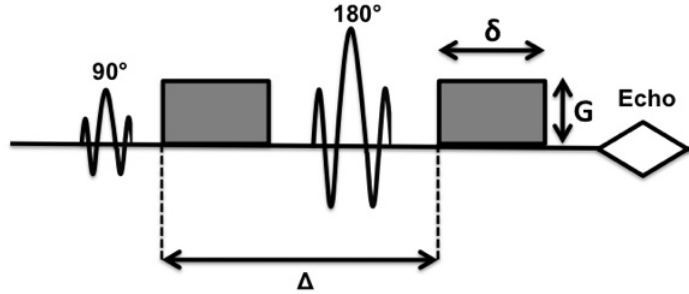


Figure 2.13: Simplified pulse sequence diagram used to capture diffusion. The b-value depends on the interval between the two gradients, Δ , the duration, δ , and amplitude, G , of the gradients.

ing that the observed signal is attenuated, resulting in regions of low intensity where diffusion occurs along the gradient (Hagmann et al., 2006).

The attenuation of the observed signal due to molecular diffusion is affected by some factors (Mori, 2007). These are the timing between the gradients (Δ), the diffusion constant (D) and the gradient duration (δ) and strength (G). The higher these parameters are (longer time between gradients, larger diffusion constant, stronger or longer gradients), the larger the observed signal loss (greater diffusion weighting) due to the corresponding greater amount of molecular motion (Mori, 2007).

In order to measure the diffusion coefficient along one direction, two MR acquisitions (at least) are needed. If S_0 represents the signal intensity in the absence of any gradients and S represents the intensity after the application

of the Stejskal-Tanner diffusion gradients, then signal attenuation (S/S_0) can be written as (Mori, 2007):

$$\frac{S}{S_0} = e^{-\gamma^2 G^2 \delta^2 (\Delta - \delta/3) D} \quad (2.39)$$

where γ is the gyromagnetic ratio, G , Δ and δ are as defined in figure 2.13 and D is the diffusion coefficient. Equation 2.39 can also be written as:

$$\frac{S}{S_0} = e^{-bD} \quad (2.40)$$

where b is known as the b-factor or b-value and is expressed as:

$$b = \gamma^2 G^2 \delta^2 (\Delta - \delta/3) \quad (2.41)$$

Taking the natural logarithm of both sides of equation 2.40 gives:

$$\ln(S) = \ln(S_0) - bD \quad (2.42)$$

Having measured S and S_0 , the value of the diffusion coefficient can be determined by solving equation 2.42 (since b is a parameter of known variables).

In diffusion weighted imaging (DWI), gradients are applied along three orthogonal directions (x, y, and z) and thus diffusion sensitization is achieved along the right-left, anterior-posterior and superior-inferior directions (de Figueiredo et al., 2011). It should be noted that when measurements are made in vivo, the diffusion coefficient that is measured is referred to as the apparent diffusion

coefficient, or ADC , as the presence of molecules or cell membranes hinders the free diffusion of water (Dietrich et al., 2010). Thus, the “apparent” reduction in diffusion resulting from restricted water motion is what is measured in vivo (Mori and Zhang, 2006) and in equations 2.39-2.42, D is replaced with ADC for these measurements.

When diffusion of water molecules is isotropic, as is the case when there are no restrictions or if the environment contains randomly oriented structures, the diffusion will be equal along all directions and it can be characterized by a sphere (figure 2.14) (Mori, 2007). This type of diffusion can be sufficiently described by one parameter, the diffusion coefficient, as one number is enough to characterize the shape of a sphere (Mori, 2007). In such a case, regardless of the direction used for the diffusion sensitizing gradients, areas that exhibit isotropic diffusion will always exhibit the same signal properties on DW images and the ADC map will be identical in these regions for every gradient direction (Mukherjee et al., 2008).

Anisotropic diffusion refers to molecular motion that has a preferred direction due to the presence of barriers that restrict the free motion (figure 2.14). For tissues exhibiting anisotropic diffusion, the contrast of the generated ADC map in DW imaging is dependent on the direction of the applied gradients (Winston, 2012). For instance, if a fiber runs along the left-right

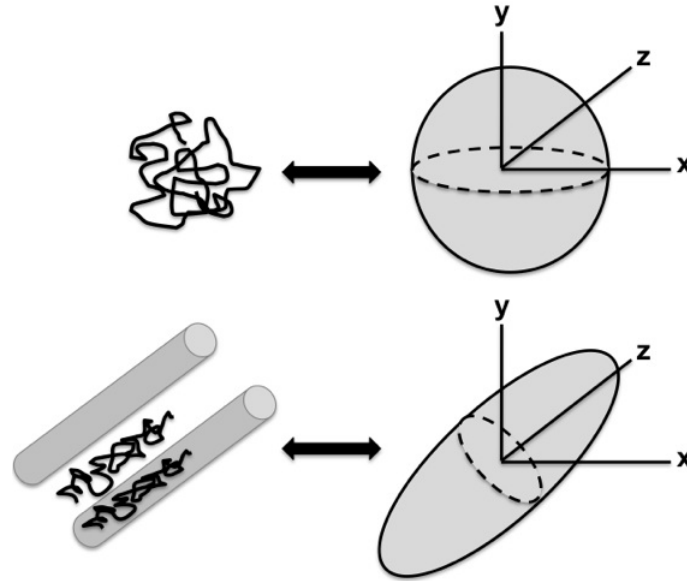


Figure 2.14: Diffusion can be isotropic (top row), where the molecule moves freely in all directions and the diffusion is modeled as a sphere. This motion occurs if the environment is unrestricted or contains random barriers. In the case of anisotropic diffusion (bottom row), the molecular motion is hindered by the presence of ordered structures, resulting in a diffusion ellipsoid.

direction (x-axis) and the gradient is applied along this direction, the measured ADC for this region will be higher than if the sensitizing gradients were applied along either of the other two directions. This finding that the contrast of the generated ADC maps in DWI depends on the direction of the applied gradients and the tissue orientation resulted in the introduction of the diffusion tensor to represent anisotropic diffusion.

Anisotropic diffusion is best characterized by an ellipsoid, where the longest axis corresponds to the direction of the greatest diffusion (figure 2.14). This type of diffusion can be represented by a diffusion tensor, \mathbf{D} given as:

$$\mathbf{D} = \begin{bmatrix} D_{xx} & D_{xy} & D_{xz} \\ D_{yx} & D_{yy} & D_{yz} \\ D_{zx} & D_{zy} & D_{zz} \end{bmatrix} \quad (2.43)$$

where the diagonal elements (D_{xx}, D_{yy}, D_{zz}) represent diffusion along the x, y and z axes and the off diagonal elements contain information about the rotations about these axes (Mori, 2007). Since the tensor is symmetric ($D_{ij} = D_{ji}$), only six parameters are needed to characterize it. These require that at least seven diffusion weighted images are collected. As was seen in equation 2.42, in order to calculate the diffusion coefficient, D , at least two measurements were needed. Thus, the six diffusion constants that make up the diffusion matrix, \mathbf{D} , require a minimum of seven diffusion weighted images to be collected. From the acquired diffusion weighted images, the diffusion tensor can be calculated using multivariate linear regression (Winston, 2012).

The obtained diffusion tensor has to be transformed to a diagonal matrix, resulting in three eigenvalues given by $\lambda_1, \lambda_2, \lambda_3$, and their corresponding eigenvectors, $\epsilon_1, \epsilon_2, \epsilon_3$ that together characterize the diffusion along an ellipsoid. The eigenvectors represent the directions of the molecular diffusion with

ϵ_1 being the primary eigenvector (Mukherjee et al., 2008) as it corresponds to the principle axis of diffusion. The eigenvalues give the magnitude of the diffusion along the directions given by the eigenvectors.

Numerous diffusion indices can be calculated from the three eigenvalues. These include the mean diffusivity, MD , which may also be given as the ADC and is simply the arithmetic mean of the three eigenvalues:

$$ADC = MD = \frac{\lambda_1 + \lambda_2 + \lambda_3}{3} \quad (2.44)$$

The MD can also be written as:

$$MD = \frac{Tr\mathbf{D}}{3} \quad (2.45)$$

where $Tr\mathbf{D}$ represents the mathematical sum of the three eigenvalues. Fractional anisotropy, FA , is another commonly used index to characterize diffusion. It scales between zero and one, where zero represents the case of perfect isotropic diffusion as in a sphere ($\lambda_1 = \lambda_2 = \lambda_3$). An FA of one represents diffusion along only the principle eigenvector (Mukherjee et al., 2008) as in a cylinder ($\lambda_1 \gg \lambda_2 = \lambda_3$). The FA is calculated using:

$$FA = \sqrt{\frac{3}{2}} \sqrt{\frac{(\lambda_1 - \lambda_m)^2 + (\lambda_2 - \lambda_m)^2 + (\lambda_3 - \lambda_m)^2}{\lambda_1^2 + \lambda_2^2 + \lambda_3^2}} \quad (2.46)$$

where λ_m is the mean of the eigenvalues (equations 2.44 - 2.45).

2.3 Blood Oxygen Level-Dependent Imaging

BOLD (blood oxygen level-dependent) imaging relies on the oxygenation status of the hemoglobin molecule as its endogenous contrast. Unlike the diamagnetic oxygen-bound hemoglobin molecule, oxyhemoglobin (oxyHb), deoxyhemoglobin (deoxyHb) is paramagnetic. Thus, the presence of deoxyHb results in local field distortions that can be detected in the MR signal. The ratio of oxyHb to deoxyHb in a given region is influenced by numerous factors including blood flow, blood volume, oxygen extraction and metabolism (Partovi et al., 2012).

Numerous methods are available to analyze the BOLD signal collected during an MR imaging session. In task based studies that evaluate the BOLD response before and after the subject is exposed to a stimulus, a fit is usually made between the collected BOLD signal and the predicted hemodynamic response function. This hypothesis driven approach requires an idealized waveform to be developed so that it can be used to model the response.

Another way of analyzing the BOLD signal is by evaluating the various characteristics of the signal's time course, as is done in studies that use cuff

compression for instance (Partovi et al., 2012; Jacobi et al., 2012). These characteristics could include the time it takes the signal to peak after the paradigm or the maximal BOLD signal reached (see figure 1.5). The collected BOLD time course can be analyzed manually by an operator or a model can be fit to the signal, allowing for the extraction of the various characteristics (Schewzow et al., 2012).

Recently, BOLD signals have been analyzed using fractal methods (Maxim et al., 2005; Wardlaw et al., 2008; Kiviniemi, 2009; Noseworthy et al., 2010; Wang et al., 2011). Fractal interpretation is a way of examining the complex fluctuations that such waveforms might exhibit, providing new insight into the underlying phenomena governing the signals.

To characterize a fractal structure, the dimension of the fractal is measured as it gives an indication of how the shape occupies space. Fractals have a fractional or noninteger dimension (Goldberger and West, 1987), unlike Euclidean structures that are characterized by integer dimensions. Thus, the dimension of Koch's curve (figure 2.15), which is an example of a fractal structure, is between that of a line (dimension =1) and that of a square (dimension =2).

A geometrical fractal, although a complex seeming structure, is actually the result of repetitive application of a certain algorithm. The second iteration

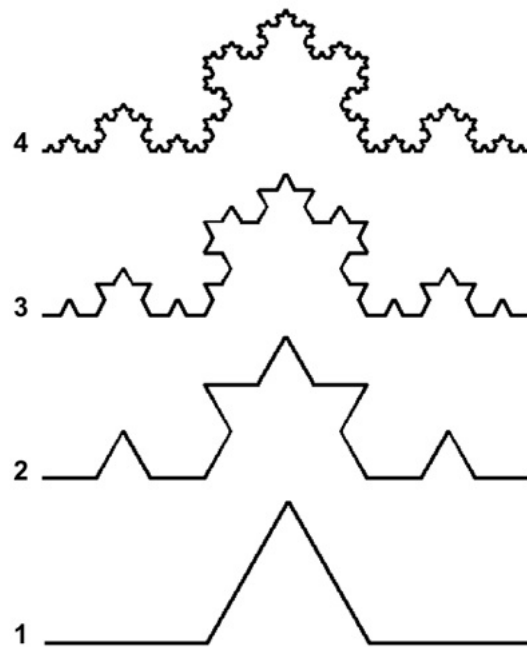


Figure 2.15: Koch's curve is an example of a geometrical fractal with a dimension of 1.26189. Shown are four iterations of the curve. At each iteration, replacement of the shape in step one in place of the line segments produces the curve of the next iteration.

of Koch's curve (figure 2.15), for instance, can be produced by starting with the initial shape (the generator or stage 1 of figure 2.15) and replacing each line segment with the generator. Subsequent generations can be produced by repeating this process.

Structures that exhibit fractal properties can be classified as being exact fractals or statistical fractals (Eke et al., 2002). Exact fractals are made of elements that are rescaled replicas of the whole shape, like Koch's curve (figure 2.15). Statistical fractals, on the other hand, do not look like exact reduced copies of the large shape, but exhibit statistical properties similar to those of the large shape, as do most biological signals showing fractal characteristics (Eke et al., 2002).

Several methods are available to compute the fractal dimension (FD) or the Hurst exponent, H , of a signal (Eke et al., 2000, 2002; Schepers et al., 2002; Delignières et al., 2005; Lopes and Betrouni, 2009; Eke et al., 2012). H and FD are related through (Bassingthwaight et al., 1994):

$$FD = 2 - H \tag{2.47}$$

Fractal analysis methods have been recently evaluated and it was demonstrated that a signal classification step must proceed the application of fractal analysis to ensure that the signal can be appropriately analyzed (Eke et al., 2000, 2002).

In all fractal techniques, the idea is that a randomly seeming signal may contain a complex pattern of correlations when examined using various time scales, thereby exhibiting self similarity. All fractal analysis methods have a set of common steps, although each approach may use a slightly different algorithm to evaluate the signal (Lopes and Betrouni, 2009). In any of the fractal techniques, certain properties of the signal (P) are first examined at various measurement scales (S). A power law scaling relationship defines all fractals such that:

$$\begin{aligned} P &\propto S^\xi \\ P &= cS^\xi \end{aligned} \tag{2.48}$$

where ξ is a negative scaling exponent and c is the proportionality constant (Eke et al., 2002). A plot of the logarithm of the examined property ($\log P$) versus the logarithm of the scale ($\log S$) then reveals a linear trend according to:

$$\log P = \log c + \xi \log S \tag{2.49}$$

By fitting a regression line through the plotted points, the slope of the line (ξ) allows for an estimation of the fractal dimension of the signal (Eke et al., 2002).

In order to apply the appropriate fractal analysis technique to a signal, the signal must first be classified using a dichotomic model (Eke et al.,

2000, 2002). In this model, a distinction is made between processes that are defined as fractional Brownian motions (fBm) and those that represent fractional Gaussian noise (fGn) (Eke et al., 2000). An fBm signal is one whose variance is not constant and increases with time, thereby making the signal nonstationary (Eke et al., 2002). An fGn signal, on the other hand, is a stationary signal whose variance is constant over time. Signals in physiology are generally classified as fBm as they tend to be nonstationary (Eke et al., 2002).

Fractal analyses can be applied to the collected data either in the frequency domain or in the time domain (Eke et al., 2002). The frequency domain approach is a simple one, requiring the fast Fourier transform of the signal to be computed, from which the power spectral amplitude, $|A|$, can then be determined. For a fractal signal,

$$|A|^2 \propto \frac{1}{f^\beta} \tag{2.50}$$

$$|A|^2 = \frac{c}{f^\beta}$$

where f is the frequency, β is referred to as the spectral index and c is the proportionality constant (Eke et al., 2002). Plotting the logarithm of the squared amplitude against the logarithm of the frequency should reveal a linear fit in the case of a fractal signal. The negative of the fitted slope is then a

measure of the spectral index. The FD can be obtained from the spectral index using:

$$\begin{aligned}
 FD &= 2 - \frac{(\beta+1)}{2} \text{ for fGn signals} \\
 FD &= 2 - \frac{(\beta-1)}{2} \text{ for fBm signals}
 \end{aligned}
 \tag{2.51}$$

Although this method is sometimes used in literature to find the fractal dimension of a signal, the technique is not accurate (Iyengar et al., 1996; Eke et al., 2000). Thus, preprocessing steps have been proposed to improve the accuracy of this frequency domain approach (Eke et al., 2000). These steps include removing the mean of the series from the value of each time point and then applying a parabolic window. End matching (or bridge detrending) follows, where the line connecting the first and last points of the signal is removed from the data (Eke et al., 2000). By applying these steps, a fractal signal should show a linear trend on a double logarithmic plot. If this pattern persists over a two decade range, fractal analysis should be undertaken (Eke et al., 2000).

The first step in fractal analysis, after observing a non-zero β exponent on a log-log plot of the squared fourier amplitude versus frequency is to determine $\hat{\beta}$. This spectral index is obtained by excluding high frequencies ($f > 1/8$) when fitting for β . The preprocessing steps and the inclusion of only low frequencies in the fit have been given the term $^{low}PSD_{we}$ (Eke et al., 2000). The next processing steps depend on the obtained value for $\hat{\beta}$, as shown in

figure 2.16. If $\hat{\beta}$ is between -1 and 0.38, then the signal is classified as fGn and the appropriate method of finding FD (or the Hurst exponent, H) is by using dispersional analysis (Eke et al., 2000). This method involves reshaping the signal, or $X(t)$, by binning adjacent points into groups. For each grouping (of size n) the mean is calculated. The standard deviation of all the group means, σ is then computed and obeys the relation (Eke et al., 2002):

$$\begin{aligned}\sigma &\propto n^{H-1} \\ \sigma &= cn^{H-1}\end{aligned}\tag{2.52}$$

where c is a proportionality constant and H is the Hurst exponent ($FD=2-H$).

Taking the logarithm of both sides of equation 2.54 gives:

$$\log \sigma = \log c + (H - 1) \log n\tag{2.53}$$

Thus, on a double logarithmic plot of σ versus n , the slope represents $H-1$, from which H or FD can be easily determined.

If, on the other hand, $\hat{\beta}$ is between 1.04 and 3 (figure 2.16), the signal is classified as fBm and the appropriate method of finding H (or FD) is using bridge detrended scaled windowed variance, bdSWV, analysis (Eke et al., 2000). Scaled windowed variance begins by dividing the signal into non overlapping segments, as is done in the dispersional method. For each grouping

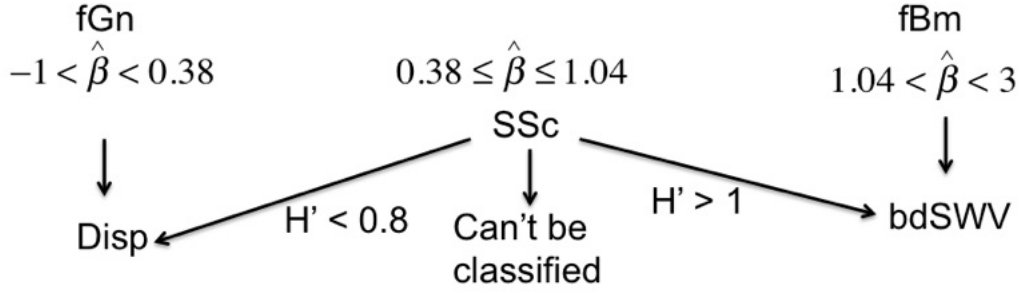


Figure 2.16: Flow chart showing the analysis steps once a signal has been determined to be fractal, according to the procedure of Eke and colleagues (Eke et al., 2000). Depending on the obtained value of $\hat{\beta}$ from the $^{low}PSD_{we}$ technique, the signal may be classified as fGn or fBm. For an fGn signal, dispersional (Disp) analysis can be used to compute the fractal dimension. For an fBm signal, the fractal dimension is calculated using the bridge detrended scaled windowed variance (bdSWV) method. If a signal falls in the middle region, signal summation conversion (SSC) has to be used to find the class of the signal and then perform the appropriate analysis.

(of size n) the standard deviation is calculated. The average of all of the group standard deviations, $\bar{\sigma}$, is then computed and obeys (Delignières et al., 2005):

$$\bar{\sigma} \propto n^H \tag{2.54}$$

$$\bar{\sigma} = cn^H$$

where c is a proportionality constant and $H=2-FD$. Eke recommends bridge detrending the signal before applying the scaled windowed variance analysis (Eke et al., 2000).

Finally, If $\hat{\beta}$ falls in the middle region between that of fGn and fBm, the signal must first be converted using a signal summation conversion (SSC)

process (Eke et al., 2000). This requires cumulatively summing the original signal, $x(t)$, to obtain the summed signal, $Y(t)$:

$$Y(t_N) = \sum_{i=1}^N x(t_i) \quad (2.55)$$

The bdSWV method is then applied to the summed signal and based on the value H' (the computed slope obtained from the double logarithmic plot of $\bar{\sigma}$ versus n), the signal can be classified as fGn or fBm (figure 2.16). If H' is smaller than 0.8, the signal is fGn and disperional analysis may be used to find the fractal dimension. If, on the other hand, H' is greater than 1, the signal is classified as fBm and bridge detrended scaled windowed variance can be used to analyze it. If the signal does not belong to either of these two classes, then the above approaches can not be used to determine the fractal dimension, as they require the signal to be first classified. In such a case, techniques that are class-independent may be used (Eke et al., 2002).

Chapter 3

Problem Definition and Thesis Objectives

Diffusion tensor imaging (DTI) allows for the assessment of skeletal muscle microstructure non-invasively by probing the diffusion of water molecules. Blood oxygen-level dependent (BOLD) imaging provides information about tissue oxygenation using deoxyhemoglobin as its endogenous contrast agent. In the lower limb, DTI and BOLD investigations are most commonly applied to study the calf region. This thesis had four objectives that were centered around understanding baseline DTI and/or BOLD values in the lower limb (calf and foot muscles) of healthy subjects.

DTI studies of the calf have been performed by numerous groups. Earlier studies were set out to establish a normative range of DT metrics in healthy populations and to characterize the diffusive properties of the calf muscles. DT indices have also been shown to be sensitive to many factors that affect muscle microstructure, including exercise, diseases and changes in ankle positioning, as has been described in section 1.2. BOLD studies of the calf provide insight into muscle oxygenation and can aid in understanding the functional status of

muscle tissue. A number of parameters have been shown to impact the BOLD response in skeletal muscle, including vascular volume, oxygen consumption and blood flow, as has been described in section 1.3.

Even though DTI indices in the calf have been shown to alter in response to various ankle positions, no studies exist in literature that evaluate whether DTI metrics are modified due to movement from upright to supine position. In addition, there is no reported data on the effect of position changes on BOLD signal characteristics. A search through the literature reveals that a few studies try to standardize posture before data collection. Some BOLD studies that investigate muscle tissue oxygenation using ischemia-hyperemia set-ups tend to mention a resting time of five to fifteen minutes in the supine position before MR scanning (Partovi et al., 2012, 2013). Also, one BOLD study assessing the post contractile BOLD response reported a twenty minute supine rest before data acquisition (Slade et al., 2011). Some imaging protocols that examine muscle cross sectional area report a one hour resting period in the supine position (Trappe et al., 2001).

The first objective of the thesis was to investigate whether calf muscle microstructure, as measured by DTI metrics (eigenvalues, FA and ADC), is sensitive to postural manipulation involving movement from standing to recumbent position. The second objective of the thesis was to examine whether

resting BOLD signal characteristics (signal intensity, standard deviation, fractal dimension (FD) and underlying frequency components) are modified by the same postural change. To test these speculations, we measured DTI and BOLD signal metrics in the calf during an initial imaging session that followed upright posture (baseline) and during two consecutive imaging sessions at thirty and sixty minutes of supine rest. We hypothesized that these indices would differ between the three measurement sessions, because position-related changes in fluid volume distributions (Thompson et al., 1928; Hagan et al., 1978; Maw et al., 1995) have been previously reported. In addition, measurable changes have been noted in leg volume and muscle cross sectional area with posture (Waterfield, 1931; Berg et al., 1993; Conley et al., 1996).

To our knowledge, the effect of supine rest on calf muscle DTI and BOLD indices has not been previously investigated. It seems that some researchers are aware of the fact that postural changes influence the distribution of body fluids and attempt to standardize posture by having the subjects lay in the supine position for a predetermined time period (ranging from five minutes to an hour). However, no study has formally investigated the response of BOLD and DTI indices to postural manipulation.

The third objective of the thesis was to examine foot muscles of healthy subjects using diffusion tensor imaging. This is because lower limb DTI studies

have only been performed in the thigh and calf region. However, foot tissue is known to be compromised by a number of diseases (Greenman et al., 2005; Hulsman et al., 2009). Since DTI has not been performed in this body region, it is necessary to establish diffusion metrics (eigenvalues, FA and ADC) in a disease free population so that the technique can later be extended to foot muscles affected by various pathologies.

Based on the results of the first objective of the thesis, mainly that 34 minutes of supine rest seemed to be necessary to allow DTI indices to stabilize and that the BOLD signal did not seem to be sensitive to small differences in muscle use between the two postural states, the final objective of the thesis was to investigate whether diffusion tensor metrics of the foot were altered in response to movement from standing to supine position. In this fourth investigation, we measured DT indices in foot muscles at baseline and at 34 minutes of supine rest.

3.1 Summary of Objectives

The objectives of the thesis can be summarized into the following four main components, where each imaging experiment is carried out in young, healthy subjects:

- Examination of whether DT metrics (eigenvalues, ADC and FA) are modified in calf muscles (anterior tibialis, posterior tibialis, soleus, medial gastrocnemius, and lateral gastrocnemius) in response to movement from upright to supine position by tracking the metrics for an hour after posture change.
- Investigation of whether BOLD metrics (mean signal intensity, standard deviation, fractal dimension, underlying frequency components) are modified in calf muscles (anterior tibialis, posterior tibialis, soleus, medial gastrocnemius, and lateral gastrocnemius) following posture change from standing to the supine position.
- Examination of foot muscles (quadratus plantae, abductor hallucis, flexor hallucis brevis, flexor digitorum brevis, and abductor digiti mini) using diffusion tensor imaging to establish a normal range of DT indices in this region of the body in healthy subjects.
- Assessment of whether DTI metrics (eigenvalues, ADC and FA) in foot muscles (quadratus plantae, abductor hallucis, flexor hallucis brevis, flexor digitorum brevis, and abductor digiti mini) are affected by movement from upright to supine posture.

Chapter 4

Assessment of Diffusion Tensor Imaging Indices in Calf Muscles Following Postural Change from Standing to Supine Position

Alyaa H. Elzibak, B.Sc., M.Sc., Michael D. Noseworthy, Ph.D., P.Eng.

4.1 Context of the Paper

Diffusion tensor imaging (DTI) has been shown to be sensitive to microstructural changes in skeletal muscles. Many groups have used the technique to investigate water diffusivity changes that arise from various ankle positions (Deux et al., 2008; Hatakenaka et al., 2008; Schwenzer et al., 2009; Okamoto et al., 2010; Sinha and Sinha, 2011; Sinha et al., 2011) or accompany muscle injuries (Zaraiskaya et al., 2006; Heemskerk et al., 2006, 2007; Qi et al., 2008). Changes in posture have been reported to modify fluid distributions in the body (Thompson et al., 1928; Hagan et al., 1978; Maw et al., 1995) and affect limb measured quantities such as volumes and cross sectional area (Waterfield, 1931; Berg et al., 1993; Conley et al., 1996). In this manuscript, we

used DTI to examine water diffusivity changes in calf muscles that accompany movement from upright to supine position.

4.2 Declaration Statement

Alyaa H. Elzibak, as principle author, wrote the first draft of the article, performed all data and statistical analyses, and created figures/ tables as appropriate. Michael D. Noseworthy, as corresponding author, provided the concept for the paper, funding and advice. He also edited the manuscript and completed the online submission process of the paper.

This paper has been accepted for publication on November 15, 2013 in the journal *Magnetic Resonance Materials in Physics, Biology and Medicine* (*Magn Reson Mater Phy*), commonly known as *MAGMA*. Permission to reprint this work has been kindly granted on November 27, 2013 from Springer Science and business Media.

Elzibak AH and Noseworthy MD. Magn Reson Mater Phy. (2013) DOI 10.1007/s10334-013-0424-1.

4.3 Paper

Assessment of diffusion tensor imaging indices in calf muscles following postural change from standing to supine Position

Alyaa H. Elzibak¹, Michael D. Noseworthy^{1,2,3,4*}

¹*Department of Medical Physics and Applied Radiation Sciences, McMaster University, Hamilton, Ontario, Canada.*

²*School of Biomedical Engineering, McMaster University, Hamilton, Ontario, Canada.*

³*Department of Electrical & Computer Engineering, McMaster University, Hamilton, Ontario, Canada.*

⁴*Department of Radiology, McMaster University, Hamilton, Ontario, Canada.*

*Corresponding author:

Dr. Michael D. Noseworthy, Ph.D., P.Eng.

Department of Electrical and Computer Engineering,
McMaster University, 1280 Main St. West, Hamilton,
ON L8S 4K1, Canada.

email: nosewor@mcmaster.ca

4.3.1 Abstract

Object: To investigate whether postural change from erect to recumbent position affects calf muscle water diffusivity.

Materials and Methods: Ten healthy adults (27.2 ± 4.9 years, 3 females) were imaged at baseline (following assumption of recumbent position), and after 34 min (session 2) and 64 min (session 3) of laying supine within a 3T MRI scanner. Diffusion tensor imaging (DTI) eigenvalues, fractional anisotropy (FA) and apparent diffusion coefficient (ADC) were evaluated in five calf muscles (anterior and posterior tibialis and triceps surae) during each of the three imaging sessions.

Results: Significant decreases were observed in all of the eigenvalues and ADC in each of the muscles with postural change. These reductions ranged from 3.2 to 6.7 % and 3.4 to 7.5 % for the various DTI metrics, following 34 and 64 min of supine rest, respectively ($P < 0.05$). No significant differences were noted in ADC or eigenvalues between the second and third imaging sessions for any muscle. FA did not change significantly with postural manipulation in any muscle compartment.

Conclusion: DTI indices were altered with postural change. As differences were not apparent between the latter two imaging sessions, we suggest a short

supine resting period (~ 34 min) is sufficient for muscle diffusivity to stabilize prior to quantitative MR imaging in healthy young adults.

Keywords: Diffusion tensor imaging (DTI), Skeletal muscle, Supine posture

4.3.2 Introduction

Considerable interest has been shown in investigating skeletal muscle microstructure noninvasively using diffusion tensor imaging (DTI). DTI provides information about tissue structure by probing the diffusion of water molecules using diffusion encoding gradients. Due to the anisotropic structure of skeletal muscle fibers, various groups have used DTI to study healthy calf muscles [1-11]. DTI has also been applied to evaluate calf muscle injuries [12] and thigh muscle disruptions due to eccentric exercise [13]. To describe the diffusivity of water within a given region of interest (ROI), a number of diffusion indices can be calculated from the diffusion tensor dataset [14]. These include three eigenvalues ($\lambda_1, \lambda_2, \lambda_3$) that provide information about diffusion magnitude along a given direction (represented by eigenvectors), fractional anisotropy (a combined metric of all three eigenvalues that describes the shape of the diffusion ellipsoid) and the apparent diffusion coefficient or the mean diffusivity (ADC or MD).

Although some groups have assessed the reproducibility of DTI metrics in the calf by investigating the changes that accompany ankle positioning [6, 7], no study has looked at whether DTI indices (eigenvalues, ADC or FA) are altered with movement from the erect to the recumbent position. Changes in posture from standing to supine are known to influence the distribution of

body fluids [15-17]. Specifically, upon assuming a horizontal position, increases in intravascular volume are observed [15,16] that are likely due to movement of fluid from the interstitial space into this compartment [15]. Shifts in bodily fluids due to postural manipulations are accompanied by alterations in limb volumes [18-20] and are known to influence the measured skeletal muscle cross-sectional area (CSA) [19, 20]. Calf muscle CSA change due to supine rest has been previously investigated using computed tomography (CT) and magnetic resonance imaging (MRI) [19, 20]. It has been suggested that a resting period of an hour might be necessary [19] before assessment of lower limb muscle CSA to ensure effects of fluid shift can be minimized. Thus, many protocols that investigate thigh or calf muscle CSA require subjects to remain in a horizontal position for sixty minutes before conducting the study [21].

Besides studies that evaluate muscle CSA, standardization of posture is also done in some blood oxygen-level dependent (BOLD) MR studies [22-24]. Vascular filling and draining have been shown to affect BOLD contrast during post ischemia reactive hyperemia protocols of the calf muscles [25]. Thus, studies that probe muscle tissue oxygenation using ischemia-hyperemia BOLD paradigms usually report a 5-min resting time in the supine position before data collection [23, 24]. To our knowledge, the effect of supine rest on calf muscle DTI indices has not been previously investigated. Since postural

changes are known to influence the distribution of body fluids, the goal of this work was to assess the response of DTI indices (eigenvalues, FA and ADC) to postural manipulation. We studied DTI metrics in calf muscles at baseline (immediately following assumption of supine rest) and at 34 min and 64 min of supine rest.

4.3.3 Materials and methods

4.3.3.1 Subjects and experimental design

Ten healthy adult subjects between 22 and 37 years of age (mean \pm SD: 27.2 ± 4.9 years, 3 females) took part in this study, approved by our institutional review board. Participants were asked to fast for at least 4 h prior to the study. All images were acquired while subjects lay in a supine position. Subjects were instructed to remain still during the scanning session. The calf muscles of the subject's dominant leg were positioned feet first within the coil in such a way as to avoid restricting any blood vessels. Leg dominance was self-reported by each subject. A wooden footrest (Fig. 4.1) was used to immobilize the foot and ensure the subject's ankle was in a neutral position for all scans. Data were collected from the region with the largest calf diameter, approximately at 66% of the tibia length (from the distal end). This region was visually selected after scout images were acquired of the calf.

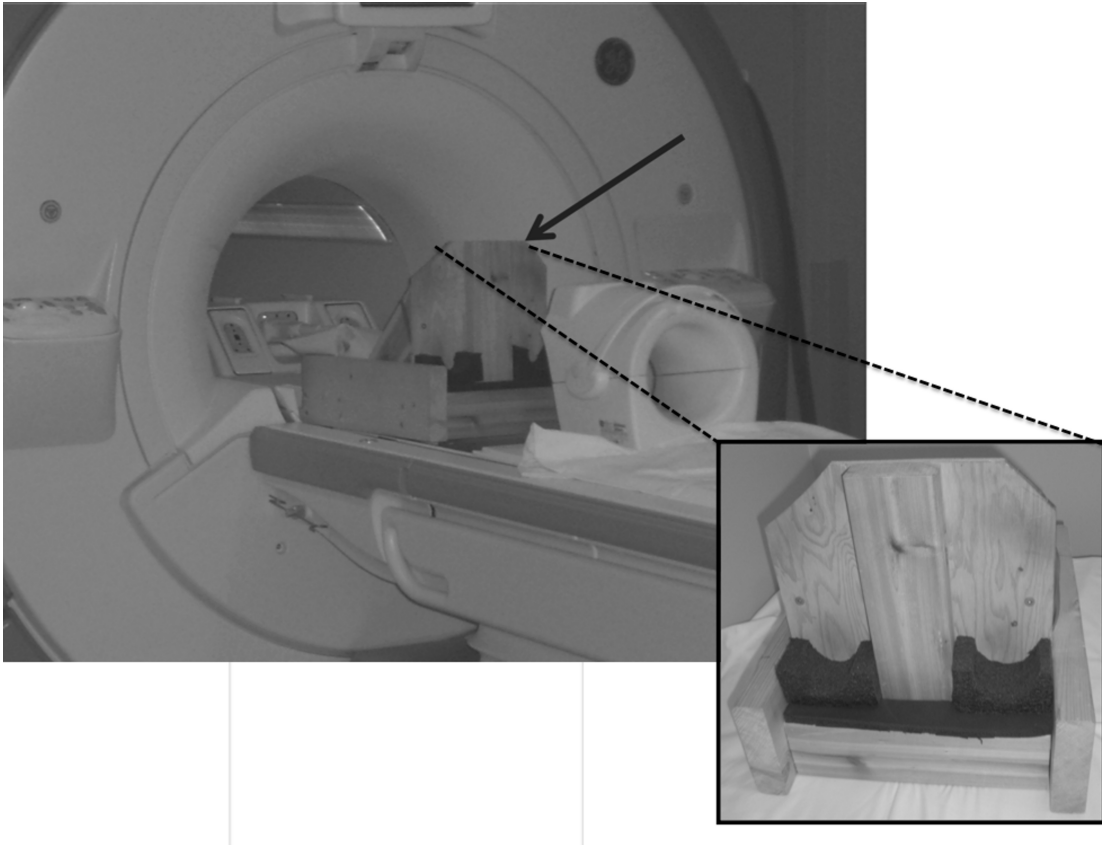


Figure 4.1: Wooden footrest used to suspend the calf muscles (*arrow*). Each foot is placed on the designated spot within the footrest and an 8-channel knee coil (shown in *front* of the footrest) surrounds the thickest part of the calf of the dominant leg.

Immediately following arrival to the imaging centre, subjects were asked to change into a cotton hospital gown and positioned on the MRI table. Following baseline MRI measurements (session 1), images were acquired at 34 min (session 2) and 64 min (session 3) of supine rest. Subjects remained on the imaging table in the MRI scanner during the entire imaging study, with their leg in the immobilizing footrest. The MRI table was also not moved for the duration of the experiment. This helped ensure that the subjects were positioned in the same location for all image acquisitions.

4.3.3.2 Magnetic resonance imaging

Imaging was performed using a 3.0T MRI system (MR750, GE Healthcare, Milwaukee, WI) and an eight-channel phased array knee coil. High contrast, T1-weighted axial anatomical images were collected using a Fast Spin Echo (FSE) sequence with the following parameters: TE/TR= 14.9/707ms, 5mm slice thickness, 0mm gap, FOV=16cm, 320x320 matrix, 20 slices, Echo Train Length (ETL)=4, scan time=2.05 minutes. Subsequent DTI images were collected from the same anatomical location as the T1-weighted images.

Diffusion weighted images were acquired using a dual spin spin-echo EPI sequence with the following parameters: 15 optimized diffusion encoding gradients, b value = 400 s/mm^2 , ASSET factor = 2, TE/TR= 68.8/6000ms,

Table 4.1: The fifteen gradient directions used in the DTI acquisition

Gradient	Gradient directions (Dx, Dy, Dz)
1	(1,0,0)
2	(0.643, 0.766, 0)
3	(0.258, 0.307, 0.916)
4	(0.745, -0.594, 0.303)
5	(0.164, -0.507, 0.846)
6	(-0.796, -0.321, 0.513)
7	(0.761, 0.427, 0.489)
8	(-0.506, 0.833, 0.224)
9	(0.667, -0.158, 0.728)
10	(0.128, 0.959, 0.254)
11	(-0.178, -0.898, -0.403)
12	(0.255, -0.590, -0.767)
13	(0.340, -0.736, 0.585)
14	(-0.801, 0.329, 0.501)
15	(0.336, 0.043, -0.941)

5mm slice thickness, 0mm gap, FOV=16cm, 64x64 matrix, 20 slices, 4 NEX, total scan time=6.08 minutes. The fifteen diffusion gradients that were applied are listed in Table 4.1. To calculate the diffusion tensor, one $b = 0 \text{ s/mm}^2$ image was also collected. Each NEX was acquired separately so eddy current and motion correction could be applied before merging and subsequent tensor calculation (details below).

4.3.3.3 Data analysis

Even though all the volunteers were healthy young adults, prior to analysis, images were visually inspected to rule out any subclinical gross pathology. DTI derived metrics (eigenvalues, ADC and FA) were investigated in five calf muscles: the triceps surae (the two heads of the gastrocnemius and the soleus) and the anterior and posterior tibialis (Fig. 4.2). Analysis was completed offline using a home-developed Bourne-again shell (BASH) script that calls the FMRIB Software Library, FSL [26], analysis tools. An affine transform was employed to correct for eddy current distortion using the FSL *eddy_correct* function, which is based on the FMRIB's Linear Image Registration Tool, FLIRT [27]. FLIRT was also employed for motion correction. Both eddy current and motion correction were applied with the reference being the $b=0$ s/mm^2 image of the first NEX. Calculation of the diffusion tensor followed eddy current and motion correction and was done using the analysis of functional neuro-images (AFNI) software [28]. At each voxel, diagonalization of the tensor produced the eigenvalues ($\lambda_1, \lambda_2, \lambda_3$). ADC and FA were then computed as:

$$\text{ADC} = \frac{\lambda_1 + \lambda_2 + \lambda_3}{3} \quad (4.1)$$

$$\text{FA} = \sqrt{\frac{3}{2}} \sqrt{\frac{(\lambda_1 - \langle \lambda \rangle)^2 + (\lambda_2 - \langle \lambda \rangle)^2 + (\lambda_3 - \langle \lambda \rangle)^2}{\lambda_1^2 + \lambda_2^2 + \lambda_3^2}} \quad (4.2)$$

where $\langle \lambda \rangle$ represents the mean of the three eigenvalues.

A single slice (at the thickest part of the calf) was analyzed for each subject, at each time point (i.e. identical slice over the three time points). Region of interest drawing and extraction of DTI measures was done using AFNI [28]. Care was taken to exclude blood vessels and fat when drawing ROIs, as non-muscle tissues have been shown to have different diffusion properties [29-31].

4.3.3.4 Statistical analysis

One-way repeated measures analysis of variance (ANOVA) was used to determine whether each of the investigated MRI metrics varied across time. Statistical significance level was defined as $P < 0.05$. If significance was achieved, the main effects were further examined using the Tukey honestly significant difference (HSD) post hoc test. Statistical analyses were performed using GraphPad Prism (Version 5.0c, GraphPad Software Inc., La Jolla, CA).

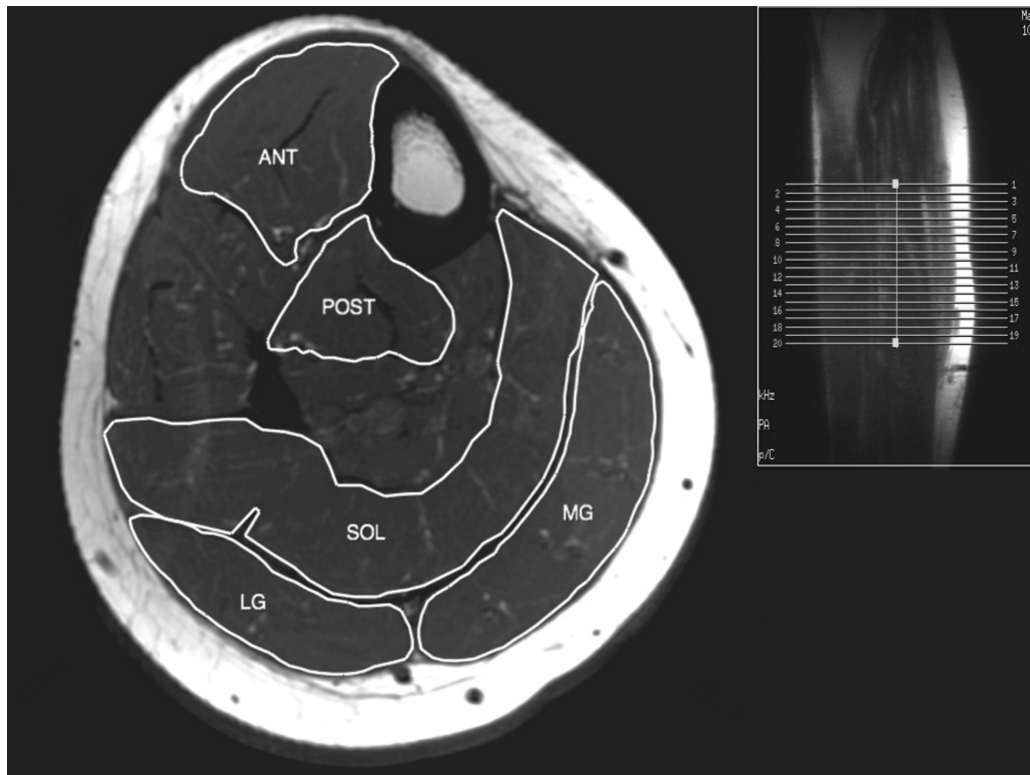


Figure 4.2: Axial T1-weighted image showing the calf muscles investigated in this study: anterior tibialis (ANT), posterior tibialis (POST), soleus (SOL), medial gastrocnemius (MG) and lateral gastrocnemius (LG). In the *upper corner*, a sagittal localizer is shown, from which twenty axial slices were prescribed.

4.3.4 Results

The average eigenvalues from each muscle group over the three consecutive imaging time points are shown in Fig. 4.3a-c. With regards to λ_1 (Fig. 4.3a), the mean over all subjects was 2.17 ± 0.02 (SE) $\times 10^{-3}$ mm²/s in the anterior tibialis muscle at baseline. There was a marked decrease ($P < 0.05$) in this value by $3.6 \pm 1.2\%$ and $4.6 \pm 1.4\%$ following 34 minutes and 64 min of supine rest, respectively. However, no significant change was observed between the latter two imaging times. A similar pattern was found in the remaining four muscle groups, as well as the two other eigenvalues (Table 4.2).

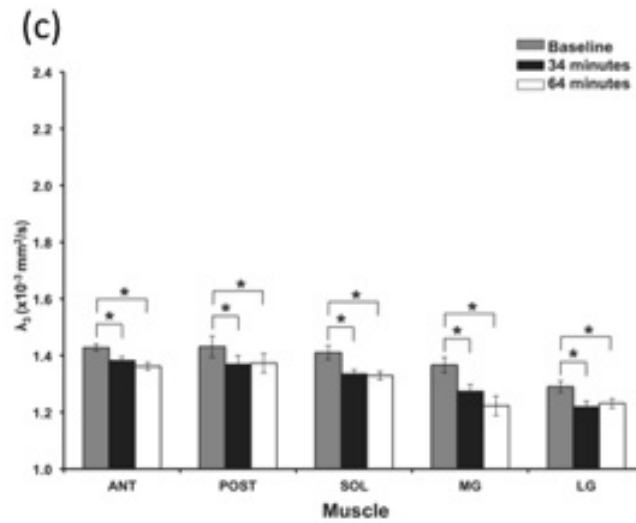
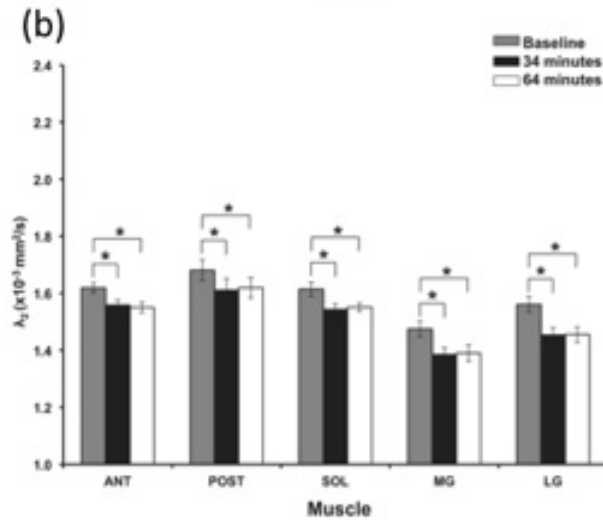
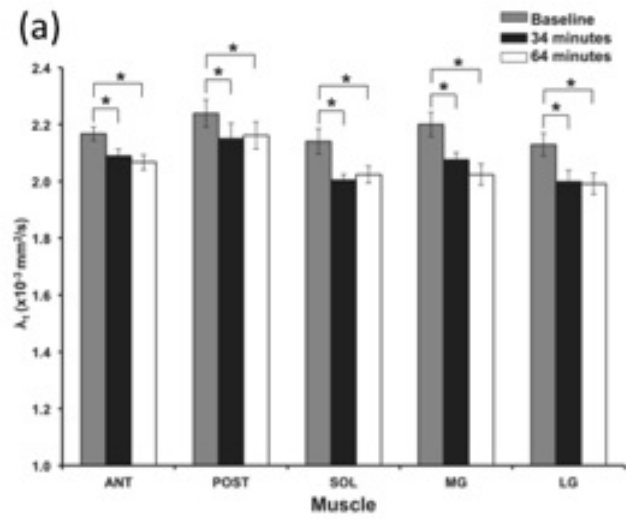


Figure 4.3: **a** The mean of the first eigenvalue, λ_1 , for each of the five calf muscles at the three imaging sessions. *Vertical error bars* represent the standard error among subjects. *Significant reductions ($P < 0.05$) were observed between baseline (i.e. session 1) and 34 min of supine rest and between baseline and 64 min of supine rest. We did not see any measurable changes between the latter two imaging sessions. (*ANT* anterior tibialis, *POST* posterior tibialis, *SOL* soleus, *MG* medial gastrocnemius, *LG* lateral gastrocnemius). **b** The averaged second eigenvalue, λ_2 (n=10 subjects, *error bars* represent SE) for all muscle groups following 34 and 64 min of supine rest. *Significant decreases ($P < 0.05$) between baseline and 34 min of supine rest and between baseline and 64 min of supine rest were noted for all muscles. (*ANT* anterior tibialis, *POST* posterior tibialis, *SOL* soleus, *MG* medial gastrocnemius, *LG* lateral gastrocnemius). **c** The mean of the third eigenvalue, λ_3 , for each of the five calf muscles at the three imaging sessions. *Vertical error bars* represent the standard error among subjects. *Significant reductions ($P < 0.05$) were observed between baseline (i.e. session 1) and 34 min of supine rest and between baseline and 64 min of supine rest. (*ANT* anterior tibialis, *POST* posterior tibialis, *SOL* soleus, *MG* medial gastrocnemius, *LG* lateral gastrocnemius)

Figure 4.4 shows the mean ADC values from all muscle groups at baseline and for the imaging sessions starting at 34 and 64 min of supine rest. As with the eigenvalues, marked decreases ($P < 0.05$) were observed in the ADC following 34 and 64 min of supine rest (Table 4.2). In addition, no significant changes were observed in ADC between the second and third imaging sessions for any muscle assessed.

The mean FA values in each muscle group for the three imaging sessions are shown in Fig. 4.5. At baseline, average FA over each muscle was 0.22 ± 0.01 (anterior tibialis), 0.23 ± 0.01 (posterior tibialis), 0.22 ± 0.01 (soleus), and 0.26 ± 0.01 and 0.25 ± 0.01 (medial and lateral gastrocnemius, respectively). The FA did not show any significant changes with time of supine posture for any muscle investigated (anterior tibialis $P=0.91$; posterior tibialis $P=0.87$; medial gastrocnemius $P=0.07$; lateral gastrocnemius $P=0.33$; soleus $P=0.31$).

4.3.5 Discussion

The goal of our study was to investigate whether postural change from standing to supine position affects the observed DTI metrics in calf muscles. To that end, we measured DTI indices (eigenvalues, FA and ADC) at baseline (immediately following assumption of recumbent position) and at 34 min and 64 min of supine rest. We observed significant decreases in all of the eigenvalues

Table 4.2: Baseline eigenvalues and ADC (mean \pm SE $\times 10^{-3}$ mm²/s; n=10 subjects) for all muscle groups and % decrease in baseline value following 34 and 64 min of supine rest

	Baseline	% decrease following 34 min of supine rest	% decrease following 64 min of supine rest
Anterior tibialis			
λ_1	2.17 \pm 0.02	3.6 \pm 1.2	4.6 \pm 1.4
λ_2	1.68 \pm 0.02	3.7 \pm 0.9	4.2 \pm 1.3
λ_3	1.43 \pm 0.01	3.2 \pm 0.9	4.6 \pm 0.8
ADC	1.74 \pm 0.01	3.5 \pm 1.0	4.5 \pm 1.1
Posterior tibialis			
λ_1	2.24 \pm 0.05	4.0 \pm 1.0	3.4 \pm 1.4
λ_2	1.68 \pm 0.03	4.3 \pm 1.2	3.6 \pm 1.2
λ_3	1.43 \pm 0.04	4.2 \pm 1.3	3.9 \pm 1.2
ADC	1.78 \pm 0.04	4.1 \pm 0.9	3.6 \pm 1.2
Soleus			
λ_1	2.14 \pm 0.04	6.1 \pm 1.6	5.3 \pm 1.1
λ_2	1.61 \pm 0.02	4.3 \pm 1.4	3.7 \pm 1.2
λ_3	1.41 \pm 0.02	5.2 \pm 1.5	5.6 \pm 1.6
ADC	1.72 \pm 0.03	5.3 \pm 1.4	4.9 \pm 1.1
Medial gastrocnemius			
λ_1	2.20 \pm 0.04	5.4 \pm 1.9	4.8 \pm 1.6
λ_2	1.47 \pm 0.03	6.0 \pm 1.7	5.7 \pm 1.0
λ_3	1.37 \pm 0.03	6.6 \pm 2.0	7.5 \pm 0.9
ADC	1.68 \pm 0.03	5.9 \pm 1.8	5.8 \pm 1.1
Lateral gastrocnemius			
λ_1	2.13 \pm 0.04	6.1 \pm 0.9	6.4 \pm 1.2
λ_2	1.56 \pm 0.03	6.7 \pm 1.5	6.6 \pm 1.7
λ_3	1.29 \pm 0.02	5.4 \pm 1.6	4.5 \pm 1.2
ADC	1.66 \pm 0.03	6.2 \pm 1.1	6.0 \pm 1.2

Significant decreases between baseline and 34 min and between baseline and 64 min ($P < 0.05$) were noted. However, no significant change was observed between the latter two imaging times

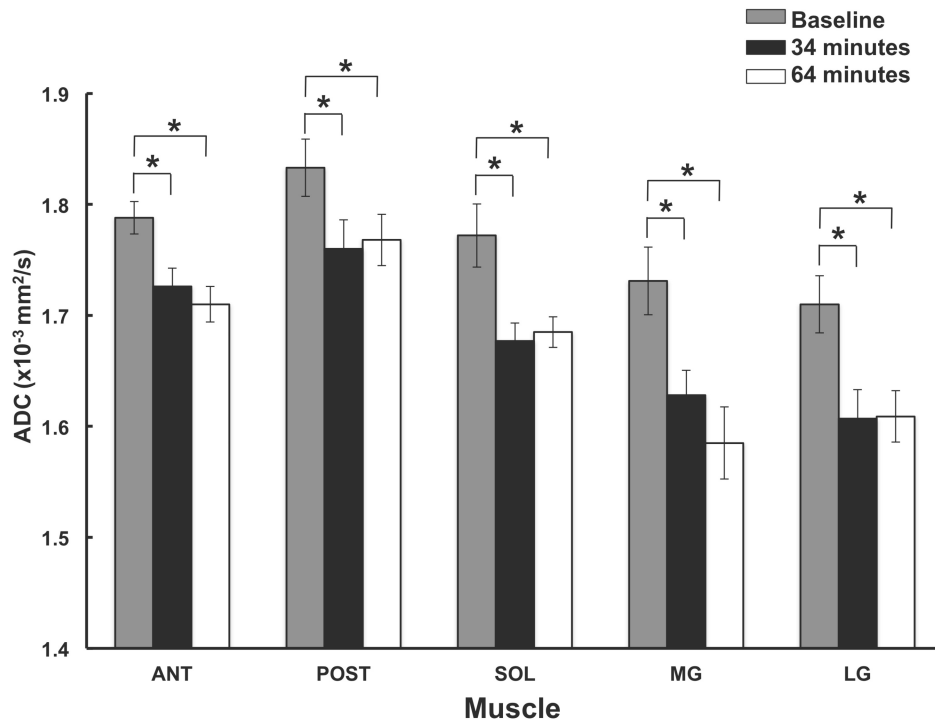


Figure 4.4: The averaged ADC (n=10 subjects, *error bars* represent SE) for all muscle groups following 34 and 64 minutes of supine rest. *Significant decreases ($P < 0.05$) between baseline and 34 minutes of supine rest and between baseline and 64 minutes of supine rest were noted for all muscles. (*ANT* anterior tibialis, *POST* posterior tibialis, *SOL* soleus, *MG* medial gastrocnemius, *LG* lateral gastrocnemius).

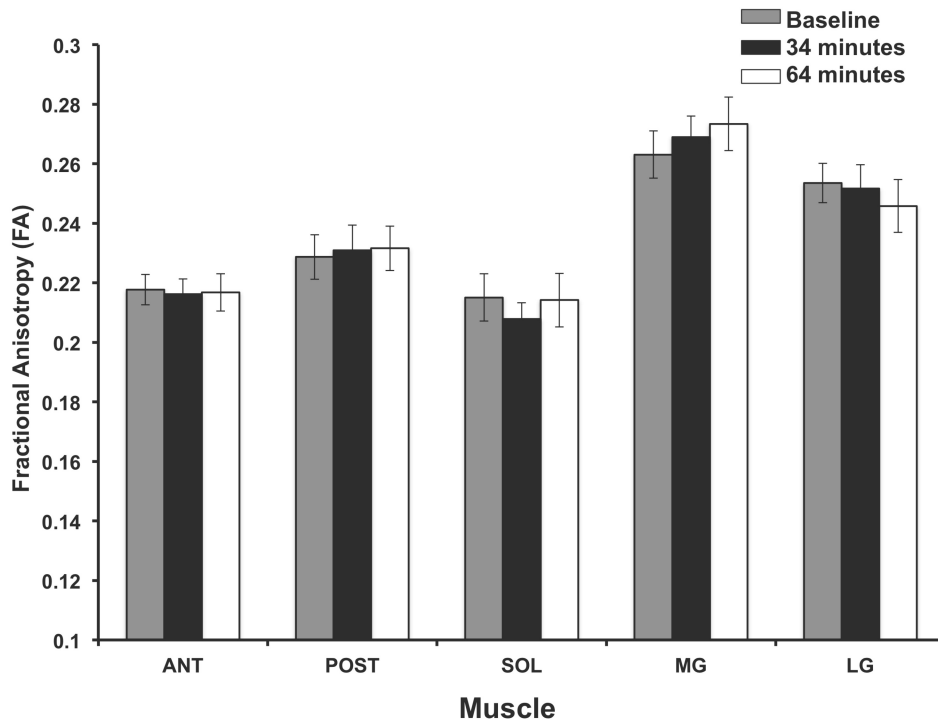


Figure 4.5: The mean FA for each of the five calf muscles at the three imaging sessions. *Vertical error bars* represent the standard error among subjects. No significant changes were observed in FA for any muscles (anterior tibialis $P=0.91$; posterior tibialis $P=0.87$; medial gastrocnemius $P=0.07$; lateral gastrocnemius $P=0.33$; soleus $P=0.31$). (*ANT* anterior tibialis, *POST* posterior tibialis, *SOL* soleus, *MG* medial gastrocnemius, *LG* lateral gastrocnemius).

(Fig. 4.3) and ADC (Fig. 4.4) in five calf muscles (anterior tibialis, posterior tibialis, soleus, medial gastrocnemius, and lateral gastrocnemius) following 34 and 64 min of supine rest ($P < 0.05$) (Table 4.2). No significant changes occurred in any of the eigenvalues or the ADC between the two latter imaging sessions for any of the muscles assessed (Figs.4.3, 4.4). In addition, we did not observe any changes in the FA for any muscle compartment with supine rest (Fig.4.5).

Many groups have reported resting DTI of healthy human calf muscle. Sinha et al. [4] observed values that ranged from 1.93×10^{-3} to 2.29×10^{-3} mm^2/s for λ_1 , 1.42×10^{-3} to 1.58×10^{-3} mm^2/s for λ_2 and 1.19×10^{-3} to 1.40×10^{-3} mm^2/s for λ_3 in various calf muscle groups. They found the ADC and FA to range between 1.53×10^{-3} to 1.67×10^{-3} mm^2/s and 0.18 to 0.33, respectively. For further comparison, Zaraiskaya et al. [12] reported values from 1.61×10^{-3} to 1.72×10^{-3} mm^2/s for λ_1 , 1.26×10^{-3} to 1.36×10^{-3} mm^2/s for λ_2 and 1.07×10^{-3} to 1.10×10^{-3} mm^2/s for λ_3 in calf muscles. An ADC range of 1.31×10^{-3} to 1.41×10^{-3} mm^2/s was observed in that study, with FA varying from 0.20 to 0.23 for calf muscles. In our current study, baseline λ_1 ranged from 2.13×10^{-3} to 2.24×10^{-3} mm^2/s , λ_2 was from 1.47×10^{-3} to 1.68×10^{-3} mm^2/s and λ_3 from 1.29×10^{-3} to 1.43×10^{-3} mm^2/s for the various calf muscles. Also, we measured ADC and FA ranges of 1.66×10^{-3}

to $1.78 \times 10^{-3} \text{ mm}^2/\text{s}$ and 0.22 to 0.26, respectively. Our observed results at baseline are in agreement with those obtained by Sinha et al. [4], and are slightly higher than those reported by Zaraiskaya et al. [12]. Although all three studies were conducted using a 3T MRI scanner, there were differences in the imaging parameters, such as number of gradient directions, b value, and TE/TR that could have impacted the results. Besides differences in imaging acquisitions, discrepancies might have arisen from the ROI selection process. In the study by Zaraiskaya et al. [12], the entire muscle was selected as the ROI. However, in both our study and that by Sinha et al. [4], small ROIs were carefully selected from each muscle to avoid the inclusion of non-muscle segments (fascia, fat, vessels). One last difference with our current study is the approach to data analysis; that of doing motion and eddy current corrections on each NEX prior to data merging and subsequent tensor calculation.

Diffusion imaging has been employed to understand skeletal muscle architecture and gain insight into various muscle diseases [1-13, 29, 30]. Characterization of the diffusive properties of calf muscles has revealed that different muscle groups have distinguishable DTI parameters [2, 4]. The dependence of calf muscle metrics on gender, pennation angle and muscle fiber length has also been demonstrated [3, 5-7]. Changes in eigenvalues, ADC and FA have been identified in calf muscle injury and the application of pressure [8, 12]. In

the present study, DTI metrics were measured at baseline and during two sessions starting at 34 minutes and 64 minutes of supine rest. Since dorsiflexion and plantar flexion have been shown to affect DTI measures [5-7], we used a footrest to ensure all subjects were imaged in a neutral position with the foot at a 90° angle relative to the leg.

There is no reported data on whether hydration state affects muscle DTI parameters in calf muscles. However, in kidney studies, baseline hydration status has been shown to affect the diffusion parameters [32, 33]. Since the influence of the hydration status on muscle DTI metrics remains to be investigated, we asked our subjects to fast for 4 h prior to the study (refrain from food and drink) in an attempt to standardize our baseline DTI measures. It should also be noted that none of our participants had engaged in vigorous exercise over the 24 h preceding the study.

Numerous groups have examined the changes that accompany postural manipulations by monitoring alterations in fluid volumes, hematocrit concentrations and muscle cross sectional area [15-20]. Hagan et al. [16] examined healthy young males (28 ± 4 (SD) years, $n=7$) during 35 min of supine rest followed by 35 min in the erect position. They observed an expansion of 6.4 % in venous blood volume and 11.7 % in the plasma volume at the end of the recumbent position with decreases of 7.0 % in the venous hemoglobin and

hematocrit concentrations. The group also noted that no significant differences were observed in the measured parameters between 20 minutes and 35 min of supine rest. A study by Maw et al. [15] reported a decrease of 5.1 % in plasma volume following movement from a seated position to an upright position in healthy young active men ($n = 8, 26 \pm 4$ (SD) years). This reduction was observed 15 minutes after subjects had switched to the standing position and no significant differences were found between the 15 min and 30 min measurements. The group also noted an accompanying significant expansion of the interstitial fluid volume. Although the study did not involve transitions from standing to a supine position, the movement from seated to supine position reflected an increase in the blood volume that was accompanied by a decrease in interstitial fluid volume. The tendency of an increase in the intravascular volume was presumed to reflect fluid movement away from the interstitial space [15].

Changes in leg volume have been reported following supine posture. Waterfield [18] showed that assuming a recumbent position results in decreases of the leg volume, where most of the change occurs in the first 40 min. It was also observed that several hours were required in order for the shrinkage to completely stabilize. Changes in calf muscle CSA following horizontal supine rest have also been measured using CT and MRI [19,20]. Berg et al. [19]

monitored calf muscle CSA changes during 120 min of supine rest in physically active young men ($n=7$, 27 ± 5 (SD) years). They found a decrease of 5.5 % in the CSA after two hours of supine rest and noted that most of the change took place within the first hour of rest, with no significant differences observed between 60 min and 120 min. The group also measured changes in fluid volume in the calf and reported losses of 5.8 and 9.2 % of fluid in the calf after 20 min and 60 min of rest, respectively [19].

In our study, we observed reductions in the three eigenvalues and ADC in all of the investigated muscles with the postural manipulation involving movement from erect to supine position. The decreases ranged from 3.2 to 6.7% and 3.4 to 7.5% for the various DTI metrics, following 34 and 64 min of supine rest, respectively ($P<0.05$). It is worth noting that no changes occurred in any of the eigenvalues or ADC between the second and third imaging sessions for any muscle group we evaluated. This finding suggests that the effects of fluid shifts associated with movement from standing to supine positions on DTI metrics are probably complete following 34 min of rest. This time needed for DTI indices to stabilize is in fair agreement with numerous studies that suggested changes accompanying postural manipulations are complete within 15-40 minutes [15, 16, 18]. However, some studies have shown that stability may require 60 min to be achieved [19].

DTI metrics are known to be influenced by the signal-to-noise ratio (SNR) [34, 35]. The SNR of our nonweighted image from all subjects in this study was (mean \pm SD): 79.2 ± 22.9 in the anterior tibialis muscle, 52.0 ± 18.7 in the posterior tibialis muscle, 55.2 ± 22.3 in the soleus muscle, 77.6 ± 33.2 in the medial gastrocnemius muscle and 95.0 ± 30.9 in the lateral gastrocnemius muscle. Based on the study by Froeling et al. [35], an SNR of at least 25 is needed to ensure the accuracy of the obtained DTI metrics. For further comparison, Damon's [34] simulations suggest that for the b value in the present study (400 s/mm^2), the largest SNR required for an accuracy level of 1 % in determining the eigenvalues and ADC is 28, while that needed for FA is 42 (from Fig. 3). For an accuracy level of 5 % in determining the DTI metrics, the largest SNR required is 21 (from Fig. 3) [34]. It is believed that the DTI metrics in the current study were determined with an accuracy of between 1 and 5 % since the obtained SNR for all muscles fell in that region. Although excellent SNR was obtained with the use of our selection of DTI parameters, higher in-plane resolution could have been achieved with the use of a larger matrix size and no parallel imaging without likely deleterious loss of SNR. We opted for higher SNR than better in-plane resolution, given the use of our resolution was sufficient for assessing healthy muscle tissue. Parallel imaging allowed shorter TE which translates to better SNR. Furthermore we

choose to use parallel imaging because the shorter echo-train length of the EPI readout minimizes geometric distortion and the magnitude of ghosting in the phase encoding direction. Future studies should consider increasing the in-plane resolution, especially when investigating pathological muscles, or those of elderly subjects, where fat infiltration becomes an issue and higher in-plane resolution might be needed to ensure accurate muscle inclusion.

T_2 of skeletal muscle has been shown to have a multi-exponential nature, with as many as four components that probably arise from macromolecules ($T_2 < 5$ ms), intracellular water molecules (2 components with $T_2 = 11$ and 39 ms) and extracellular water molecules ($T_2 = 114$ ms) [36]. Each of these proton pools, being separable, is classified as having intermediate exchange, with respect to the nuclear magnetic resonance (NMR) time scale of water. Since a TE of 68.8 ms was used in the DTI acquisition in the current study, the calculated DTI parameters include a mixture of both intra and extracellular water components, with more so being derived from the diffusion behavior of extracellular water. We assume this because a large portion of the signal from the intracellular component would have decayed by the time of readout sampling. Thus, the observed decrease in ADC with supine rest in the current study is assumed to be a consequence of reduced interstitial space impeding diffusion of water. It is known that ADC is influenced by the ratio of the volume that

cells occupy to the extracellular space volume, and also by the extracellular space composition [37]. Interstitial edema is associated with increased diffusion due to an increased extracellular space [37]. Since supine rest has been associated with increased intravascular blood volume [16] likely due to fluid movement away from the interstitial space [15], the decrease in ADC with supine rest observed in our study is presumably the consequence of a reduced extracellular space. The lack of change in FA for any muscles indicates that muscle tissue anisotropy was not altered with the postural manipulation and hence the overall shape of muscle diffusion ellipsoids remained constant.

Our study has several limitations that need mentioning, including the small sample size and the evaluation of only young healthy adults. It is known that aging affects calf muscular fat content [38] and water diffusivity [39] in healthy subjects. It has also been suggested that older subjects show less fluid shift with postural manipulations in comparison to young subjects [40]. With regards to pathological conditions, some diseases including hypoalbuminemia [41] have been shown to exhibit greater changes in blood volume with postural manipulation in comparison with healthy subjects. Thus, extension of the results of the current study to older populations or to people who suffer from vascular diseases could not be justified without further investigation.

4.3.6 Conclusion

In this study, we demonstrated that postural change from standing to supine position alters some DTI metrics in calf muscles. Specifically, we observed significant decreases in all of the eigenvalues and the ADC in the five calf muscles investigated, relative to baseline, following 34 and 64 min of supine rest. Since DTI indices were not significantly different between the second and third imaging sessions, we suggest 34 min of supine rest, prior to quantitative muscle MRI measurements as a sufficient length of time to establish resting tissue equilibrium in healthy young adults. Supine rest for at least 34 min prior to quantitative leg muscle diffusion tensor imaging could lead to more consistent and reliable results.

4.3.7 Acknowledgements

Funding for this work was provided from the Natural Sciences and Engineering Research Council (NSERC) of Canada doctoral postgraduate scholarship (PGS-D) (AHE). We also wish to acknowledge Andrew Davis for writing the BASH script, and Janet Burr, Cheryl Contant and Julie Lecomte for MRI technical assistance.

4.3.8 References

1. Damon BM, Ding Z, Anderson AW, Freyer AS, Gore JC (2002) Validation of diffusion tensor MRI based muscle fiber tracking. *Magn Reson Med* 48:97-104.
2. Galbán CJ, Maderwald S, Uffmann K, de Greiff A, Ladd ME (2004) Diffusive sensitivity to muscle architecture: a magnetic resonance diffusion tensor imaging study of the human calf. *Eur J Appl Physiol* 93:253-262.
3. Galbán CJ, Maderwald S, Uffmann K, Ladd ME (2005) A diffusion tensor imaging analysis of gender differences in water diffusivity within human skeletal muscle. *NMR Biomed* 18:489-498.
4. Sinha S, Sinha U, Edgerton VR (2006) In vivo diffusion tensor imaging of the human calf muscle. *J Magn Reson Imaging* 24:182-190.
5. Hatakenaka M, Yabuuchi H, Matsuo Y, Okafuji T, Kamitani T, Setoguchi T, Nishikawa K, Honda H (2008) Effect of passive muscle length change on apparent diffusion coefficient: detection with clinical MR imaging. *Magn Reson Med Sci* 7:59-63.
6. Sinha U, Sinha S, Hodgson JA, Edgerton RV (2011) Human soleus muscle architecture at different ankle joint angles from magnetic resonance diffusion tensor imaging. *J Appl Physiol* 110:807-819.

7. Sinha S, Sinha U (2011) Reproducibility analysis of diffusion tensor indices and fiber architecture of human calf muscles in vivo at 1.5 tesla in neutral and plantarflexed ankle positions at rest. *J Magn Reson Imaging* 34:107-119.
8. Hata J, Yagi K, Hikishima k, Komaki Y, Goto M, Yano K (2012) Diffusion fractional anisotropy-based transformation in skeletal muscle caused by pressure. *Magn Reson Med Sci* 11:179-184.
9. Saupe N, White LM, Sussman MS, Kassner A, Tomlinson G, Noseworthy MD (2008) Diffusion tensor magnetic resonance imaging of the human calf comparison between 1.5T and 3.0T- preliminary results. *Invest Radiol* 43:612-618
10. Okamoto Y, Kunimatsu A, Miki S, Shindo M, Niittsu M, Minami M (2008) Fractional anisotropy values of calf muscles in normative state after exercise: preliminary results. *Magn Reson Med Sci* 7:157-167
11. Okamoto Y, Kunimatsu A, Kono T, Nasu K, Sonobe J, Minami M (2010) Changes in MR diffusion properties during active muscle contraction in the calf. *Magn Reson Med Sci* 9:1-8
12. Zaraiskaya T, Kumbhare D, Noseworthy MD (2006) Diffusion tensor imaging in evaluation of human skeletal muscle injury. *J Magn Reson Imaging* 24:402-408.

13. Cermak NM, Noseworthy MD, Bourgeois JM, Tarnopolsky MA, Gibala MJ (2012) Diffusion tensor MRI to assess skeletal muscle disruption following eccentric exercise. *Muscle and Nerve* 46:42-50.
14. Noseworthy MD, Davis AD, Elzibak AH (2010) Advanced MR imaging techniques for skeletal muscle evaluation. *Semin Musculoskelet Radiol* 14:257-268.
15. Maw GJ, Mackenzie IL, Taylor NAS (1995) Redistribution of body fluids during postural manipulations. *Acta Physiol Scand* 155:157-163.
16. Hagan RD, Diaz FJ, Horvath SM (1978) Plasma volume changes with movement to supine and standing positions. *J Appl Physiol* 45:414-417
17. Thompson WO, Thompson PK, Dailey ME (1928) The effect of posture upon the composition and volume of the blood in man. *J Clin Invest* 5: 573-604.
18. Waterfield RL. The effect of posture on the volume of the leg (1931) *J Physiol* 72:121-123
19. Berg HE, Tender B, Tesch PA (1993) Changes in lower limb muscle cross-sectional area and tissue fluid volume after transition from standing to supine. *Acta Physiol Scand* 148:379-385.

20. Conley MS, Foley JM, Ploutz-synder LL, Meyer RA, Dudley GA (1996) Effect of acute head-down tilt on skeletal muscle cross-sectional area and proton transverse relaxation time. *J Appl Physiol* 81:1572-1577.
21. Trappe SW, Trappe TA, Lee GA, Costill DL (2001) Calf muscle strength in humans. *Int J Sports Med* 22:186-191.
22. Jacobi B, Bongartz G, Partovi S, Schulte AC, Aschwanden M, Lumsden AB, Davies MG, Loebe M, Noon GP, Karimi S, Lyo JK, Staub D, Huegeli RW, Bilecen D (2012) Skeletal muscle BOLD MRI: from underlying physiological concepts to its usefulness in clinical conditions. *J Magn Reson Imaging* 35:1253-1265.
23. Schulte AC, Aschwanden M, Bilecen D (2008) Calf muscles at blood oxygen level-dependent MR imaging: aging effects at postocclusive reactive hyperemia. *Radiology* 247:482-489.
24. Partovi S, Schulte AC, Aschwanden M, Staub D, Benz D, Imfeld S, Jacobi B, Broz P, Jäger KA, Takes M, Huegeli RW, Bilecen D, Walker UA (2012) Impaired skeletal muscle microcirculation in systemic sclerosis. *Arthritis Res Ther* 14:R209

25. Duteil S, Wary C, Raynaud JS, Lebon V, Lesage D, Leroy-Willig A, Carlier PG (2006) Influence of vascular filling and perfusion on BOLD contrast during reactive hyperemia in human skeletal muscle. *Magn Reson Med* 55:450-454.
26. Jenkinson M, Beckmann CF, Behrens TE, Woolrich MW, Smith SM (2012) FSL. *Neuroimage* 62:782-90.
27. Jenkinson M, Bannister P, Brady JM, Smith SM (2002) Improved optimisation for the robust and accurate linear registration and motion correction of brain images. *Neuroimage* 17:825-841.
28. Cox RW (1996) AFNI: software for analysis and visualization of functional magnetic resonance neuroimages. *Comput Biomed Res* 29:162-173.
29. Baur A, Reiser MF (2000) Diffusion-weighted imaging of the musculoskeletal system in humans. *Skeletal Radiol* 29:555-562
30. Qi J, Olsen NJ, Price RR, Winston JA, Park JH (2007) Diffusion-weighted imaging of inflammatory myopathies: polymyositis and dermatomyositis. *J Magn Reson Imaging* 27:212-217.
31. Williams SE, Heemskerk AM, Welch EB, Li K, Damon BM, Park JH (2013) Quantitative effects of inclusion of fat on muscle diffusion tensor mri measurements. *J Magn Reson Imaging*. doi: 10.1002/jmri. 24045

32. Muller MF, Prasad PV, Bimmler D, Kaiser A, Edelman RR (1994) Functional imaging of the kidney by means of measurement of the apparent diffusion coefficient. *Radiology* 193:711-715
33. Sigmund EE, Vivier P-H, Sui D, Lamparello NA, Tantillo K, Mikheev A, Rusinek H, Babb JS, Storey P, Lee VS (2012) Intravoxel incoherent motion and diffusion-tensor imaging in renal tissue under hydration and furosemide flow challenges. *Radiology* 263:758-769
34. Damon BM (2008) Effects of image noise in muscle diffusion tensor (DT)-MRI assessed using numerical simulations. *Magn Reson Med* 60:934-944
35. Froeling M, Nederveen AJ, Nicolay K, Strijkers GJ (2013) DTI of human skeletal muscle: the effects of diffusion encoding parameters, signal-to-noise ratio and T2 on tensor indices and fiber tracts. *NMR Biomed.* doi: 10.1002/nbm.2959
36. Saab G, Thompson RT, March GD (1999) Multicomponent T2 relaxation of in vivo skeletal muscle. *Magn Reson Med* 42:150-157
37. Fornasa F (2011) Diffusion-weighted magnetic resonance imaging: what makes water run fast or slow? *J Clin Imaging Sci* 1:27

38. Schwenzer NF, Martirosian P, Machann J, Schraml C, Steidle G, Claussen CD, Schick F (2009) Aging effects on human calf muscle properties assessed by MRI at 3 tesla. *J Magn Reson Imaging* 29:1346-1354
39. Galban CJ, Maderwald S, Stock F, Brauck K, Ladd ME (2006) Age dependence of water diffusivity in human skeletal muscle. In: *Proceedings of the 14th scientific meeting, International Society for Magnetic Resonance in Medicine, Seattle*, p 257
40. Miwa C, Sugiyama Y, Mano T, Matsukawa T, Iwase S, Tamkemas W, Kobayashi F (2000) Effects of aging on cardiovascular responses to gravity-related fluid shift in humans. *J Gerontol Med Sci* 55:M329-M335
41. Eisenberg S (1963) Postural changes in plasma volume in hypoalbuminemia. *Arch Internal Med* 112:140-145

Chapter 5

Analysis of Calf Blood Oxygen-Level Dependent (BOLD) Signal after Supine Posture

Alyaa H. Elzibak, B.Sc., M.Sc., Michael D. Noseworthy, Ph.D., P.Eng.

5.1 Context of the Paper

Having noted that diffusion tensor metrics of calf muscles are altered with position-related changes in the first manuscript (**chapter 4**), we were interested to examine the effect of posture on blood oxygen-level dependent (BOLD) calf signal characteristics. The BOLD signal represents contributions from vascular volume, blood flow and tissue oxygenation (Partovi et al., 2012; Jacobi et al., 2012; Noseworthy et al., 2003, 2010). Since fluid volumes have been shown to alter with posture, we examined BOLD signal characteristics in this manuscript during three measurement times. The first was collected following upright posture and the second and third were acquired after thirty minutes and sixty minutes of acquisition of the first measurement, respectively. One of the metrics that we examined, in addition to global signal metrics, was

the fractal dimension of the BOLD signal. This quantity has been shown to be sensitive to subtle fluctuations (Noseworthy et al., 2010).

5.2 Declaration Statement

This is a manuscript that has been prepared in final format. Alyaa H. Elzibak, as principle author, wrote the first draft of the article, performed all data and statistical analyses, and created figures/ tables as appropriate. Michael D. Noseworthy, as corresponding author, provided the concept for the paper, guidance and funding. He also proofread the manuscript.

5.3 Paper

Analysis of Calf Blood Oxygen-Level Dependent (BOLD) Signal after Supine Posture

Alyaa H. Elzibak, B.Sc., M.Sc.¹, Michael D. Noseworthy, Ph.D., P.Eng.^{1,2,3,4*}

¹*Department of Medical Physics and Applied Radiation Sciences, McMaster University, Hamilton, Ontario, Canada.*

²*School of Biomedical Engineering, McMaster University, Hamilton, Ontario, Canada.*

³*Department of Electrical & Computer Engineering, McMaster University, Hamilton, Ontario, Canada.*

⁴*Department of Radiology, McMaster University, Hamilton, Ontario, Canada.*

*Corresponding Author Address:

Dr. Michael D. Noseworthy, Ph.D., P.Eng.

Associate Professor and Director of Biomedical Engineering

McMaster University, Hamilton, Ontario, Canada

Electrical and Computer Engineering

1280 Main St. West, Hamilton, Ontario, Canada. L8S 4K1

(905) 525-9140 ext.23727

Email: nosewor@mcmaster.ca

5.3.1 Abstract

Objective: To examine the response of resting blood oxygen level-dependent (BOLD) signal metrics (signal intensity, standard deviation, fractal dimension (FD) and underlying frequency components) in calf muscles to supine posture.

Materials and Methods: Images of ten healthy young adults (26.7 ± 5.1 years) were collected using a 3T MRI scanner. BOLD signal time course was evaluated in five muscle compartments (anterior and posterior tibialis, soleus, medial and lateral gastrocnemius) at three consecutive measurement times at time=0, 30 and 60 minutes of supine rest. Whole muscle cross sectional signal characteristics were compared between each time point.

Results: Mean BOLD signal intensity and standard deviation did not show significant changes with supine rest for any investigated muscle. Due to the presence of power law scaling in muscle BOLD time course, fractal analysis was performed. No statistically significant changes were observed in the FD between the three measurements for any of the muscles. No apparent trends were noted when investigating physiological peaks in the frequency spectrum of BOLD data.

Conclusion: None of the investigated BOLD characteristics were modified by supine rest. This suggests that resting calf BOLD metrics might not be

sensitive to subtle difference in muscle use between the two postural states.

Key Words: blood oxygen-level dependent (BOLD), skeletal muscle, fractal, supine rest

5.3.2 Introduction

Blood oxygen-level dependent (BOLD) imaging has been successfully applied to examine skeletal muscle microvasculature, providing insight into muscle functional status (1). The BOLD technique is attractive due to its non-invasive nature, as it employs changes in the oxygenation of the hemoglobin molecule as endogenous contrast (2). Numerous parameters contribute to the BOLD response of skeletal muscles, including changes in vascular volume, oxygen extraction, metabolism and blood flow (1-4). By perturbing muscle oxygenation status using various paradigms, investigations of muscle BOLD response are possible. To probe skeletal muscle tissue oxygenation and induce measurable BOLD signal changes, exercise challenges (5-9), ischemia induced by cuff compression (10-13) and the intake of vasoactive substances (14) have all been used. Of these stimuli, the cuff compression protocol is the only one that has been clinically applied with success to a variety of diseased populations, including peripheral arterial occlusive disease (10), systemic sclerosis (12) and granulomatosis with polyangiitis (13).

Examining the effect of the applied paradigm on the BOLD response usually involves assessment of a collected time course from a muscle region of interest (ROI). The BOLD signal in a given ROI can be evaluated by quantifying signal characteristics such as the maximal signal reached or the time

it takes the signal to peak (1, 10-13). Alternatively, examination of the underlying frequency components of the signal may reveal some insight about physiological status (4,15,16).

Recently, analysis methods employing fractal techniques have been used to quantify BOLD time series (4, 17-19). Fractals describe structures that exhibit self-similarity at different measurement scales (20). Many geometrical structures and biological systems can be represented as fractals. For example, snow flakes, the branching pattern of trees, the pulmonary system and blood vessels are all described as fractals (20). Although these are spatial fractals, many physiological time series also show temporal fractal characteristics. Some examples are heart rate (21), cerebral hemodynamics (22,23), EEG (24) and BOLD time series (17-19). Unlike Euclidean structures that have integer values as their dimensions, fractals have a fractional dimension, FD (25).

Numerous methods can be used to calculate the FD of a time series (26-29). All analyses are based on the idea that a signal, which may seem to contain random fluctuations, has an underlying complex pattern of correlations when examined at different scales. A power law scaling describes fractals, where the power spectral amplitude, $|A|$, is related to the frequency, f , according to:

$$|A|^2 \propto f^{-\phi} \tag{5.1}$$

where ϕ is a scaling exponent, referred to as the spectral index (26-28). Although the FD of a signal can be computed from the spectral index, a more accurate method has been recently established to calculate the FD (26,27). This involves classification of the signal into fractional Brownian motion (fBm) or fractional Gaussian noise (fGn). Calculation of the FD then uses relative dispersion (Disp) or bridge detrended scaled windowed variance (bdSWV) for fGn and fBm signals, respectively (26,27).

The purpose of this study was to assess resting BOLD signal characteristics (signal intensity, standard deviation, underlying frequency components and FD) of calf skeletal muscles during three measurement times. The first measurement was collected following upright posture. The second and third measurements were acquired after thirty minutes and sixty minutes of acquisition of the first measurement, respectively. Between measurements, the subjects remained in the supine posture. This was done to investigate whether any of the signal's parameters were altered with positional change. It is well known that supine posture results in modifications of structural features, including fluid volumes, muscle cross sectional area (30-34) and water diffusivity characteristics (35). The objective of this study was thus to investigate whether functional (i.e. BOLD signal characteristics) are modified by supine posture.

5.3.3 Materials and Methods

5.3.3.1 Subjects and data collection

Healthy young subjects between 23 and 33 years of age (mean = 26.7 years old, eight males and two females) were scanned using a GE 3.0T MR750 MRI system and an 8-channel phased array knee coil (GE Healthcare, Milwaukee, WI). Images of the dominant leg, as reported by each subject, were collected from the calf region with the largest cross sectional area while subjects were in the supine position. Participants were in a fasted state (refrained from food and drink intake for four hours prior to the study). None of the subjects reported a history of peripheral vascular disease or lower leg injury and none of the subjects had participated in vigorous exercise in the twenty-four hours prior to being imaged.

Following a 3-plane localizer, axial anatomical slices were acquired using a T1-weighted sequence (Fast Spin Echo (FSE), TE/TR= 14.9/707ms, FOV=16cm, 320x320 matrix, 5mm thick, 0mm gap, 20 slices). T2*-weighted BOLD slices were then collected using a GRE-EPI sequence with the following parameters: TE/TR =35/250ms, $\alpha=33^\circ$, 64x64 matrix, 2400 time points, slice thickness=10mm, 3 slices, total scan time=10.10 minutes. In addition to linear shims, second order shims were applied to optimize the field homogeneity and obtain high quality BOLD images. The first BOLD data set was acquired

after the subject had been in the scanner for twelve minutes. After this first imaging session, subjects rested inside the MR scanner. The second and third sets of BOLD data were acquired thirty-minutes and sixty minutes after the initial BOLD set, respectively. Subjects were asked to remain still during the entire imaging session.

5.3.3.2 Data analysis

All MRI BOLD data was analyzed offline using in-house programs written in Matlab (ver. 2010a, The Mathworks, Natick MA). Before analysis, images were spatially aligned using the MCFLIRT motion correction script (36) from the FMRIB Software Library, FSL (37). A single slice was chosen for each subject. This slice was the middle BOLD slice (of three). ROIs were drawn on this middle slice in five different muscle groups: the anterior and posterior tibialis, the soleus and the medial and lateral gastrocnemius. In addition, an ROI was drawn in the image noise. The average BOLD time-course was then extracted from each of the ROIs and used for further analysis. For each time course, in each muscle ROI, mean BOLD signal intensity and standard deviation were calculated. Measurement of BOLD signal temporal fractal dimension was performed using the method of Eke et al (26,27). Initially, the data from each ROI was preprocessed. This involved the application

of a parabolic window and bridge detrending. The parabolic window was given by (26):

$$P(t) = 1 - \left(\frac{2t}{N+1} - 1\right)^2 \quad \text{for } t = 1, \dots, N \quad (5.2)$$

where N is the signal's length. Finally, the power spectral amplitude was computed from the fast Fourier transform using the first 2048 volumes in the analysis. If the signal was found to be fractal (i.e. it followed a linear fit on a double logarithmic graph given by equation (5.1), the spectral index, ϕ , was computed from the slope of the best-fitted line on the double logarithmic graph of the squared amplitude against frequency, fitting only to the low frequencies ($f < 1/8$) (26). Based on the value of ϕ , the signal was classified into fBm or fGn. For fGn signals, or those whose variance did not change over time (27), ϕ was between -1 and 0.38. If ϕ was between 1.04 and 3, the signal was classified as an fBm signal, where the variance changed with time (27). Further classification, using signal summation conversion (SSC) was used for signals that did not fall in the above ranges so that they could be classified into fGn or fBm signals (26). Calculation of the FD for an fGn signal used relative dispersion (Disp), whereas that for an fBm signal was based on the bridge detrended scaled windowed variance (bdSWV) method (26,27). Both of these methods assessed the variability of the signal by examining the BOLD

time course using different measurement scales. By binning adjacent points into windows of size n that did not overlap, a measure of the variability for each window size was computed. In the case of Disp analysis, the standard deviation of the window means, σ , was related to the window size as follows (27):

$$\sigma \propto n^{H-1} \quad (5.3)$$

where H is known as the Hurst exponent and is related to FD ($FD = 2-H$). For bdSWV, the mean of the window standard deviations, $\bar{\sigma}$, was related to the window size through (27):

$$\bar{\sigma} \propto n^H \quad (5.4)$$

The slope of the double logarithmic plot of either equation 5.3 or 5.4 represented the quantity $H-1$ (for equation 5.3) and H (for equation 5.4), from which the FD was easily determined. From the 2400 BOLD time points that were acquired in this study, the first 2048 volumes were used in the analysis, after the signal had reached steady state. Computation of either bdSWV or Disp was done for nine window sizes.

Lastly, an investigation of the underlying frequency components in the BOLD time course was performed. This was done by taking the fast Fourier transform of the signal from the BOLD time course within each ROI.

5.3.3.3 Statistical analysis

For each muscle ROIs, the mean BOLD signal intensity and FD from the three imaging sessions were assessed for significance using a repeated measures analysis of variance (rmANOVA). A p-value <0.05 was considered significant. GraphPad Prism was used for all statistical testing (Version 5.0c, GraphPad Software Inc., La Jolla, CA).

5.3.4 Results

Fig. 5.1 shows a sample anatomical slice from one of the subjects, along with the corresponding BOLD slice. The results of the measurement of the mean BOLD signal intensity and standard deviation in each of the muscles, and in the image noise, for the three measurement times are shown in **Table 5.1**. BOLD signal intensity did not show significant changes with supine rest for any muscle we investigated (anterior tibialis $P=0.49$; posterior tibialis $P=0.24$; medial gastrocnemius $P=0.28$; lateral gastrocnemius $P=0.96$; soleus $P=0.59$). The ROI drawn in the BOLD image noise had a mean signal intensity of 3.8 ± 0.3 (SE) during the first measurement, 3.8 ± 0.3 during the second measurement, and 3.9 ± 0.3 during the third measurement. These values were not statistically different ($P= 0.93$). In addition, BOLD temporal standard deviation in the muscles and image noise did not show significant

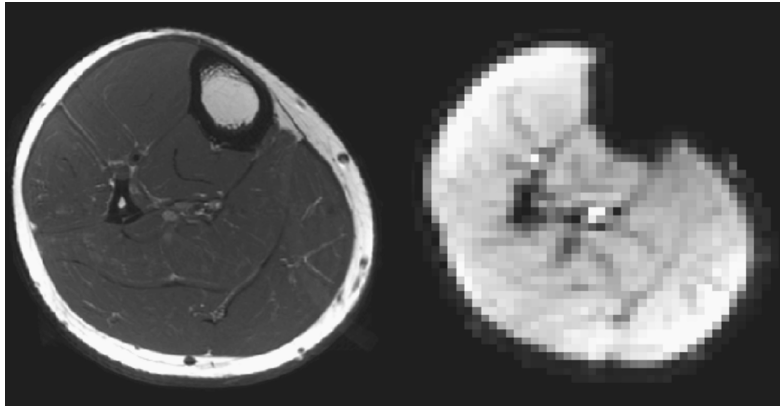


Figure 5.1: Sample T1-weighted axial anatomical slice and the corresponding T2* weighted image.

changes with supine rest ($P=0.47$ anterior tibialis, $P=0.81$ posterior tibialis, $P=0.29$ medial gastrocnemius, $P=0.07$ lateral gastrocnemius, $P=0.44$ soleus, image noise $P=0.77$).

Fractal analysis of the BOLD signal intensity revealed that the muscles' BOLD time course could be treated as fractal, due to the presence of a linear decreasing trend on the plot of the logarithm of the squared amplitude versus the logarithm of the frequency (**Fig. 5.2**). For comparison, the double logarithmic plot of a noise time course is also shown (**Fig. 5.1**). The calculated FD values in each of the muscle ROIs during the three measurement times are summarized in **Table 5.2**. No statistically significant changes were observed in the FD between the three measurements for any of the muscles (anterior tib-

ROI location	Measurement 1	Measurement 2	Measurement 3
Anterior tibialis			
SI	945.2 ± 45.2	967.0 ± 22.6	913.7 ± 38.2
SD	5.3 ± 0.6	4.4 ± 0.4	5.4 ± 0.9
Posterior tibialis			
SI	750.8 ± 19.9	755.1 ± 18.9	725.3 ± 25.1
SD	6.6 ± 0.7	6.3 ± 0.1	7.2 ± 1.1
Medial gastrocnemius			
SI	974.3 ± 68.7	1014.0 ± 63.7	1045.0 ± 56.8
SD	4.7 ± 0.9	4.4 ± 0.4	4.9 ± 0.7
Lateral gastrocnemius			
SI	944.8 ± 55.1	938.1.6 ± 68.6	937.4 ± 56.5
SD	6.0 ± 0.9	6.3 ± 0.9	7.1 ± 0.9
Soleus			
SI	794.2 ± 21.9	805.5 ± 27.5	811.6 ± 32.2
SD	6.2 ± 0.7	5.7 ± 0.5	7.6 ± 1.6
Image noise			
SI	3.8 ± 0.3	3.8 ± 0.3	3.9 ± 0.3
SD	0.6 ± 0.2	0.5 ± 0.2	0.5 ± 0.2

Table 5.1: BOLD signal was evaluated in 2400 serially acquired images (4 per second) over 10 minutes. Mean temporal BOLD signal intensity (SI, in arbitrary units) and standard deviation (SD), over the 10-minute scan are shown. The three measurements represent the data from each of the three imaging sessions, separated by 30 minutes of supine rest. Values for each measurement are mean ± SE averaged over all subjects (n=10). Statistical analysis revealed that any observed variations between imaging sessions were random or due to chance ($P > 0.05$).

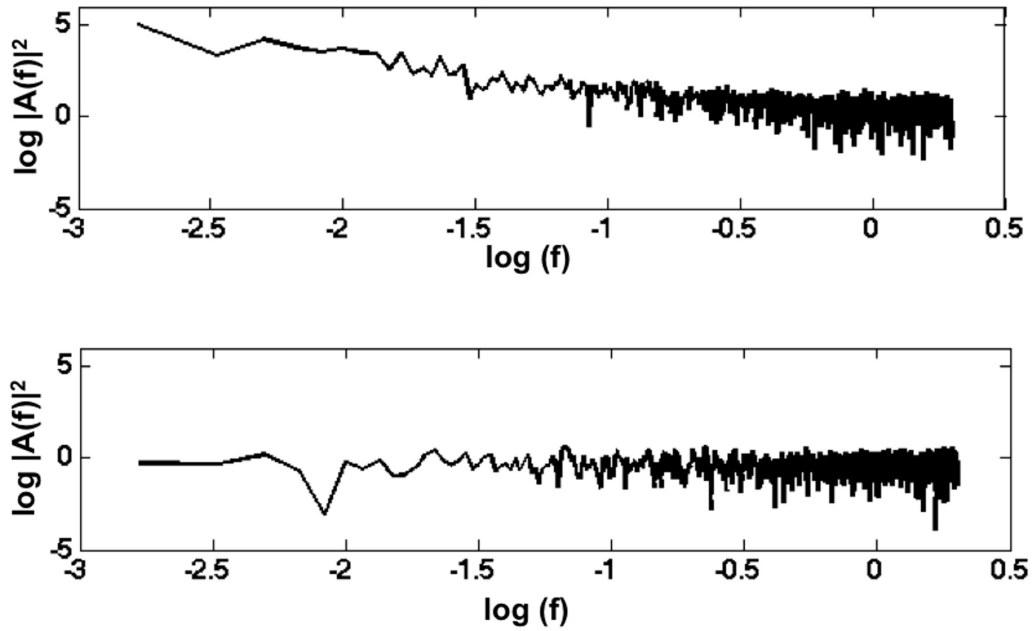


Figure 5.2: Power spectral density plots of an ROI from the medial gastrocnemius muscle (top) and one from the image noise (bottom). Power law scaling relationship was observed in the muscle ROI (top) but not in the noise ROI (bottom).

ialis $P=0.35$; posterior tibialis $P=0.23$; medial gastrocnemius $P=0.11$; lateral gastrocnemius $P=0.58$; soleus $P=0.10$).

Investigation of the frequency spectra of the BOLD time course revealed that the spectra were dominated by peaks in the low frequency range (< 0.1 Hz), with most of the power below 0.01 Hz (**Fig. 5.3**). Contributions arising from cardiac (~ 1 Hz) or respiratory (~ 0.2 Hz) rate were not evident in the spectra. Quantification of the spectra over the three measurement times

ROI location	Measurement 1	Measurement 2	Measurement 3
Anterior tibialis	1.88 ± 0.03	1.91 ± 0.01	1.86 ± 0.03
Posterior tibialis	1.91 ± 0.01	1.91 ± 0.02	1.87 ± 0.03
Medial gastrocnemius	1.88 ± 0.01	1.88 ± 0.02	1.85 ± 0.02
Lateral gastrocnemius	1.87 ± 0.03	1.87 ± 0.02	1.85 ± 0.01
Soleus	1.86 ± 0.03	1.86 ± 0.02	1.81 ± 0.03

Table 5.2: Fractal dimension of the BOLD signal in the various muscles. The three measurements represent the data from each of the three imaging sessions, separated by 30 minutes of supine rest. Values for each measurement are mean ± SE averaged over all subjects (n=10). No significant differences were observed between the three measurements for any of the muscle groups (anterior tibialis P=0.35; posterior tibialis P=0.23; medial gastrocnemius P=0.11; lateral gastrocnemius P=0.58; soleus P=0.10).

proved to be ineffective, as no consistent trend was observed either across time or among subjects (**Fig. 5.4 - Fig. 5.6**).

5.3.5 Discussion

The present study was set out to investigate whether postural change, involving movement from upright to supine position, would modify resting BOLD signal characteristics (signal intensity, standard deviation, fractal dimension (FD) and underlying frequency components). To that end, calf skeletal muscles signal metrics were assessed during an initial imaging session that followed upright posture and during two consecutive sessions, separated by thirty minutes of supine rest. Five calf regions were examined: the anterior

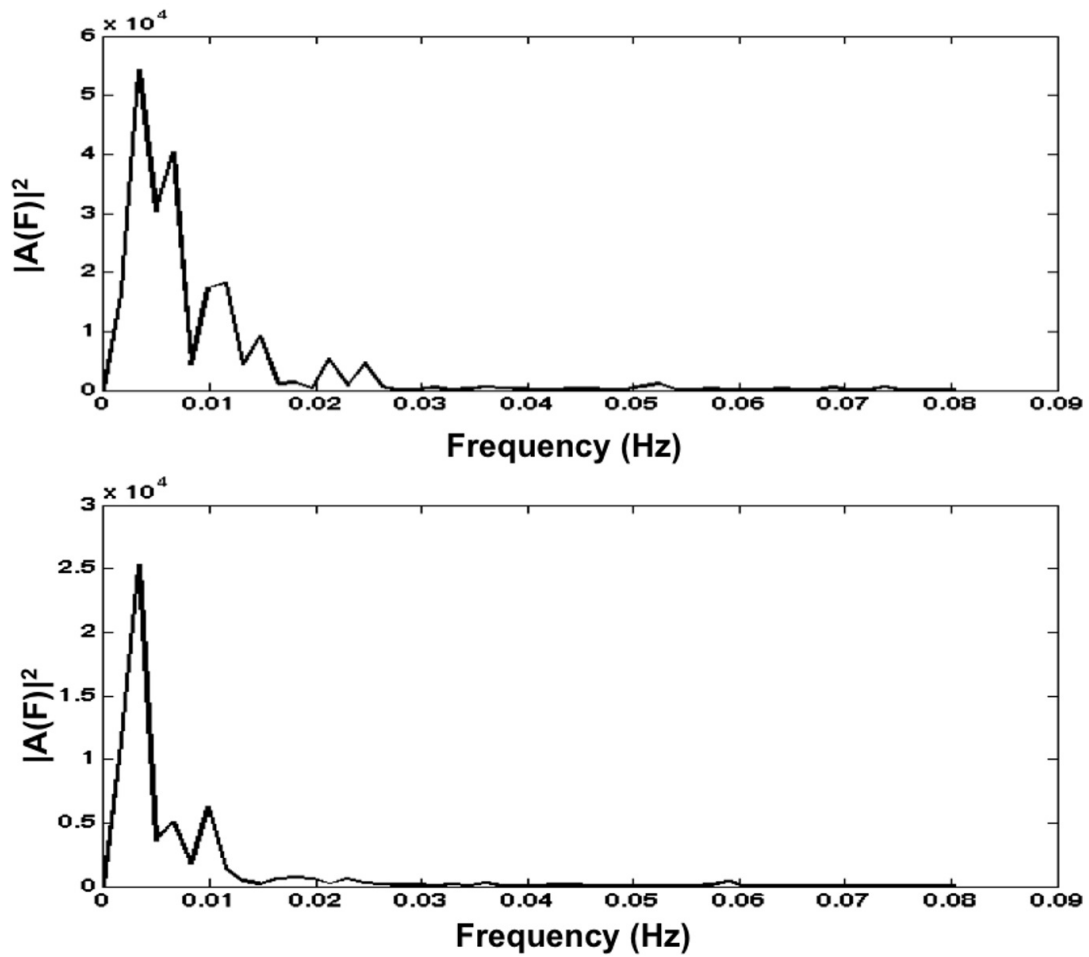


Figure 5.3: Sample spectra of the BOLD time course from the lateral gastrocnemius ROIs. Low frequency contributions (< 0.1 Hz) dominated the spectra. Similar frequency contributions were observed in spectra from all other muscles.

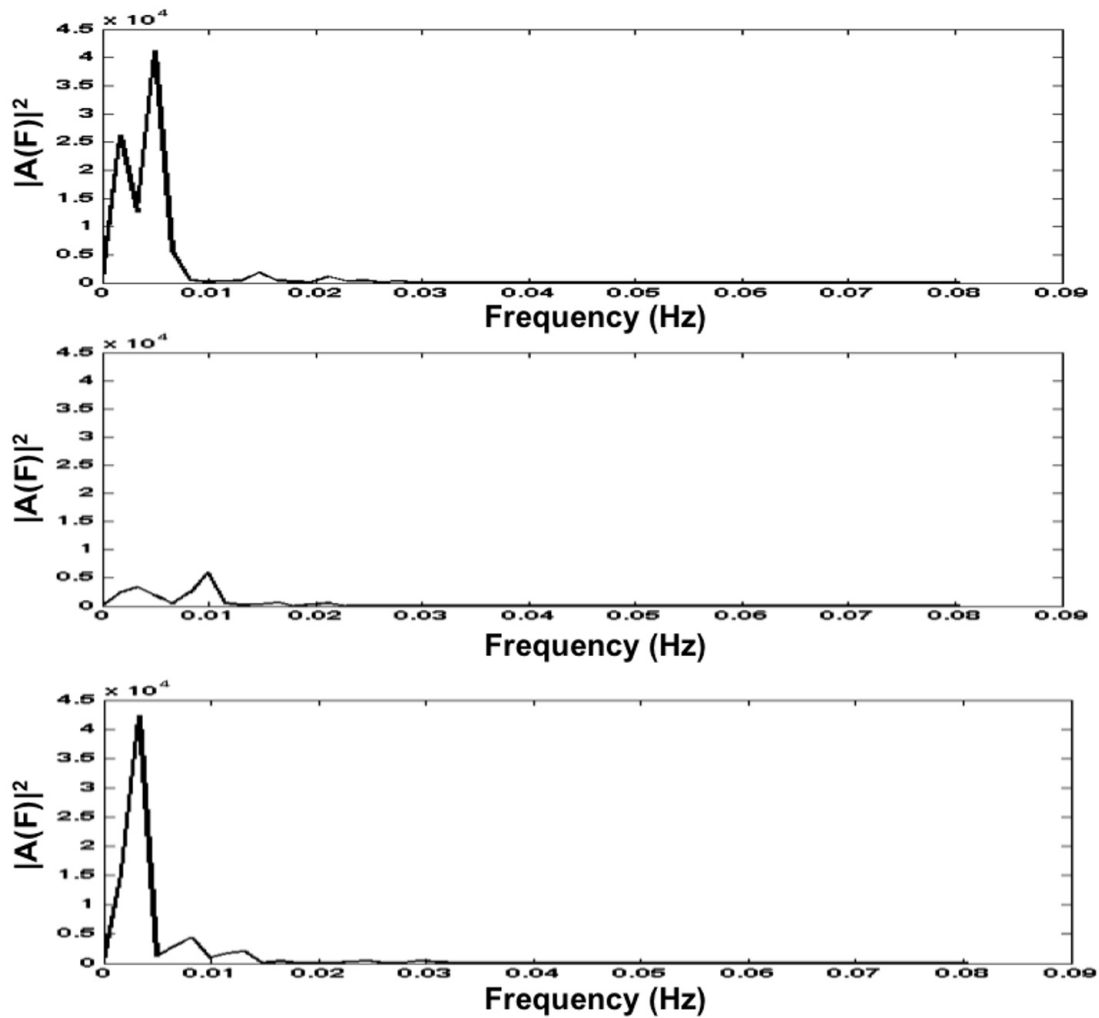


Figure 5.4: Sample spectra of the BOLD time course from the soleus muscle of one of the subjects during the first (top), second (middle) and third (last) imaging sessions. No trend was observed when comparing spectra of various subjects (see **Fig. 5.5** and **Fig. 5.6**).

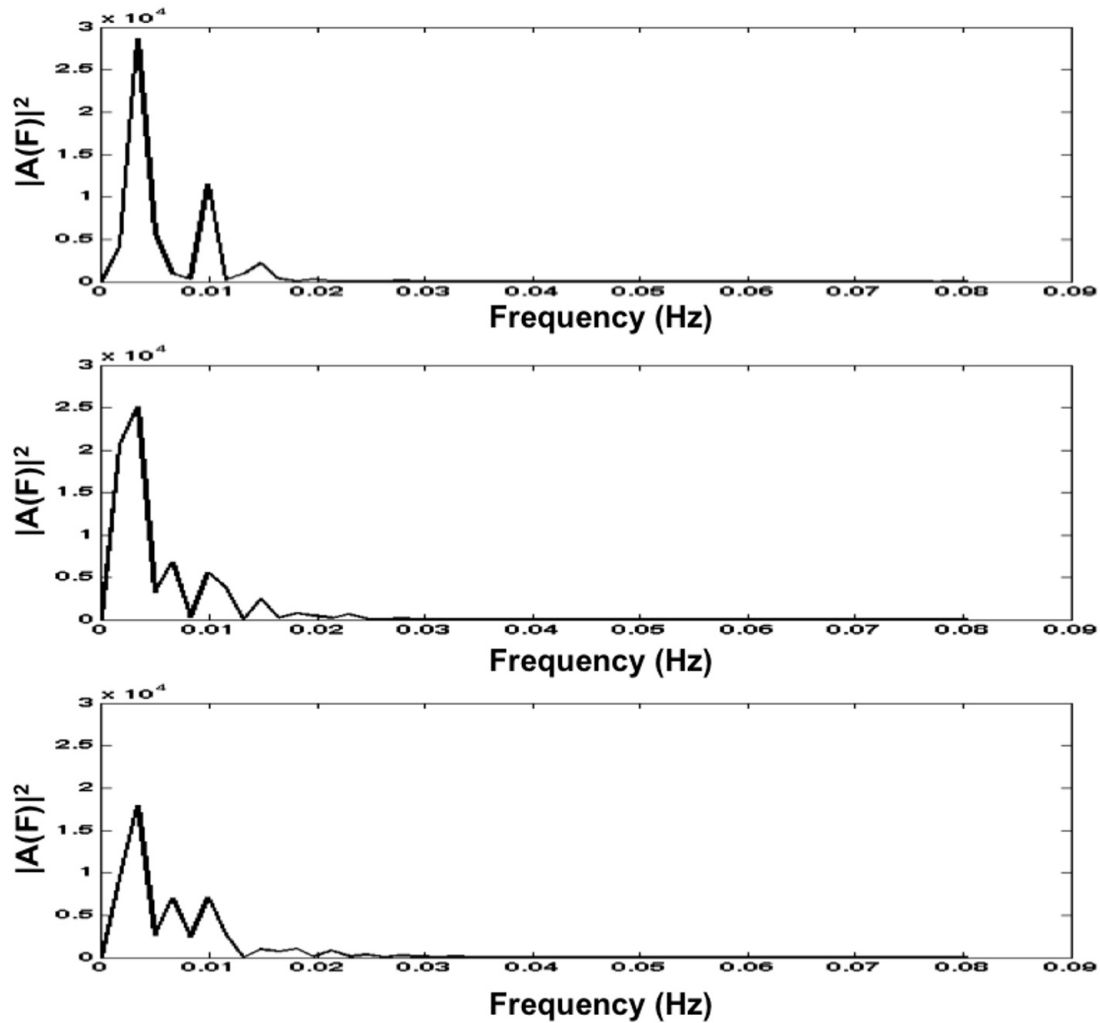


Figure 5.5: Sample spectra of the BOLD time course from the soleus muscle of one of the subjects during the first (top), second (middle) and third (last) imaging sessions. No trend was observed when comparing spectra of various subjects (see **Fig. 5.4** and **Fig. 5.6**).

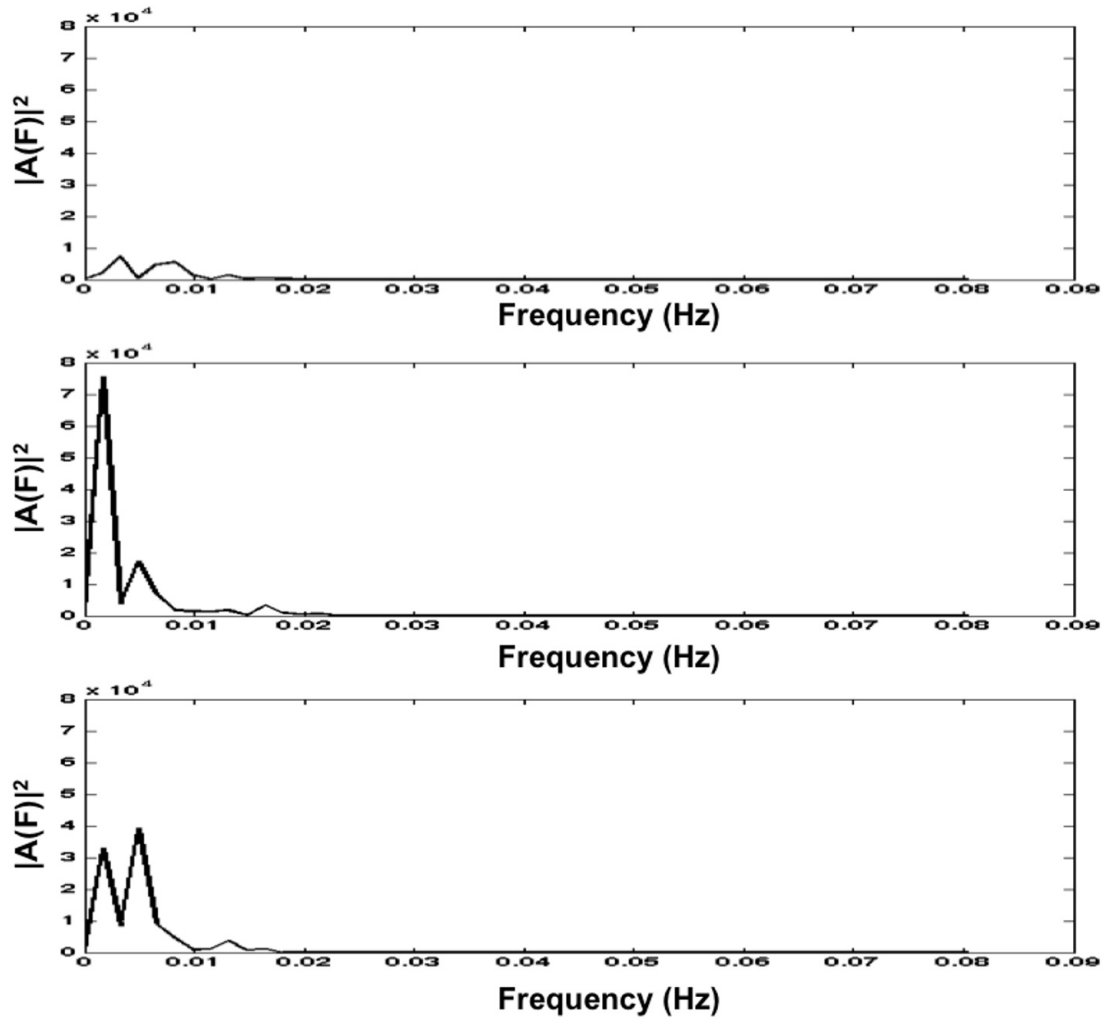


Figure 5.6: Sample spectra of the BOLD time course from the soleus muscle of one of the subjects during the first (top), second (middle) and third (last) imaging sessions. No trend was observed when comparing spectra of various subjects (see **Fig. 5.4** and **Fig. 5.5**).

and posterior tibialis, the soleus, and the medial and lateral gastrocnemius. We hypothesized that the computed signal characteristics would differ between the three measurement sessions. The reason for this speculation was that position-related changes have been well documented in literature (30-35, 38-42). Fluid shifts have been reported to accompany postural changes (32-34). In addition, changes in plasma volume (31), leg volume (30) and muscle cross sectional area (33,34) have been established following postural manipulation from standing to supine position. A few literature studies have also examined changes in heart rate, oxygen consumption, muscle performance and leg blood flow in response to position related changes (38-42). Since the BOLD signal represents contributions from vascular volume, blood flow and tissue oxygenation (1-4) and because postural manipulations have been reported to alter some of these quantities, it was not unreasonable to investigate the effect of position changes on BOLD characteristics.

The mean and standard deviation of the BOLD signal intensity were the first metrics that were assessed, to obtain an idea of the global signal characteristics. We failed to report any changes in mean BOLD signal intensity or standard deviation with supine rest (**Table 5.1**). We expected image noise to remain consistent throughout imaging sessions, as subjects were not moved for the duration of the entire experiment. As for mean BOLD signal

intensity, with the source of BOLD signal change being microvascular (i.e. blood volume, blood flow and oxy:deoxyhaemoglobin ratio), we speculated that baseline BOLD signal would be maximally changing as leg muscles would have just switched from standing to supine posture. As our study showed lack of change in BOLD signal intensity and its variability with supine rest, it is suggested that global measures of resting BOLD signal measurement may not be sensitive to the subtle difference in muscle use between the two postural states.

Since calculation of signal temporal fractal dimension has been shown to be sensitive to subtle fluctuations (4), we postulated that it could be useful in determining if posture affects resting muscle BOLD signals. Fractals have been used to describe many geometrical structures and physiological dynamics (17-29). Fractals exhibit self-similarity. For a spatial fractal, this means that sub units of the structure resemble the overall structure, as is seen in the branching of trees. For temporal fractals, the pattern of fluctuations in the signal is similar over various time scales. A power law scaling characterizes fractal systems, as shown in Equation (5.1).

Fractal analysis has been applied to investigate the fluctuations seen in many physiological time series, including heart beat recordings (21,25,43), EEG recordings (24) and cerebral artery flow velocity and blood pressure (22).

Fractals have also been recently used to quantify BOLD signal fluctuations in time series collected from the brain (18,19,44), tumors (17), and skeletal muscle (4). Spatial fractals have been used to characterize blood flow distributions within skeletal muscles (45,46). Fractal analysis has also provided information of diagnostic and prognostic value, especially when it comes to cardiovascular dynamics. Losses of fractal scaling or alterations in the power law relationship have been noted in some diseases (16,21,22) and with aging (21,42).

Our muscle BOLD time series, when investigated for fractal characteristics, revealed a power law scaling (**Fig. 5.2**). According to the calculated spectral index, ϕ , and using signal summation conversion when necessary (26,27), muscle BOLD time series were classified as fBm. Signal class of many physiological time courses has been reported to be fBm (20, 22, 27), although brain BOLD signals fall in the fGn class (18,19). The FD of the investigated muscles was around 1.87 (**Table 5.2**). FD values close to 1.0 represent smooth signals, whose elements are positively correlated (20,26). On the other hand, values close to 2.0 represent signals that exhibit negative correlation or "roughness" (20,26). We did not find any significant changes in the FD between the three measurement times in any of the muscles (**Table 5.2**).

Spectral analysis is a useful way of examining time series and has been employed by numerous groups to gain insight into the dynamics of many phys-

iological signals (4, 15, 16, 47, 48). Once distinct peaks have been identified in a power spectrum, quantification of the power at a given frequency is possible. Alterations in the characteristics of a power spectrum have been noted to reflect disease states (4, 15, 16). When analyzing the BOLD time course by looking at the spectral distribution in this study ((**Fig. 5.3 - Fig. 5.6**)), we noted that low frequency peaks (below 0.1 Hz) were the major contributors to the spectrum, with most of the fluctuations at frequencies lower than 0.01 Hz. From a physiological perspective, low frequency components in the range of 1-15 cycles/ minute (0.017-0.25 Hz) have been attributed to vasomotion, based on observations from blood flow measurements (15). Frequencies below this range (<1-2 cycles /minute) have also been observed in blood flow data and were postulated to result from a combination of vasoactivity as well as hemodynamic mechanisms (15). The low frequency peaks observed in BOLD spectra in this study could reflect these phenomena. Our spectra revealed variable response when comparing between muscles and subjects. It was difficult to identify an apparent trend or to pinpoint which of the frequencies were of physiological origin or which ones reflected low frequency noise. Thus, conclusions about changes in power spectrum between the three measurement times were not possible to make.

No studies exist in literature describing muscle oxygenation changes due to postural change. However, two studies have investigated leg blood flow in standing and supine posture (39, 40). In one study, leg blood flow did not differ between supine and standing postures at rest (40), while another study found significantly higher blood flow to the leg during upright exercise, in comparison to supine exercise (39). In addition, one study has examined vastus lateralis muscle deoxygenation during upright and supine cycling exercise (41). Higher muscle deoxygenation was observed in supine cycling, compared to upright cycling (41). Vascular filling (achieved by dangling the leg) and vascular draining have also been reported to impact BOLD signal contrast in calf muscles during reactive hyperemia induced by cuff compression (49). Numerous parameters contribute to BOLD signal fluctuations, including vascular volume and tissue oxygenation. Although BOLD signal measurement does not necessarily reflect fluid shifts between compartments, since some studies have reported blood flow and deoxygenation changes in skeletal muscles due to positional changes, we were interested in assessing the effects of body posture on resting BOLD signal characteristics. Muscle BOLD signal is best studied following a paradigm that perturbs tissue oxygenation (such as exercise or cuff compression), however, recent interest has been shown in muscle assessment in the resting state as it is more tolerable by patients who may show physical

weakness (50). Since we did not find changes in any of the investigated resting BOLD signal characteristics, our results suggest that resting BOLD signal is not sensitive to subtle differences in muscle use between the two postural positions. If a paradigm (such as an exercise protocol) had been performed in the standing and supine position, BOLD signal characteristics would have probably been observed to differ between the two postures.

Our study has a few limitations. The response of BOLD signal characteristics was only assessed in healthy young subjects. Further studies are needed to investigate signal characteristics in subjects of varying age or those with various pathologies. In addition, more postural manipulations (standing to supine, supine to standing, seated to supine, ...) may help in assessing whether the resting BOLD signal is affected by position related changes. Finally, partial voluming may be an issue masking any subtle changes that could be occurring. Future work should perform mapping of FD to validate whether muscle segments behave in the same way whole muscles do.

In conclusion, resting BOLD signal characteristics did not show changes in response to postural change from upright to supine position in healthy young adult subjects. These results imply that resting calf BOLD metrics might not be sensitive to the subtle difference in muscle use between the two postural states. Extension of the results of the current study to BOLD experimental design in-

volving other situations, such as exercise or cuff compression, is not warranted without an assessment of postural manipulations on BOLD characteristics in such designs.

5.3.6 References

- (1) Partovi S, Karimi S, Jacobi B, Schulte AC, Aschwanden M, Zipp L, Lyo JK, Karmonik C, Müller-Eschner M, Huegli RW, Bongartz G, Bilecen D. Clinical implications of skeletal muscle blood-oxygenation-level-dependent (bold) mri. *Magn Reson Mater Phy* 2012; 25: 251-261
- (2) Noseworthy MD, Bulte DP, Alfonsi J. BOLD magnetic resonance imaging of skeletal muscle. *Semin Musculoskelet Radiol* 2003;7:307-315
- (3) Jacobi B, Bongartz G, Partovi S, Schulte AC, Aschwanden M, Lumsden AB, Davies MG, Loebe M, Noon GP, Karimi S, Lyo JK, Staub D, Huegli RW, Bilecen D. Skeletal muscle BOLD MRI: from underlying physiological concepts to its usefulness in clinical conditions. *JMRI* 2012;35:1253-1265
- (4) Noseworthy MD, Davis AD, Elzibak AH. Advanced MR imaging techniques for skeletal muscle evaluation. *Semin Musculoskelet Radiol* 2010;14:257-268
- (5) Damon BM, Wadington MC, Hornberger JL, Lansdown DA. Absolute and relative contributions of BOLD effects to the muscle functional MRI signal in-

tensity time course: effect of exercise intensity. *Magn Reson Med* 2007;58:335-345

(6) Wigmore DM, Damon BM, Poher DM, Kent-Braun JA. MRI measures of perfusion related changes in human skeletal muscle during progressive contractions. *J Appl Physiol* 2004;97:2385-2394

(7) Jordan BF, Kimpalou JZ, Beghein N, Dessy C, Feron O, Gallez B. Contribution of oxygenation to BOLD contrast in exercising muscle. *Magn Reson Med* 2004;52:391-396

(8) Meyer RA, Towse TF, Reid RW, Jayaraman RC, Wiseman RW, McCully KK. BOLD MRI mapping of transient hyperemia in skeletal muscle after single contractions. *NMR Biomed* 2004; 17:392-398

(9) Towse TF, Slade JM, Ambrose JA, DeLano MC, Meyer RA. Quantitative analysis of the postcontractile blood-oxygenation-level-dependent (BOLD) effect in skeletal muscle. *J Appl Physiol*; 2011;111:27-39

(10) Ledermann HP, Schulte AC, Heidecker HG, Aschwanden M, Jäger KA, Scheffler K, Steinbrich W, Bilecen D. Blood oxygenation level-dependent magnetic resonance imaging of the skeletal muscle in patients with peripheral arterial occlusive disease. *Circulation* 2006;113:2929-2935

(11) Schulte AC, Aschwanden M, Bilecen D. Calf muscles at blood oxygen level-dependent MR imaging: aging effects at postocclusive reactive hyperemia. *Radiology* 2008;247:482-489

(12) Partovi, S., Schulte AC, Aschwanden M, Staub D, Benz D, Imfeld S, Jacobi B, Broz P, Jager KA, Takes M, Huegli RW, Bilecen D, Walker UA. Impaired skeletal muscle microcirculation in systemic sclerosis. *Arthritis Res Ther* 2012; 14 (5), R209

(13) Jacobi B, Schulte AC, Partovi S, Michel S, Karimi S, Lyo JK, Daikeler T, Aschwanden M, Staub D, Zipp L, Rasmus M, Huegli RW, Bongartz G, Bilecen D. Alterations of skeletal muscle microcirculation detected by blood oxygenation level-dependent mri in a patient with granulomatosis with polyangiitis. *Rheumatology* 2013;52 (3), 579-81

(14) Bulte DP, Alfonsi J, Bells S, Noseworthy MD. Vasomodulation of skeletal muscle BOLD signal. *J Magn Reson Imaging* 2006;24, 886-890

(15) Braun RD, Lanzen JL, Dewhirst MW. Fourier analysis of fluctuations of oxygen tension and blood flow in R3230Ac tumors and muscle in rats. *Am J Physiol* 1999; 277, H551-68

(16) Seeley AJE, Macklem PT. Complex systems and the technology of variability analysis. *Crit Care* 2004;8, R367-84

(17) Wardlaw, Wong GR, Noseworthy MD. Identification of intratumour low frequency microvascular components via bold signal fractal dimension mapping. *Phys Med* 2008;24, 87-91

(18) Maxim V, Sendur L, Fadili J, Suckling J, Gould R, Howard R, Bullmore E. Fractional gaussian noise, functional mri and alzheimer's disease. *NeuroImage* 2005; 25, 141-158

(19) Warsi MA, Molloy W, Noseworthy MD. Correlating brain blood oxygenation level dependent (bold) fractal dimension mapping with magnetic resonance spectroscopy (mrs) in alzheimer's disease. *MAGMA* 2012; 25, 335-344

(20) Bassingthwaighe JB, Liebovitch LS, West BJ. *Fractal physiology*. 1994 Oxford University Press, Inc

(21) Goldberger AL, Amaral LAN, Hausdorff JM, Ivanov PC, Peng C-K, Stanley HE. Fractal dynamics in physiology: alterations with disease and aging. *Proc Natl Acad Sci* 2002; Suppl 1,2466-72

(22) Soehle M, Czosnyka M, Chatfield DA, Hoeft A, Peña A. Variability and fractal analysis of middle cerebral artery blood flow velocity and arterial blood pressure in subarachnoid hemorrhage. *J Cereb Blood Flow Metab* 2008;28,64-

73

(23) Fahmeed H (ed.), Dynamic Brain Imaging: Multi-Modal Methods and In Vivo Applications. Humana Press 2009; 489: 23-40

(24) Paramanathan P, Uthayakumar R. Application of fractal theory in analysis of human electroencephalographic signals. Comput Biol Med 2008;38, 372-8

(25) Goldberger AL, West BJ. Fractals in physiology and medicine. Yale J Biol Med 1987;60, 421-435

(26) Eke A, Hermán P, Bassingthwaite JB, Raymond GM, Percival DB, Cannon M, Balla I, Ikrényi C. Physiological time series: distinguishing fractal noises from motions. Eur J Physiol 2000;439,403-415

(27) Eke A, Hermán P, Kocsis L, Kozak LR. Fractal characterization of complexity in temporal physiological signals. Physiol Meas 2002;23, R1-38

(28) Eke A, Hermán P, Sanganahalli BG, Hyder F, Mukli P, Nagy Z. Pitfalls in fractal time series analysis: fmri bold as an exemplary case. Front Physiol 2012; 3, 417

(29) Schepers HE, van Beek JHGM, Bassingthwaite JB. Four methods to estimate the fractal dimension from self-affine signals. IEEE Eng Med Biol Mag 1992;11, 57-64

(30) Waterfield RL. The effect of posture on the volume of the leg. *J Physiol* 1931; 72,121-123

(31) Thompson WO, Thompson PK, Dailey ME (1928) The effect of posture upon the composition and volume of the blood in man. *J Clin Invest* 5: 573-604

(32) Maw GJ, Mackenzie IL, Taylor NAS. Redistribution of body fluids during postural manipulations. *Acta Physiol Scand* 1995; 155,157-163

(33) Berg HE, Tender B, Tesch PA. Changes in lower limb muscle cross-sectional area and tissue fluid volume after transition from standing to supine. *Acta Physiol Scand* 1993;148,379-385

(34) Conley MS, Foley JM, Ploutz-snyder LL, Meyer RA, Dudley GA. Effect of acute head-down tilt on skeletal muscle cross-sectional area and proton transverse relaxation time. *J Appl Physiol* 1996; 81:1572-1577

(35) Elzibak AH, Noseworthy MD. Assessment of diffusion tensor imaging indices in calf muscles following postural change from standing to supine position. *Magn Reson Mater Phy* (In Press).

(36) Jenkinson M, Bannister P, Brady JM, Smith SM. Improved optimisation for the robust and accurate linear registration and motion correction of brain images. *Neuroimage* 2002;17:825-841

(37) Jenkinson M, Beckmann CF, Behrens TE, Woolrich MW, Smith SM. FSL. Neuroimage 2012;62:782-90

(38) Jones AY, Dean E. Body position change and its effect on hemodynamic and metabolic status. Heart Lung 2004;33:281-290

(39) Egaña M, Green S. Effect of body tilt on calf muscle performance and blood flow in humans. J Appl Physiol 2005;57:2249-2258

(40) MacDonald MJ, Shoemaker JK, Tschakovsky ME, Hughson RL. Alveolar oxygen uptake and femoral artery blood flow dynamics in upright and supine leg exercise in humans. J Appl Physiol 1998;85:1622-1628

(41) Denis R, Perrey S. Influence of posture on pulmonary O₂ uptake kinetics, muscle deoxygenation and myoelectrical activity during heavy-intensity exercise. Journal of Sports Science and Medicine 2006;5:254-265

(42) Leyk D, Essfeld D, Baum K, Stegemann J. Early leg blood flow adjustment during dynamic foot plantarflexions in upright and supine body position. Int. J. Sports Med. 1994;15:447-452

(43) Iyengar N, Peng CK, Morin R, Goldberger AL, Lipsitz LA. Age-related alterations in the fractal scaling of cardiac interbeat interval dynamics. Am J Physiol 1996;271:R1078-R1084

(44) Wink A-M, Bullmore E, Barnes A, Bernard F, Suckling J. Monofractal and multifractal dynamics of low frequency endogenous brain oscillations in functional MRI. *Hum Brain Mapp* 2008;29:791-801

(45) Iversen PO, Nicolaysen G. High correlation of fractals for regional blood flows among resting and exercising skeletal muscles. *Am J Physiol Heart Circ Physiol* 1995;269:H7-H13

(46) Kalliokoski KK, Kuuesla TA, Laaksonen MS, Knuuti J, Nuutila P. Muscle fractal vascular branching pattern and microvascular perfusion heterogeneity in endurance-trained and untrained men. *J Physiol* 2003;546.2:529-535

(47) Akselrod S, Gordon D, Ubel FA, Shannon DC, Berger AC, Cohen RJ. Power spectrum analysis of heart rate fluctuation: a quantitative probe of beat-to-beat cardiovascular control. *Science* 1981;213:220-222

(48) Pomeranz B, Macaulay RJB, Caudill MA, Kutz I, Adam D, Gordon D, Kilborn KM, Barger AC, Shannon DC, Cohen RJ, Benson H. Assessment of autonomic function in humans by heart rate spectral analysis. *Am J Physiol* 1985;248:H151-H153

(49) Duteil S, Wary C, Raynaud JS, Lebon V, Lesage D, Leroy-Willig A, Carlier PG. Influence of vascular filling and perfusion on BOLD contrast during

reactive hyperemia in human skeletal muscle. *Magn Reson Med* 2006;55:450-454

(50) Zuo CS, Sung Y-H, Simonson DC, Habecker E, Wang J, Haws C, Vil-lafuerte RA, Henry ME, Dobbins RL, Hodge RJ, Nunez DJR, Renshaw PF. Reduced t_2^* values in soleus muscle of patients with type 2 diabetes mellitus. *PLoS ONE* 2012;7: e49337

Chapter 6

Diffusion tensor imaging of the normal foot at 3T

Alyaa H. Elzibak, M.Sc., Dinesh A. Kumbhare, MSc, MD, FRCPC, Srinivasan Harish, MBBS, FRCPC, Michael D. Noseworthy, Ph.D., P.Eng.

6.1 Context of the Paper

Diffusion tensor imaging (DTI) has been used to examine numerous skeletal muscles of the body. In the lower limb, which is the region of interest of this project, diffusion imaging has been only applied to examine thigh (Budzik et al., 2007; Qi et al., 2008; Kan et al., 2009; Gondin et al., 2010; Cermak et al., 2012) and calf (Sinha and Yao, 2002; Galbán et al., 2004; Zaraiskaya et al., 2006; Galbán et al., 2005, 2007; Heemskerk et al., 2010; Sinha and Sinha, 2011) muscles. This manuscript aimed at extending the technique to the foot region, by assessing the feasibility of diffusion imaging of foot muscles and establishing baseline DT metrics in healthy subjects.

6.2 Declaration Statement

Alyaa H. Elzibak, as principle author, wrote the first draft of the article, performed all data and statistical analyses, and created figures/tables as appropriate. Dinesh A. Kumbhare provided the concept for the paper. Michael D. Noseworthy, as corresponding author, provided guidance and funding. All co-authors proofread and edited the manuscript. Michael D. Noseworthy completed the online submission process of the paper.

This paper has been accepted for publication on November 5, 2013 in the *Journal of Computed Assisted Tomography (JCAT)*. Permission to include this work was granted from Wolters Kluwer Lippincott Williams & Wilkins. This is a non-final version of the article, published in final form in *Journal of Computed Assisted Tomography (JCAT)*.

<http://journals.lww.com/jcat/Pages/default.aspx>.

6.3 Paper

Diffusion tensor imaging of the normal foot at 3T

Alyaa H. Elzibak, M.Sc.^{1,2}, Dinesh A. Kumbhare, MSc, MD, FRCPC^{3,4}, Srinivasan Harish, MBBS, FRCPC^{2,5,6}, Michael D. Noseworthy, Ph.D.,

P.Eng.^{1,2,3,5,6,7*}

¹*Department of Medical Physics and Applied Radiation Sciences, McMaster University, Hamilton, Ontario, Canada.*

²*Imaging Research Centre, St. Joseph's Healthcare, Hamilton, ON, Canada.*

³*School of Biomedical Engineering, McMaster University, Hamilton, Ontario, Canada.*

⁴*Department of Medicine, Division of Rehabilitation Sciences, McMaster University, Hamilton, Ontario, Canada.*

⁵*Department of Radiology, McMaster University, Hamilton, Ontario, Canada.*

⁶*Department of Diagnostic Imaging, St. Joseph's Healthcare, Hamilton, ON, Canada.*

⁷*Department of Electrical & Computer Engineering, McMaster University, Hamilton, Ontario, Canada.*

***Corresponding Author Address:**

Dr. Michael D. Noseworthy, Ph.D., P.Eng.

Associate Professor and Director of Biomedical Engineering

McMaster University, Hamilton, Ontario, Canada

Electrical and Computer Engineering

1280 Main St. West, Hamilton, Ontario, Canada. L8S 4K1

(905) 525-9140 ext. 23727

Email: nosewor@mcmaster.ca

Dr. Michael Noseworthy wishes to acknowledge he has received lecture honoraria from both GE Healthcare and Bayer Healthcare in the last 12 months. Neither of these were connected to the work presented in this manuscript.

Acknowledgments: The authors would like to thank Norm Konyer for helpful discussions and Andrew Davis for writing the BASH script. Funding from Natural Sciences and Engineering Research Council (NSERC) of Canada is also acknowledged (doctoral NSERC postgraduate scholarship to AHE).

6.3.1 Abstract

Objective: To establish normative diffusion tensor imaging (DTI) eigenvalues ($\lambda_1, \lambda_2, \lambda_3$), apparent diffusion coefficient (ADC) and fractional anisotropy (FA) in asymptomatic foot muscles.

Methods: Ten healthy adults (25.9 ± 4.3 years) were examined using a 3T MRI scanner. DTI indices were evaluated in five muscles in the foot: quadratus plantae (QP), abductor hallucis (AH), flexor hallucis brevis (FHB), flexor digitorum brevis (FDB), and abductor digiti mini (ADM). Signal-to-noise ratio (SNR) was also measured for each muscle.

Results: In the various foot muscles, λ_1 ranged from 1.88×10^{-3} - 2.14×10^{-3} mm²/s, λ_2 from 1.39×10^{-3} - 1.48×10^{-3} mm²/s, λ_3 from 0.91×10^{-3} - 1.27×10^{-3} mm²/s, ADC from 1.48×10^{-3} - 1.55×10^{-3} mm²/s and FA from 0.21-0.40. Statistical differences were seen in some eigenvalues between muscle pairs. Mean SNR ranged from 47.5-69.1 in the various muscles examined.

Conclusions: Assessment of anisotropy of water diffusion in foot muscles was feasible using DTI. The measured DTI metrics in the foot were similar to those in calf and thigh skeletal muscles.

Key Words: magnetic resonance imaging (MRI), diffusion tensor imaging (DTI), skeletal muscle, normal foot, 3T

6.3.2 Introduction

Diffusion tensor imaging (DTI) has become a widely applied technique to characterize the microstructure of anisotropic tissues. The method has been used to noninvasively study various organs, such as the brain (1-3), liver (4), kidney (5,6), heart (7), breast (8), prostate (9) and skeletal muscle (10-13). Diffusion imaging measures the random displacement (Brownian motion) of water molecules, which is isotropic in an unconstrained environment. However, in coherently oriented structures such as muscle fibers, molecular diffusion is hindered by barriers that constrain the free diffusion. This results in anisotropic diffusion, where water molecules move more easily along the axis of the myofibril than perpendicular to it.

Diffusivity of water can be characterized using numerous metrics, including three eigenvalues (λ_1 , λ_2 , λ_3), where λ_1 corresponds to diffusion along the principle axis. The average of the eigenvalues is represented by the apparent diffusion coefficient (ADC) or the mean diffusivity (MD). Fractional anisotropy (FA) characterizes the shape of the diffusion ellipsoid and ranges between zero for perfect isotropic diffusion and one for anisotropic diffusion, as in an infinite cylinder. In skeletal muscle, an interpretation of the meaning of DTI eigenvalues has been inconclusive. It is generally accepted that λ_1 represents diffusion along the muscle fiber axis. Galban et al. suggested that λ_2

and λ_3 might represent diffusion along sheets of fibers and within muscle fiber cross-section, respectively (14).

Since its initial application to examine skeletal muscle in vitro by Basser et al. (15), DTI has become a useful tool to probe muscle microstructure in vivo to gain insight about the underlying architecture (16). The technique has been applied to evaluate muscle health and has shown that injured calf muscles are associated with increased eigenvalues and ADC, with a reduction in FA (17). Tracking of muscle fibers in damaged zones further revealed structural abnormalities with injury (17). Diffusion imaging has also been used to evaluate pathological muscle conditions (18,19) and muscle disruptions induced by exercise (20). Some DTI studies have demonstrated dependence of diffusivity measures on age (21,22) and gender (23), while others failed to establish such correlations (13,24). DTI metrics have also been shown to depend on muscle fiber architecture and pennation angle (25-27). Changes in diffusion indices have been reported following exercise (28-30), due to ischemic damage (31), and in response to external pressure application (32).

Skeletal muscle DTI studies now span a range of muscles located throughout the body, including the thigh (10,18,20), lumbar (13), forearm (11) and calf (12,14,17,21-34) musculature. However, numerous pathologies are known to affect foot tissue, such as peripheral vascular diseases and complex regional pain

syndrome (35,36). These contribute to muscle weakness, disuse and atrophy, and in severe cases, could lead to amputation of the affected limb. Although conventional anatomical imaging may aid in diagnosing muscle impairments, an understanding of muscle dysfunction usually requires biopsies or the use of functional imaging methods. The imaging approach is more tolerable by patient populations as biopsies are invasive, painful, and associated with complications. In addition, biopsy of foot muscles is not routine clinical practice. The importance of examining foot muscles using advanced functional imaging methods has recently been elucidated by Kos et al. (37). The researchers explored the use of foot blood oxygen level-dependent (BOLD) MR imaging. Using an ischemia-hyperemia paradigm that is widely applied to calf studies, the group demonstrated the feasibility of foot imaging in healthy volunteers (37).

We believe that advanced imaging protocols such as functional imaging and DTI could provide valuable clinically relevant information in the evaluation of pathological conditions that manifest with symptoms in the foot. The purpose of this study was to examine the diffusive properties of foot muscles and establish a normative range of values in healthy subjects. To our knowledge, DTI indices (eigenvalues, FA and ADC) have not been previously investigated in the foot. Assessment of diffusion behavior in an asymptomatic

population is necessary before future application of the technique to a diseased group of subjects.

6.3.3 Materials and Methods

6.3.3.1 Subjects

Ten healthy adult subjects between 19 and 32 years of age (mean \pm SD: 25.9 ± 4.3 years, height: 173.9 ± 10.2 cm, weight: 69.9 ± 12.6 kg, 2 females) took part in the study. The foot muscles of the subject's dominant leg were imaged. None of the subjects reported having any pathology in the imaged foot. Participants refrained from food and drink intake for at least four hours prior to the study and none of the subjects performed strenuous exercises in the twenty-four hours preceding the imaging session. These measures were imposed in an attempt to standardize our DTI metrics. Some DTI studies require subjects to fast and refrain from intense exercise, while others do not report any pre-measurement restrictions. All subjects underwent MR screening before taking part in the study, which was approved by our local research ethics board.

6.3.3.2 Magnetic resonance imaging

MR imaging was performed using a GE Signa MR750 3.0T MRI system and an HD foot/ankle array coil (GE Healthcare, Milwaukee, WI). Subjects

were placed feet-first and lay in the supine position in the MR scanner. Following scout imaging, high contrast T1-weighted coronal (short axis) anatomical images were collected using a Fast Spin Echo (FSE) sequence with the following parameters: TE/TR= 14.9/785 ms, 5mm slice thickness, 0mm gap, FOV=16cm, 320x320 matrix, 20 slices, Echo Train Length (ETL) of 4. Images were acquired starting at the neck of the talus and moving towards the distal end of the foot. DTI images were subsequently collected from the same anatomical location as the T1-weighted images. A dual spin-echo EPI sequence was used for DTI measurements with 15 diffusion encoding gradient directions ([1,0,0]; [0.643,0.766,0]; [0.258,0.307,0.916]; [0.258,0.307,0.916]; [0.164,-0.507,0.846]; [-0.796,-0.321,0.513]; [0.761,0.427,0.489]; [-0.506,0.833,0.224]; [0.667, -0.158,0.728]; [0.128,0.959,0.254]; [-0.178,-0.898,-0.403]; [0.255,-0.590,-0.767]; [0.340,-0.736,0.585]; [-0.801,0.329,0.501];[0.336,0.043,-0.941]), one $b=0$ s/mm^2 image, TE/TR= 68.8/4050ms, b -value=400 s/mm^2 , 5mm slice thickness, 0mm gap, FOV=16cm, frequency encoding along the superior/ inferior direction, 64x64 matrix, 20 slices and array spatial sensitivity encoding technique (ASSET) acceleration factor of 2. A shim volume was manually defined in the DTI acquisition. Four DTI data sets with the same pre-scan values were acquired (4 NEX) separately so that each set can be corrected before calculation of the tensor (as described below). In skeletal muscle DTI studies,

a range of parameters has been employed (b-values from 300-600 s/mm^2 , 6 or 12 gradient directions, 4-8 averages). The DTI parameters that we have used here (12 gradient directions, ASSET application, separate NEX and b-value of 400 s/mm^2) are in the range of those typically employed in muscle DTI studies and have been standardized in our lab for skeletal muscle imaging. To determine the signal to noise ratio (SNR) for each muscle, an additional identical DTI data set was collected so that the difference method (38) could be used in the SNR computation (as described below).

6.3.3.3 Data analysis

Diffusion tensor imaging indices were measured in five muscular regions of interest (ROI) in the foot: quadratus plantae (QP), abductor hallucis (AH), flexor hallucis brevis (FHB), flexor digitorum brevis (FDB), and abductor digiti mini (ADM) (**Fig. 6.1**). Before tensor analyses, the acquired DTI data sets were corrected for motion and eddy currents using FMRIB's linear image registration tool, FLIRT (39), which is part of the FMRIB Software Library, FSL (FMRIB Analysis Group) (40). The reference image for the registration was set as the $b=0$ s/mm^2 image of the first NEX. After image registration and eddy current correction, the DTI data sets were summed and tensor calculation was carried out using analysis of functional neuro-images (AFNI) software (National Institute of Mental Health) (41). ROIs for each of

the investigated muscles were drawn on five slices. SNR was first determined for each muscle ROI. Since parallel imaging was used to acquire the DTI data, SNR was calculated using the difference method as (38):

$$\text{SNR} = \frac{1}{\sqrt{2}} \times \frac{\mu_{sum}}{\sigma_{diff}} \quad (6.1)$$

where μ_{sum} is the mean signal intensity of the ROI in the summed image and σ_{diff} is standard deviation of the ROI signal in the differenced image. This technique requires the acquisition of two separate data sets, hence eight DTI scans were performed and the two resulting summed images from each of the four DTI sets were used to determine the SNR.

Calculation of the diffusion tensor at each voxel of the corrected DTI set was done using AFNI (National Institute of Mental Health) (41) resulting in three eigenvalues ($\lambda_1, \lambda_2, \lambda_3$), ADC and FA, where ADC was computed as:

$$\text{ADC} = \frac{\lambda_1 + \lambda_2 + \lambda_3}{3} \quad (6.2)$$

and FA was calculated with:

$$\text{FA} = \sqrt{\frac{3}{2}} \sqrt{\frac{(\lambda_1 - \langle \lambda \rangle)^2 + (\lambda_2 - \langle \lambda \rangle)^2 + (\lambda_3 - \langle \lambda \rangle)^2}{\lambda_1^2 + \lambda_2^2 + \lambda_3^2}} \quad (6.3)$$

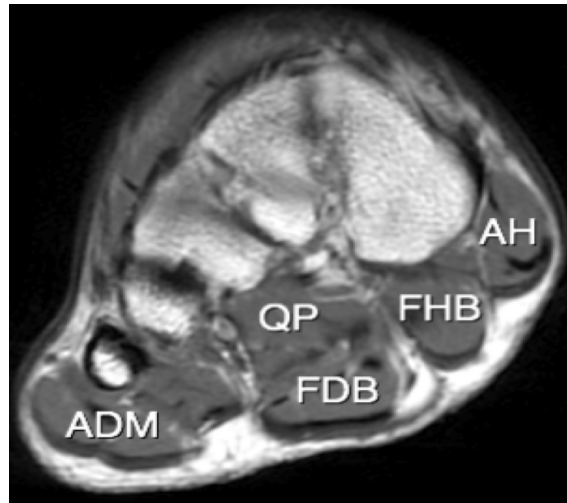


Figure 6.1: Coronal (short axis) T1-weighted image showing the foot muscles that were investigated in this study: quadratus plantae (QP), abductor hallucis (AH), flexor hallucis brevis (FHB), flexor digitorum brevis (FDB), and abductor digiti mini (ADM).

where $\langle \lambda \rangle$ represents the mean of the three eigenvalues.

6.3.3.4 Statistical analysis

To determine if there was significant difference between muscle pairings in terms of eigenvalues, FA or ADC, a repeated measured analysis of variance (ANOVA) with Tukey honestly significant difference (HSD) post hoc test was performed (significance was set at $P < 0.05$). Since five muscles were examined in this study, ten different muscle pairings were possible in total ($5 \text{ choose } 2 = 10$), because the order of each muscle pair did not matter (for instance the QP-

AH pairing is the same as the AH-QP pairing). All statistical analyses were performed using GraphPad Prism (Version 5.0c, GraphPad Software Inc.).

6.3.4 Results

Diffusion tensor metrics (λ_1 , λ_2 , λ_3 , ADC, FA) were measured in the foot of 10 healthy volunteers (**Table 6.1**). A sample T1-weighted anatomical image and the corresponding $b=0\text{s}/\text{mm}^2$ DTI image from one of the subjects is shown in **Fig. 6.2** for two slice locations. **Fig. 6.3** shows images of the three diffusion eigenvalues along with the corresponding T1-weighted anatomical slice for one of the subjects at one anatomic level.

Statistical differences were seen in λ_1 between the following muscle pairings: QP-AH, QP-FHB, AH-FDB, FHB-FDB, and FDB-ADM (**Table 6.2**). None of the muscle pairings showed statistical differences in λ_2 . However, with regards to the third eigenvalue, λ_3 , statistical differences were seen between QP-FDB, AH-FDB, AH-ADM, FHB-FDB and FHB-ADM (**Table 6.2**). None of the paired muscles showed statistical differences in ADC (**Table 6.2**).

The largest FA was measured in the FDB muscle with a mean (\pm SD) of 0.40 ± 0.07 , with all other muscles measuring below 0.30 (**Fig. 6.4**). Statistical differences in FA were seen between the following muscle pairs:

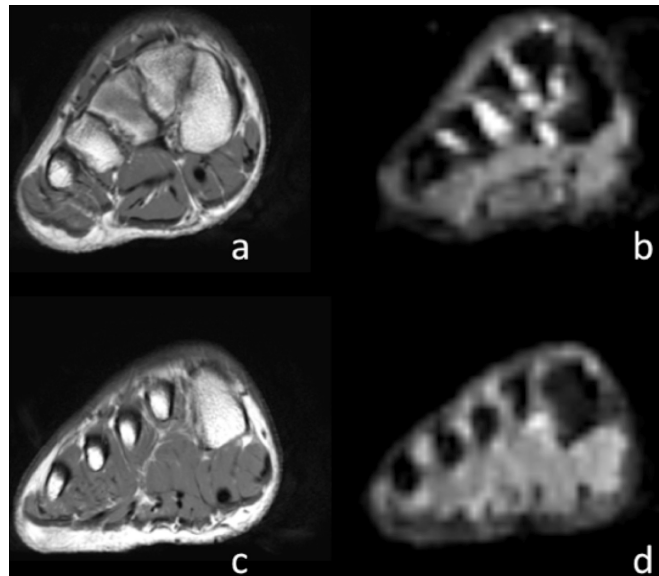


Figure 6.2: Sample anatomical images at two slice locations (a, c) and the corresponding $b=0s/mm^2$ DTI images (b, d) of one of the subjects.

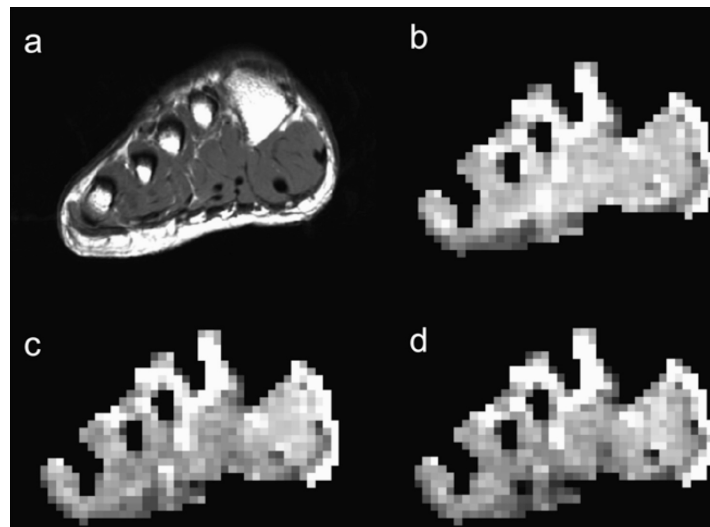


Figure 6.3: Sample anatomical slice (a) along with the tensor eigenvalues: λ_1 (b), λ_2 (c), and λ_3 (d) from one of the subjects.

Muscle		λ_1	λ_2	λ_3	ADC
Quadratus (QP)	plantae	2.05 ± 0.14	1.44 ± 0.10	1.17 ± 0.12	1.55 ± 0.10
Abductor (AH)	hallucis	1.88 ± 0.13	1.43 ± 0.14	1.27 ± 0.09	1.52 ± 0.12
Flexor hallucis brevis (FHB)		1.91 ± 0.19	1.48 ± 0.20	1.25 ± 0.14	1.55 ± 0.18
Flexor digitorum brevis (FDB)		2.14 ± 0.19	1.39 ± 0.18	0.91 ± 0.22	1.48 ± 0.17
Abductor digiti mini (ADM)		1.95 ± 0.15	1.40 ± 0.12	1.07 ± 0.19	1.48 ± 0.14

Table 6.1: DTI eigenvalues ($\lambda_1, \lambda_2, \lambda_3$) and apparent diffusion coefficient (ADC) for muscles in the foot (mean \pm SD). Units of eigenvalues and ADC are expressed as $\times 10^{-3}$ mm²/s.

Muscle pair-ings	λ_1	λ_2	λ_3	ADC	FA
QP-AH	*				*
QP-FHB	*				*
QP-FDB			*		*
QP-ADM					
AH-FHB					
AH-FDB	*		*		*
AH-ADM			*		*
FHB-FDB	*		*		*
FHB-ADM			*		*
FDB-ADM	*				*

Table 6.2: Statistical analysis (repeated measured analysis of variance (ANOVA) with Tukey honestly significant difference (HSD) post hoc test) between pairs of muscle groups for DTI metrics. * Statistical significance defined at $P < 0.05$ between muscles. QP= quadratus plantae, AH= abductor hallucis, FHB= flexor hallucis brevis, FDB= flexor digitorum brevis, and ADM= abductor digiti mini.

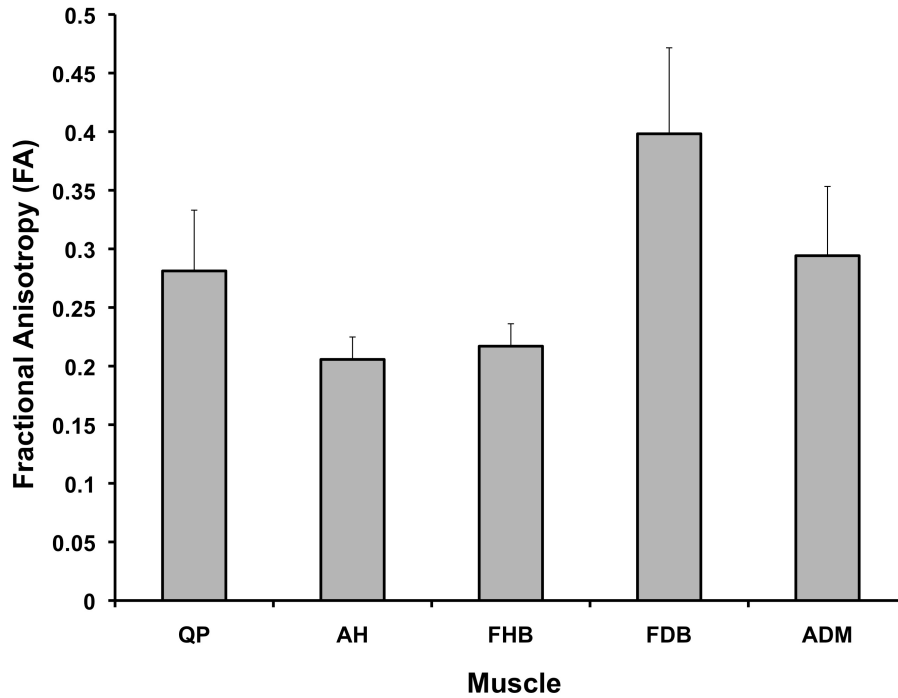


Figure 6.4: The averaged fractional anisotropy, FA (n=10 subjects, error bars represent standard deviation) for each of the five muscle groups: quadratus plantae (QP), abductor hallucis (AH), flexor hallucis brevis (FHB), flexor digitorum brevis (FDB), and abductor digiti mini (ADM).

QP-AH, QP-FHB, QP-FDB, AH-FDB, AH-ADM, FHB-FDB, FHB-ADM and FDB-ADM (**Table 6.2**).

The measured SNR for each of the investigated muscles is given in **Table 6.3**. The averaged SNR ranged from 47.5 - 69.1 in the various muscles examined.

Muscle	SNR
Quadratus plantae (QP)	49.0 ± 16.0
Abductor hallucis (AH)	56.6 ± 25.5
Flexor hallucis brevis (FHB)	69.1 ± 27.4
Flexor digitorum brevis (FDB)	47.5 ± 17.4
Abductor digiti mini	55.7 ± 23.7

Table 6.3: The measured signal to noise ratio (SNR) for each of the investigated foot muscles. Values shown are mean ± SD averaged over all subjects (n=10). SNR was calculated using the difference method (38) as given by Equation 6.1.

6.3.5 Discussion

The aim of our study was to use diffusion tensor imaging to measure the diffusion anisotropy of water in foot muscles of asymptomatic disease free adult subjects. We characterized diffusion tensor metrics (λ_1 , λ_2 , λ_3 , ADC, FA) in five muscles of the foot of healthy volunteers (n=10). The investigated muscles were: the quadratus plantae (QP), the abductor hallucis (AH), the flexor hallucis brevis (FHB), the flexor digitorum brevis (FDB), and the abductor digiti mini (ADM). Although DTI has been previously applied to study various skeletal muscles such as those of the calf (12,14,17,21-34), forearm (11), lumbar (13), and thigh (10,18,20), to our knowledge, this is the first study that has extended the technique to examine foot muscles.

DTI has been shown to provide useful insight into microstructural muscular abnormalities of the calf and the thigh (17-20). DTI derived metrics have

also been shown to alter in the presence of inflammatory markers in the brain (42,43), the liver (4) and the knee joint (44). It is well known that numerous pathologies, including complex regional pain syndrome (CRPS) (36), affect foot tissue and result in muscular abnormalities of the affected limb (45,46). There is also evidence suggesting the presence of inflammatory markers in the affected CRPS limb based on blister fluid samples (47) and skin biopsies (48). Due to its noninvasive nature and since it has been useful in examining muscular abnormalities and inflammatory changes, DTI of the foot could potentially further our understanding of pathologies that affect this region of the body, including CRPS and peripheral vascular diseases. We hope that this technique may allow earlier diagnosis and allow treatment monitoring with serial scans. Our study was thus performed to examine DTI metrics in foot muscles of an asymptomatic population and demonstrate the feasibility of the technique before future applications to a compromised group of volunteers.

In the current study, we measured λ_1 to range from 1.88×10^{-3} to $2.14 \times 10^{-3} \text{ mm}^2/\text{s}$, λ_2 from 1.39×10^{-3} to $1.48 \times 10^{-3} \text{ mm}^2/\text{s}$ and λ_3 from 0.91×10^{-3} to $1.27 \times 10^{-3} \text{ mm}^2/\text{s}$ in the various foot muscles. Our ADC and FA values were observed to range from 1.48×10^{-3} to $1.55 \times 10^{-3} \text{ mm}^2/\text{s}$ and 0.21 to 0.40, respectively. Our measured DTI metrics are similar to those obtained by other groups investigating skeletal muscle DTI (12,14, 49). In one

study, λ_1 was observed to vary from 1.93×10^{-3} to 2.29×10^{-3} mm^2/s , λ_2 from 1.42×10^{-3} to 1.58×10^{-3} mm^2/s and λ_3 from 1.19×10^{-3} to 1.40×10^{-3} mm^2/s in the muscles of the calf of healthy volunteers (12). ADC and FA ranges of 1.53×10^{-3} to 1.67×10^{-3} mm^2/s and 0.18 to 0.33 were reported in that study, respectively (12). Another study investigating diffusive properties of thigh muscles reported λ_1 to range from 2.08×10^{-3} to 2.09×10^{-3} mm^2/s , λ_2 from 1.54×10^{-3} to 1.58×10^{-3} mm^2/s and λ_3 from 1.13×10^{-3} to $\times 10^{-3}$ mm^2/s in the various muscles, with an ADC and FA ranges of 1.59×10^{-3} to 1.62×10^{-3} mm^2/s and 0.27 to 0.30, respectively (49). These reported DTI values are in agreement with our measured metrics in foot muscles.

We observed variations in some of the DTI metrics between foot muscles. Variation in DTI metrics between muscles (i.e. statistical differences between muscle pairs for a given DT index) may be a consequence of varying muscle composition or architecture (14). Specifically, statistical differences were seen between QP-AH, QP-FHB, AH-FDB, FHB-FDB, and FDB-ADM for λ_1 . We did not find any statistical differences in terms of λ_2 between any muscle pairs. However, we noted statistical differences in λ_3 between QP-FDB, AH-FDB, AH-ADM, FHB-FDB and FHB-ADM. Previous reports have shown that there are variations in the eigenvalues across calf muscles (12,14). In the study by Sinha et al., the largest number of statistically different muscle pairs

was seen for λ_1 , while none of the muscles showed differences in terms of λ_3 (12). Galban et al. reported a different pattern, where they found the smallest number of pairs of muscles produced statistical differences on the basis of λ_1 and the largest number of statistically different muscle pairs was seen for λ_3 (14). The results of the current study show an equal number of statistically different muscle pairs for λ_1 and λ_3 . The variations seen in λ_1 between muscle groups have been suggested to stem from the presence of the mitochondria and the sarcoplasmic reticulum, which would result in structural barriers that would vary between muscles (14). Differences seen in λ_3 across muscles have been previously explained to be the result of variations in the radius of muscle fibers (14).

SNR was calculated using the approach for parallel imaging, which requires the acquisition of two DTI data sets (38). The same ROIs used for determining the DTI indices were also employed in the SNR calculation using the $b=0$ images. Our calculated SNR was 49.0 ± 16.0 in the QP muscle, 56.6 ± 25.2 in the AH muscle, 69.1 ± 27.4 in the FHB muscle, 47.5 ± 17.4 in the FDB muscle and 55.7 ± 23.7 in the ADM muscle. It has been previously shown that the behavior of the DTI metrics depends on the SNR level and the b -value used (50). The b -value in the current study was 400 s/mm^2 , and from Fig. 3 of (50), it can be seen that with this b -value, for an accuracy

of 5% in determining the DTI metrics, the required SNR is approximately 5 for λ_1 , 8 for λ_2 , 13 for λ_3 , 9 for ADC and 20 for FA (50). For an accuracy of 1%, an SNR of 11 is needed for λ_1 , 18 for λ_2 , 28 for λ_3 , 18 for ADC, and 43 for FA (50). The SNR calculated in our study was more than 35 in almost all subjects and muscles examined. Thus, we believe our DTI metrics were reliably determined (between 1% and 5% accuracy) since the SNR levels were higher than minimum requirements, as predicted by (50).

In conclusion, we have demonstrated that DTI of the foot is feasible and we have established a normative range of values for the diffusion tensor metrics (λ_1 , λ_2 , λ_3 , ADC, FA) in healthy adult subjects. Our measured DTI indices in the foot were similar to those obtained in calf and thigh skeletal muscles. Future application of the technique to a compromised population could potentially further our understanding of pathologies that affect foot musculature.

6.3.6 References

- (1) Beaulieu C. The basis of anisotropic water diffusion in the nervous system—a technical review. *NMR Biomed* 2002;15:435-55.

- (2) Sotak CH. The role of diffusion tensor imaging in the evaluation of ischemic brain injury- a review. *NMR Biomed* 2002;15:561-569.
- (3) Bode MK, Ruuhonen J, Nieminen MT, et al. Potential of diffusion imaging in brain tumors: a review. *Acta Radiol* 2006;47:585-594.
- (4) Taouli B, Chouli M, Martin AJ, et al. Chronic hepatitis: role of diffusion-weighted imaging and diffusion tensor imaging for the diagnosis of liver fibrosis and inflammation. *J Magn Reson Imaging* 2008;28:89-95.
- (5) Notohamiprodjo M, Dietrich O, Horger W, et al. Diffusion tensor imaging (DTI) of the kidney at 3 Tesla- feasibility, protocol evaluation and comparison to 1.5 Tesla. *Invest Radiol* 2010;45:245-254.
- (6) Sigmund EE, Vivier P-H, Sui D, et al. Intravoxel incoherent motion and diffusion-tensor imaging in renal tissue under hydration and furosemide flow challenges. *Radiology* 2012;263:758-769.
- (7) Hsu EW, Muzikant AL, Matulevicius SA, et al. Magnetic resonance myocardial fiber-orientation mapping with direct histological correlation. *Am J Physiol* 1998;274:H1627-H1634.
- (8) Partridge SC, Murthy RS, Ziadloo A, et al. Diffusion tensor magnetic resonance imaging of the normal breast. *Magn Reson Imaging* 2010;28:320-328.

(9) Gürses B, Kabakci N, Koyanlikaya A, et al. Diffusion tensor imaging of the normal prostate at 3 Tesla. *Eur Radiol* 2008;18:716-721.

(10) Budzik JF, Le Thuc V, Demondion X, et al. In vivo MR tractography of thigh muscles using diffusion imaging: initial results. *Eur Radiol* 2007;17:3079-3085.

(11) Froeling M, Oudeman J, van den Berg S, et al. Reproducibility of diffusion tensor imaging in human forearm muscles at 3.0 T in a clinical setting. *Magn Reson Med*. 2010;64:1182-1190.

(12) Sinha S, Sinha U, Edgerton VR. In vivo diffusion tensor imaging of the human calf muscle. *J Magn Reson Imaging* 2006;24:182-190.

(13) Jones GEG, Kumbhare DA, Harish S, et al. Quantitative DTI assessment in human lumbar stabilization muscles at 3 T. *J Comput Assist Tomogr* 2013;37:98-104.

(14) Galbán CJ, Maderwald S, Uffmann K, et al. Diffusive sensitivity to muscle architecture: a magnetic resonance diffusion tensor imaging study of the human calf. *Eur J Appl Physiol* 2004;93:253-262.

(15) Bassar PJ, Mattiello J, LeBihan D. Estimation of the effective self-diffusion tensor from the NMR spin echo. *J Magn Reson B* 1994;103:247-254.

(16) Noseworthy MD, Davis AD, Elzibak AH. Advanced MR imaging techniques for skeletal muscle evaluation. *Semin Musculoskelet Radiol* 2010;14:257-268.

(17) Zaraiskaya T, Kumbhare D, Noseworthy MD. Diffusion tensor imaging in evaluation of human skeletal muscle injury. *J Magn Reson Imaging* 2006;24:402-408.

(18) Qi J, Olsen NJ, Price RR, et al. Diffusion-weighted imaging of inflammatory myopathies: polymyositis and dermatomyositis. *J Magn Reson Imaging* 2008;27:212-217.

(19) Saotome T, Sekino M, Eto F, et al. Evaluation of diffusional anisotropy and microscopic structure in skeletal muscles using magnetic resonance. *Magn Reson Imaging* 2006;24:19-25.

(20) Cermak NM, Noseworthy MD, Bourgeois JM, et al. Diffusion tensor MRI to assess skeletal muscle disruption following eccentric exercise. *Muscle and Nerve* 2012;46:42-50.

(21) Galban CJ, Maderwald S, Stock F, et al. Age dependence of water diffusivity in human skeletal muscle. *Proc Intl Soc Mag Reson Med* 2006; 257.

(22) Galban CJ, Maderwald S, Stock F, et al. Age-related changes in skeletal muscle as detected by diffusion tensor magnetic resonance imaging. *J Gerontol A Biol Sci Med Sci* 2007;62:453-458.

(23) Galbán CJ, Maderwald S, Uffmann K, et al. A diffusion tensor imaging analysis of gender differences in water diffusivity within human skeletal muscle. *NMR Biomed* 2005;18:489-498.

(24) Okamoto Y, Kunimatsu A, Kono T, et al. Gender differences in MR muscle tractography. *Magn Reson Med Sci.* 2010;9:111-118.

(25) Sinha U, Sinha S, Hodgson JA, et al. Human soleus muscle architecture at different ankle joint angles from magnetic resonance diffusion tensor imaging. *J Appl Physiol* 2011;110:807-819.

(26) Sinha S, Sinha U. Reproducibility analysis of diffusion tensor indices and fiber architecture of human calf muscles in vivo at 1.5 tesla in neutral and plantarflexed ankle positions at rest. *J Magn Reson Imaging* 2011;34:107-119.

(27) Hatakenaka M, Yabuuchi H, Matsuo Y, et al. Effect of passive muscle length change on apparent diffusion coefficient: detection with clinical MR imaging. *Magn Reson Med Sci* 2008;7:59-63.

(28) Okamoto Y, Kunimatsu A, Miki S, et al. Fractional anisotropy values of calf muscles in normative state after exercise: preliminary results. *Magn Reson Med Sci* 2008;7:157-167.

(29) Deux JF, Malzy P, Paragios N, et al. Assessment of calf muscle contraction by diffusion tensor imaging. *Eur Radiol* 2008;18:2303-2310.

(30) Okamoto Y, Kunimatsu A, Kono T, et al. Changes in MR diffusion properties during active muscle contraction in the calf. *Magn Reson Med Sci* 2010;9:1-8.

(31) Heemskerk AM, Drost MR, van Bochove GS, et al. DTI-based assessment of ischemia-reperfusion in mouse skeletal muscle. *Magn Reson Med* 2006;56:272-281.

(32) Hata J, Yagi K, Hikishima k, et al. Diffusion fractional anisotropy-based transformation in skeletal muscle caused by pressure. *Magn Reson Med Sci* 2012;11:179-184.

(33) Damon BM, Ding Z, Anderson AW, et al. Validation of diffusion tensor MRI based muscle fiber tracking. *Magn Reson Med* 2002;48:97-104.

(34) Saupe N, White LM, Sussman MS, et al. Diffusion tensor magnetic resonance imaging of the human calf comparison between 1.5T and 3.0T- preliminary results. *Invest Radiol* 2008;43:612-618.

(35) Greenman RL, Panasyuk S, Wang X, et al. Early changes in the skin microcirculation and muscle metabolism of the diabetic foot. *Lancet* 2005;366:1711-17.

(36) Hulsman NM, Geertzen JHB, Dijkstra PU, et al. Myopathy in CRPS-I: disuse or neurogenic. *Eur J Pain* 2009;13:731-736.

(37) Kos S, Klarhöfer M, Aschwanden M, et al. Simultaneous dynamic blood oxygen level-dependent magnetic resonance imaging of foot and calf muscles. Aging effects at ischemia and postocclusive hyperemia in healthy volunteers. *Invest Radiol* 2009;44:741-747.

(38) Dietrich O, Raya JG, Reeder SB, et al. Measurement of signal-to-noise ratios in MR images: influence of multichannel coils, parallel imaging, and reconstruction filters. *J Magn Reson Imaging* 2007;26:375-385.

(39) Jenkinson M, Bannister P, Brady JM, Smith SM. Improved Optimisation for the Robust and Accurate Linear Registration and Motion Correction of Brain Images. *Neuroimage* 2002;17(2):825-841.

(40) Jenkinson M, Beckmann CF, Behrens TE, Woolrich MW, Smith SM. FSL. *Neuroimage* 2012;62:782-90.

(41) Cox RW. AFNI: software for analysis and visualization of functional magnetic resonance neuroimages. *Comput Biomed Res* 1996;29:162-173.

(42) Gupta RK, Hasan KM, Mishra AM, et al. High fractional anisotropy in brain abscesses versus other cystic intracranial lesions. *Am J Neuroradiol* 2005;26:1107-14.

(43) Trivedi R, Malik GK, Gupta RK, et al. Increased anisotropy in neonatal meningitis: an indicator of meningeal inflammation. *Neuroradiology* 2007;49:767-775.

(44) Agarwal V, Kumar M, Singh JK, et al. Diffusion tensor anisotropy magnetic resonance imaging: a new tool to assess synovial inflammation. *Rheumatology* 2009;48:378-382.

(45) Vas LC, Pai R, Radhakrishnan M. Ultrasound appearance of forearm muscles in 18 patients with complex regional pain syndrome 1 of the upper extremity. *Pain Pract* 2013; 13(1):76-88.

(46) Heerschap A, den Hollander JA, Reynen H, et al. Metabolic changes in reflex sympathetic dystrophy: A 31P NMR spectroscopy study. *Muscle and Nerve* 1993;16:367-373.

(47) Huygen FJ, De Bruijn AG, De Bruin MT, et al. Evidence for local inflammation in complex regional pain syndrome type 1. *Mediators Inflamm* 2002; 11:47-51.

(48) Krämer HH, Eberle T, Üçeyler N, et al. TNF-alpha in CRPS and "normal" trauma- significant differences between tissue and serum. *Pain* 2011;152:285-290.

(49) Gondin J, Callot V, Cozzone PJ, et al. Specific changes in water diffusivity due to passive shortening and lengthening of thigh muscles - a diffusion tensor imaging study. *Proc Intl Soc Mag Reson Med* 2010; 881.

(50) Damon BM. Effects of image noise in muscle diffusion tensor (DT)-MRI assessed using numerical simulations. *Magn Reson Med*. 2008;60:934-944.

Chapter 7

Foot Diffusion Tensor Metrics: Response to Supine Posture

Alyaa H. Elzibak, B.Sc., M.Sc., Dinesh A. Kumbhare, MSc, MD, FRCPC,
Michael D. Noseworthy, Ph.D., P.Eng.

7.1 Context of the Paper

Having noted that diffusion tensor metrics of calf muscles are altered with position-related changes in the first manuscript (**chapter 4**) and having established a normal range of DT metrics in healthy foot muscles in the third manuscript (**chapter 6**), this paper aimed at evaluating whether DT indices are altered in the foot with positional change. Since 34 minutes of supine rest seemed to be necessary to allow DTI indices to stabilize in the calf (**chapter 4**), we measured diffusion metrics in the foot at baseline and at 34 minutes of supine rest. BOLD signal characteristics were not investigated as they did not seem to be sensitive to small differences in muscle use between the two postural states, as observed in the second manuscript (**chapter 5**).

7.2 Declaration Statement

This is a manuscript that has been prepared in final format for submission. Alyaa H. Elzibak, as principle author, wrote the first draft of the article, performed all data and statistical analyses, and created figures/tables as appropriate. Dinesh A. Kumbhare provided the concept of looking at foot muscles using DTI. Michael D. Noseworthy, as corresponding author, provided the concept of assessing DTI metrics in the foot in response to posture change. He also provided guidance, editing and funding.

7.3 Paper

Foot Diffusion Tensor Metrics: Response to Supine Posture

Alyaa H. Elzibak, M.Sc.¹, Dinesh A. Kumbhare, MSc, MD, FRCPC^{2,3}, Michael D. Noseworthy, Ph.D., P.Eng.^{1,2,4,5*}

¹*Department of Medical Physics and Applied Radiation Sciences, McMaster University, Hamilton, Ontario, Canada.*

²*School of Biomedical Engineering, McMaster University, Hamilton, Ontario, Canada.*

³*Department of Medicine, Division of Rehabilitation Sciences, McMaster University, Hamilton, Ontario, Canada.*

⁴*Department of Electrical & Computer Engineering, McMaster University, Hamilton, Ontario, Canada.*

⁵*Department of Radiology, McMaster University, Hamilton, Ontario, Canada.*

*Corresponding Author Address:

Dr. Michael D. Noseworthy, Ph.D., P.Eng.

Associate Professor and Director of Biomedical Engineering

McMaster University, Hamilton, Ontario, Canada

Electrical and Computer Engineering

1280 Main St. West, Hamilton, Ontario, Canada. L8S 4K1

(905) 525-9140 ext.23727

Email: nosewor@mcmaster.ca

7.3.1 Abstract

Objective: To determine the response of foot diffusion tensor eigenvalues (λ_1 , λ_2 , λ_3), apparent diffusion coefficient (ADC) and fractional anisotropy (FA) to positional change from upright to supine posture.

Methods: The dominant foot of nine healthy adults (mean \pm SD: 27.1 ± 6.5 years, 3 females) was imaged using a 3T MR scanner. Data was acquired at baseline (measurement 1) and following 34 minutes of supine rest (measurement 2). DT metrics were examined in five foot muscles (quadratus plantae (QP), abductor hallucis (AH), flexor hallucis brevis (FHB), flexor digitorum brevis (FDB), and abductor digiti mini (ADM)) during each of the two measurement times.

Results: All three eigenvalues and ADC showed significant decreases in the five muscles with positional change ($P < 0.05$). These reductions ranged from 2.7-4.6% in the various foot muscles, following 34 minutes of supine rest ($P < 0.05$). No changes were noted in FA in any of the muscles with supine rest.

Conclusions: The observed changes in the diffusivity of foot muscles with movement from upright to supine position were similar to those previously reported in calf DT metrics. This study further elucidates the need for im-

posing a resting period in the recumbent position before DT data collection.

Key Words: diffusion tensor imaging (DTI), foot, positional change, skeletal muscle

7.3.2 Introduction

Diffusion tensor imaging (DTI) is an emerging technique that is becoming widely used to noninvasively characterize tissue microstructure. It has been applied to study water diffusion in healthy organs (1-8), providing insight into the underlying tissue architecture. Diffusion imaging has also become a valuable tool in assessing numerous pathological conditions that are reflected by modifications in the diffusion of water (9-15), including inflammatory diseases (12-15).

The application of DTI to examine skeletal muscle architecture has been promising, confirming that diffusivity changes accompany microstructural muscle alterations (9, 16-23). DTI measurements are based on the idea that the presence of membranes and other cellular structures impedes the isotropic diffusion of water molecules. In skeletal muscles, this leads to a preferential diffusion of water molecules (24) such that the axis parallel to the muscle fiber shows greater diffusion than that observed along transverse directions (25, 26).

Various elements of the diffusion tensor have been used to express the behavior of the diffusing molecules. These include eigenvalues (λ_1 , λ_2 , λ_3), apparent diffusion coefficient (ADC), and fractional anisotropy (FA). Several

studies have revealed that these indices may be modified in the presence of architectural or pathological muscle disruptions (16-23). For example, plantar flexion and dorsiflexion have been reported to influence the measured diffusion metrics, presumably reflecting changes in muscle fiber structure due to muscle shortening or lengthening (27, 28). In addition, increased water diffusion has been noted in the calf muscles of injured subjects, possibly the result of modified muscle microstructure in these damaged regions (9).

Diffusion imaging of skeletal muscles is dominated by studies that examine the calf region (2,9, 20-23, 25-28), although muscles in other body locations have also been investigated (3,4,18, 19). Recent evaluations have been performed to establish diffusion metrics in foot muscles and the feasibility of examining this region has been demonstrated (6). The current study aims at furthering our understanding of the diffusive behavior in foot muscles, by examining the diffusion indices in the foot following positional change from upright to supine posture.

Extensive research has been carried out to investigate the influence of postural changes on body fluid volume distributions (29, 30) and the accompanying changes in leg volume (31) or muscle cross sectional area (32,33). Recently, DT indices were shown to vary in response to movement from erect to recumbent position in calf muscles (34). The authors noted that most of

the change in the diffusion metrics took place within the first half an hour of assuming the supine position (34). The current work aims at extending the results of the previous research by examining the effect of posture on foot DTI metrics. We measured diffusion indices (λ_1 , λ_2 , λ_3 , ADC and FA) in five muscles of the foot (quadratus plantae (QP), abductor hallucis (AH), flexor hallucis brevis (FHB), flexor digitorum brevis (FDB), and abductor digiti mini (ADM)) of healthy subjects during two imaging sessions. Measurement 1 was acquired after the subjects had arrived to the imaging centre and were ready to be imaged. The second data set (measurement 2) was collected thirty-four minutes after the 1st measurement. Subjects remained in the supine position between these two measurements. We hypothesized that similar changes will be observed in the DTI metrics of foot muscles in response to supine posture, as were seen in calf muscles (34).

7.3.3 Materials and Methods

7.3.3.1 Subjects and Data Collection

Nine healthy adult subjects between 17 and 40 years of age (mean: 27.1 years, height: 173.5 ± 11.1 cm, weight: 65.4 ± 12.8 kg, 3 females) participated in this study. A GE 3.0T MRI system (MR750, GE Healthcare, Milwaukee,

WI) and an HD foot/ankle array coil (GE Healthcare, Milwaukee, WI) were used to scan the foot muscles of the dominant leg of each subject. Images were acquired while subjects lay in the supine position, feet-first in the MR scanner. Subjects were in the fasted state (had been asked to refrain from food and drink intake for four hours prior the study) and had avoided participating in vigorous exercise in the twenty-four hours before the study. The MR imaging session involved two sets of measurements; the first (measurement 1) was collected soon after the subjects had arrived to the centre and were ready to be imaged. Following this first measurement, subjects remained in the supine position in the MR scanner for thirty-four minutes, at which time a second data set (measurement 2) was acquired.

Each data set consisted of coronal anatomical slices (Fast Spin Echo (FSE), TE/TR= 14.9/785 ms, 5mm slice thickness, 0mm gap, FOV=16cm, 320x320 matrix, 20 slices) and DTI slices from matching anatomical locations (dual spin-echo EPI, 15 diffusion encoding gradient directions, TE/TR= 68.8/4050ms, b-value=400 s/mm^2 and one b=0 s/mm^2 image, 5mm slice thickness, 0mm gap, FOV=16cm, 64x64 matrix, 20 slices, ASSET factor of 2, manual shim volume, 4 separate NEX). The neck of the talus bone was used as the starting position for image acquisition as shown in **Fig. 7.1**.

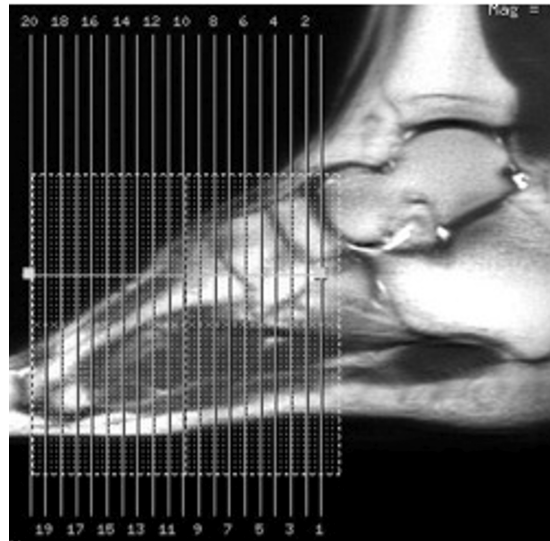


Figure 7.1: Sagittal localizer showing the position of the twenty coronal slices (short axis) acquired in this study. Image collection started from the neck of the talus bone.

7.3.3.2 Data Analysis

All DTI data was analyzed offline using analysis tools from FMRIB Software Library, FSL (35) and analysis of functional neuro-images (AFNI) (36). Before tensor analysis, images were corrected for motion and eddy currents using FMRIB's linear image registration tool, FLIRT (37), as described previously (6, 34). Five slices were chosen for DT metric analyses for each subject. Regions of interest (ROIs) were drawn on these slices in five different muscle groups: the quadratus plantae, the abductor hallucis, the flexor hallucis brevis, the flexor digitorum brevis, and the abductor digiti mini. Diffusion

tensor calculation, using AFNI, produced the DT eigenvalues ($\lambda_1, \lambda_2, \lambda_3$) at each voxel. The ADC was then computed as the mean of the three eigenvalues, and the FA was calculated using:

$$FA = \sqrt{\frac{3}{2}} \sqrt{\frac{(\lambda_1 - ADC)^2 + (\lambda_2 - ADC)^2 + (\lambda_3 - ADC)^2}{\lambda_1^2 + \lambda_2^2 + \lambda_3^2}} \quad (7.1)$$

A paired t-test was carried out to assess if the DT metrics varied between the two measurements for any of the muscles. Statistical analyses were performed using GraphPad Prism (Version 5.0c, GraphPad Software Inc.) and significance was set at $P < 0.05$.

7.3.4 Results

Fig. 7.2 shows the mean of the DTI metrics in the quadratus plantae muscle of the participants at the first and second measurement times. We observed decreases in the eigenvalues and ADC, and no changes in the FA between the two measurement times. A similar behavior was noted for the DT indices in all other muscles as listed in **Table 7.1**. The decreases in the eigenvalues and ADC noted when comparing the first and second measurements were found to be significant in all investigated muscles, and ranged from 2.65

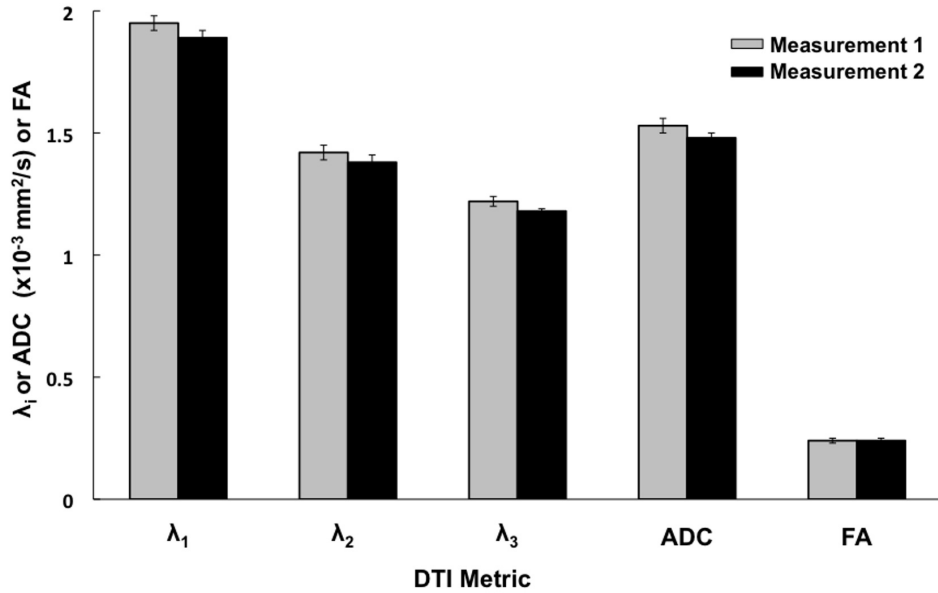


Figure 7.2: Mean DT metrics in the quadratus plantae muscle at the two measurement times (error bars represent SE). We noted significant decreases ($P < 0.05$) between the first and second measurement for all DT indices, except FA. A similar pattern was observed in all other muscle groups (**Table 7.1**).

to 4.59% (**Table 7.2**). No significant changes were noted in the FA (**Table 7.1**) of any of the muscles between the two measurements (quadratus plantae $P = 0.40$, abductor hallucis $P = 0.22$, flexor hallucis brevis $P = 0.13$, flexor digitorum brevis $P = 0.35$, abductor digiti mini $P = 0.18$).

7.3.5 Discussion

The present study was carried out to examine changes in water diffusivity of foot muscles of healthy young subjects that accompany changes in

	Measurement 1	Measurement 2
Quadratus plantae		
λ_1	1.95 ± 0.03	1.89 ± 0.03
λ_2	1.42 ± 0.03	1.38 ± 0.03
λ_3	1.22 ± 0.02	1.18 ± 0.01
ADC	1.53 ± 0.03	1.48 ± 0.02
FA	0.24 ± 0.01	0.24 ± 0.01
Abductor hallucis		
λ_1	1.83 ± 0.04	1.74 ± 0.03
λ_2	1.39 ± 0.04	1.33 ± 0.04
λ_3	1.23 ± 0.03	1.19 ± 0.03
ADC	1.48 ± 0.04	1.42 ± 0.03
FA	0.21 ± 0.01	0.20 ± 0.01
Flexor hallucis brevis		
λ_1	1.87 ± 0.04	1.82 ± 0.03
λ_2	1.45 ± 0.04	1.39 ± 0.04
λ_3	1.26 ± 0.03	1.21 ± 0.03
ADC	1.53 ± 0.04	1.47 ± 0.03
FA	0.20 ± 0.01	0.21 ± 0.01
Flexor digitorum brevis		
λ_1	1.95 ± 0.04	1.89 ± 0.05
λ_2	1.33 ± 0.04	1.29 ± 0.04
λ_3	1.09 ± 0.05	1.04 ± 0.05
ADC	1.46 ± 0.04	1.41 ± 0.04
FA	0.30 ± 0.02	0.30 ± 0.02
Abductor digiti mini		
λ_1	1.92 ± 0.05	1.83 ± 0.04
λ_2	1.34 ± 0.05	1.28 ± 0.04
λ_3	1.09 ± 0.05	1.06 ± 0.05
ADC	1.45 ± 0.05	1.39 ± 0.04
FA	0.29 ± 0.02	0.28 ± 0.01

Table 7.1: Mean of eigenvalues, ADC and FA for the two measurement times in each of the five muscles (n= 9 subjects; mean \pm SE; eigenvalues and ADC are $\times 10^{-3}$ mm²/s). Significant decreases ($P < 0.05$) were observed between the first and second measurement for all DT indices (**Table 7.2**), except the FA.

	% Decrease between the two measurements (P-value)
Quadratus plantae	
λ_1	3.22 ± 0.89 (P < 0.004)
λ_2	2.94 ± 0.82 (P < 0.003)
λ_3	3.66 ± 0.91 (P < 0.003)
ADC	3.26 ± 0.67 (P < 0.001)
Abductor hallucis	
λ_1	4.59 ± 0.71 (P < 0.001)
λ_2	4.03 ± 1.09 (P < 0.004)
λ_3	3.74 ± 1.46 (P < 0.02)
ADC	4.19 ± 0.92 (P < 0.002)
Flexor hallucis brevis	
λ_1	3.04 ± 0.88 (P < 0.006)
λ_2	4.18 ± 1.39 (P < 0.005)
λ_3	4.02 ± 0.90 (P < 0.002)
ADC	3.69 ± 0.84 (P < 0.002)
Flexor digitorum brevis	
λ_1	2.92 ± 1.00 (P < 0.01)
λ_2	2.93 ± 0.84 (P < 0.004)
λ_3	3.93 ± 1.65 (P < 0.03)
ADC	3.19 ± 0.64 (P < 0.001)
Abductor digiti mini	
λ_1	4.17 ± 1.03 (P < 0.002)
λ_2	3.88 ± 0.97 (P < 0.004)
λ_3	2.65 ± 1.76 (P < 0.02)
ADC	3.75 ± 0.79 (P < 0.001)

Table 7.2: % decrease in the DT metrics that showed significant differences between the two measurement time. Data are mean \pm SE.

posture involving movement from upright to recumbent position. To that end, DT metrics (λ_1 , λ_2 , λ_3 , ADC and FA) were measured during two imaging sessions; the first one followed upright posture (measurement 1) and the second one commenced following 34 minutes of supine rest (measurement 2). Examinations were conducted on five regions of the foot: quadratus plantae (QP), abductor hallucis (AH), flexor hallucis brevis (FHB), flexor digitorum brevis (FDB), and abductor digiti mini (ADM).

DT imaging has been carried out in numerous skeletal muscles in the body. However, extension of the technique to the foot region has only been recently attempted (6). The baseline DT metrics obtained in the current study agree well with those published in the foot study (6). We measured λ_1 to vary from 1.83×10^{-3} to 1.95×10^{-3} mm²/s, λ_2 from 1.33×10^{-3} to 1.45×10^{-3} mm²/s and λ_3 from 1.09×10^{-3} to 1.26×10^{-3} mm²/s in the various foot muscles during the first measurement. In the foot study, λ_1 was observed to vary from 1.88×10^{-3} to 2.14×10^{-3} mm²/s, λ_2 from 1.39×10^{-3} to 1.48×10^{-3} mm²/s and λ_3 from 0.91×10^{-3} to 1.27×10^{-3} mm²/s (6). The largest λ_1 values were found in the FDB and QP muscles in both studies, while the smallest value was observed in the AH muscle. The FHB muscle had the highest λ_2 , while the FDB muscle had the smallest value. λ_3 values were smallest in both FDB and ADM muscles.

With regards to ADC and FA, we measured ADC to range from 1.45×10^{-3} to 1.53×10^{-3} mm²/s and FA from 0.20 to 0.30 in the foot muscles. These values were also in fair agreement with those reported in literature for foot metrics (6), where ADC and FA had been noted to range from 1.48×10^{-3} to 1.55×10^{-3} mm²/s and 0.20 to 0.40, respectively (6). The highest ADC values were reported in the QP and FHB muscle in both studies, while FA was highest in the FDB and lowest in the FHB and AH muscles.

We noted that all three of our measured eigenvalues and ADC were reduced in all of the foot muscles following 34 minutes of supine posture, while no significant changes were observed in the FA. The decreases that were noted ranged from 2.65 to 4.59% (**Table 7.2**) in the various metrics. DT indices have been recently shown to change in calf muscles due to supine posture (34). Reductions of 3.2-6.7% have been reported in the eigenvalues and ADC following 34 minutes of supine rest (34). The decreases that we observed in the diffusion metrics in the foot are of the same magnitude as those observed in the calf (34).

Changes in diffusion indices have been reported in response to numerous muscle microstructural alterations, including injuries (9), exercise (21), external pressure (22), and muscle lengthening or shortening (16,18,20). The changes in diffusion metrics that accompany such stimuli range from 7-60 %.

Values near the high end of this interval are seen in cases where traumatic muscle alterations become evident, as in the case of muscle tears (9).

Reductions in water diffusivity, as observed with supine posture, have been previously attributed to stem from reductions in the extracellular space (34). It is generally accepted that supine posture is accompanied by increases in intravascular volume (30). These are presumed to result from movement of fluid from the interstitial space into the blood (30). Expansion of the extracellular space has been speculated to lead to the observed increase in diffusivity noted in inflammatory myopathies (12). Thus, a reduction in diffusivity as noted in the current study could likely be due to a decrease in the extracellular space, as suggested previously (34).

DTI has already been used to look at muscle damage (9) and to study inflammation in numerous body regions (12-15). Application of DT imaging to understand diseases that show loss of motor activity in relation to systemic inflammation, such as chronic obstructive pulmonary disease (COPD) or complex regional pain syndrome (CRPS) could be useful in furthering our understanding of muscle status in such pathological conditions. Since we have noted reductions in the diffusion metrics with posture in this study, it is important to first test the effect of posture in any compromised population. Once an understanding of the response of diffusion metrics to positional change has

been established in a diseased population, any necessary supine posture can be implemented prior to DTI acquisition, leading to accurate DT metric evaluations.

In conclusion, diffusion tensor metrics were examined in foot muscles of young healthy adults in response to positional change involving movement from upright to supine posture. Our results revealed that all three eigenvalues ($\lambda_1, \lambda_2, \lambda_3$) and ADC were reduced following 34 minutes of supine rest. The measured reductions were similar to those reported in calf skeletal muscles. This study further elucidates the need for imposing a resting period in the supine position before commencing DTI data collection.

7.3.6 References

- (1) Partridge SC, Murthy RS, Ziadloo A, et al. Diffusion tensor magnetic resonance imaging of the normal breast. *Magn Reson Imaging* 2010;28:320-328.
- (2) Galbán CJ, Maderwald S, Uffmann K, et al. A diffusion tensor imaging analysis of gender differences in water diffusivity within human skeletal muscle. *NMR Biomed* 2005;18:489-498.

- (3) Jones GEG, Kumbhare DA, Harish S, et al. Quantitative DTI assessment in human lumbar stabilization muscles at 3 T. *J Comput Assist Tomogr* 2013;37:98-104.
- (4) Froeling M, Oudeman J, van den Berg S, et al. Reproducibility of diffusion tensor imaging in human forearm muscles at 3.0 T in a clinical setting. *Magn Reson Med* 2010;64:1182-1190.
- (5) Gürses B, Kabakci N, Koyanlikaya A, et al. Diffusion tensor imaging of the normal prostate at 3 Tesla. *Eur Radiol* 2008;18:716-721.
- (6) Elzibak AH, Kumbhare DA, Harish S, et al. Diffusion tensor imaging of the normal foot at 3T. *J Comput Assist Tomogr* In Press.
- (7) Beaulieu C. The basis of anisotropic water diffusion in the nervous system- a technical review. *NMR Biomed* 2002;15:435-55.
- (8) Notohamiprodjo M, Dietrich O, Horger W, et al. Diffusion tensor imaging (DTI) of the kidney at 3 Tesla- feasibility, protocol evaluation and comparison to 1.5 Tesla. *Invest Radiol* 2010;45:245-254.
- (9) Zaraiskaya T, Kumbhare D, Noseworthy MD. Diffusion tensor imaging in evaluation of human skeletal muscle injury. *J Magn Reson Imaging* 2006;24:402-408.

- (10) Bode MK, Ruohonen J, Nieminen MT, et al. Potential of diffusion imaging in brain tumors: a review. *Acta Radiol* 2006;47:585-594.
- (11) Sotak CH. The role of diffusion tensor imaging in the evaluation of ischemic brain injury- a review. *NMR Biomed* 2002;15:561-569.
- (12) Qi J, Olsen NJ, Price RR, et al. Diffusion-weighted imaging of inflammatory myopathies: polymyositis and dermatomyositis. *J Magn Reson Imaging* 2008;27:212-217.
- (13) Taouli B, Chouli M, Martin AJ, et al. Chronic hepatitis: role of diffusion-weighted imaging and diffusion tensor imaging for the diagnosis of liver fibrosis and inflammation. *J Magn Reson Imaging* 2008;28:89-95.
- (14) Agarwal V, Kumar M, Singh JK, et al. Diffusion tensor anisotropy magnetic resonance imaging: a new tool to assess synovial inflammation. *Rheumatology* 2009;48:378-382.
- (15) Trivedi R, Malik GK, Gupta RK, et al. Increased anisotropy in neonatal meningitis: an indicator of meningeal inflammation. *Neuroradiology* 2007;49:767-775.
- (16) Hatakenaka M, Yabuuchi H, Matsuo Y, et al. Effect of passive muscle length change on apparent diffusion coefficient: detection with clinical MR imaging. *Magn Reson Med Sci* 2008;7:59-63.

- (17) Galban CJ, Maderwald S, Stock F, et al. Age-related changes in skeletal muscle as detected by diffusion tensor magnetic resonance imaging. *J Gerontol A Biol Sci Med Sci* 2007;62:453-458.
- (18) Gondin J, Callot V, Cozzone PJ, et al. Specific changes in water diffusivity due to passive shortening and lengthening of thigh muscles - a diffusion tensor imaging study. *Proc Intl Soc Mag Reson Med* 2010; 881.
- (19) Cermak NM, Noseworthy MD, Bourgeois JM, et al. Diffusion tensor MRI to assess skeletal muscle disruption following eccentric exercise. *Muscle and Nerve* 2012;46:42-50.
- (20) Sinha S, Sinha U. Reproducibility analysis of diffusion tensor indices and fiber architecture of human calf muscles in vivo at 1.5 tesla in neutral and plantarflexed ankle positions at rest. *J Magn Reson Imaging* 2011;34:107-119.
- (21) Okamoto Y, Kunimatsu A, Kono T, et al. Changes in MR diffusion properties during active muscle contraction in the calf. *Magn Reson Med Sci* 2010;9:1-8.
- (22) Hata J, Yagi K, Hikishima k, et al. Diffusion fractional anisotropy-based transformation in skeletal muscle caused by pressure. *Magn Reson Med Sci* 2012;11:179-184.

(23) Deux JF, Malzy P, Paragios N, et al. Assessment of calf muscle contraction by diffusion tensor imaging. *Eur Radiol* 2008;18:2303-2310.

(24) Henkelman RM, Stanisz GJ, Kim JK, et al. Anisotropy of NMR properties of tissues. *Magn Reson Med* 1994;32:592-601.

(25) Sinha S, Sinha U, Edgerton VR. In vivo diffusion tensor imaging of the human calf muscle. *J Magn Reson Imaging* 2006;24:182-190.

(26) Galbán CJ, Maderwald S, Uffmann K, et al. Diffusive sensitivity to muscle architecture: a magnetic resonance diffusion tensor imaging study of the human calf. *Eur J Appl Physiol* 2004;93:253-262.

(27) Okamoto Y, Kunimatsu A, Kono T, et al. Changes in MR diffusion properties during active muscle contraction in the calf. *Magn Reson Med Sci* 2010;9:1-8

(28) Schwenzer NF, Steidle G, Martirosian P, et al. Diffusion tensor imaging of the human calf muscle: distinct changes in fractional anisotropy and mean diffusion due to passive muscle shortening and stretching. *NMR Biomed.* 2009; 22:1047-53.

(29) Thompson WO, Thompson PK, Dailey ME (1928) The effect of posture upon the composition and volume of the blood in man. *J Clin Invest* 5: 573-604

(30) Maw GJ, Mackenzie IL, Taylor NAS. Redistribution of body fluids during postural manipulations. *Acta Physiol Scand* 1995; 155,157-163

(31) Waterfield RL. The effect of posture on the volume of the leg. *J Physiol* 1931; 72,121-123

(32) Berg HE, Tender B, Tesch PA. Changes in lower limb muscle cross-sectional area and tissue fluid volume after transition from standing to supine. *Acta Physiol Scand* 1993;148,379-385

(33) Conley MS, Foley JM, Ploutz-synder LL, Meyer RA, Dudley GA. Effect of acute head-down tilt on skeletal muscle cross-sectional area and proton transverse relaxation time. *J Appl Physiol* 1996; 81:1572-1577

(34) Elzibak AH, Noseworthy MD. Assessment of diffusion tensor imaging indices in calf muscles following postural change from standing to supine position. *Magn Reson Mater Phy* 2013; DOI 10.1007/s10334-013-0424-1.

(35) Jenkinson M, Beckmann CF, Behrens TE, Woolrich MW, Smith SM. FSL. *Neuroimage* 2012;62:782-90.

(36) Cox RW. AFNI: software for analysis and visualization of functional magnetic resonance neuroimages. *Comput Biomed Res* 1996;29:162-173.

(37) Jenkinson M, Bannister P, Brady JM, Smith SM. Improved Optimisation for the Robust and Accurate Linear Registration and Motion Correction of Brain Images. *Neuroimage* 2002;17(2):825-841.

Chapter 8

Conclusions and Future Directions

8.1 Summary of Findings

This thesis helped further our understanding of baseline DTI/ BOLD metrics in calf muscles of healthy subjects. The following were the main findings:

- Examination of calf muscles (anterior tibialis, posterior tibialis, soleus, medial gastrocnemius, and lateral gastrocnemius) using DTI revealed that all three eigenvalues and ADC were reduced in response to movement from the upright to supine position.
- Reductions of 3.2-6.7% and 3.4-7.5% were measured in the various calf DTI metrics, following 34 and 64 minutes of supine rest, respectively ($P < 0.05$).
- No significant changes were noted in any of the eigenvalues or ADC between the second and third imaging sessions for any muscle compartment.

- The FA did not change in any of the investigated calf muscles with supine rest.
- The obtained SNR of the nonweighted image for our calf DTI metrics was (mean \pm SD): 79.2 ± 22.9 in the anterior tibialis muscle, 52.0 ± 18.7 in the posterior tibialis muscle, 55.2 ± 22.3 in the soleus muscle, 77.6 ± 33.2 in the medial gastrocnemius muscle and 95.0 ± 30.9 in the lateral gastrocnemius muscle, leading us to conclude that the indices were accurately determined.
- Examination of calf muscles (anterior tibialis, posterior tibialis, soleus, medial gastrocnemius, and lateral gastrocnemius) using BOLD imaging revealed that measures of global signal characteristics (mean and standard deviation) did not change with supine rest.
- Investigating the BOLD time series using fractals revealed a power law scaling in all investigated calf muscles, and the signals were classified as fBm and had FD values around 1.87.
- We did not find any significant changes in the FD between the three measurement times in any of the calf muscles.

- Spectral analysis of BOLD time series revealed that low frequency peaks (below 0.1 Hz) were the major contributors to the spectrum, with most of the fluctuations at frequencies lower than 0.01 Hz.
- Since variable responses were noted in the power spectra when comparing between muscle compartments and subjects, and due to the difficulty in identifying which frequencies were of physiological origin and which ones reflected low frequency noise, conclusions about changes in power spectrum between the three measurement times were not possible to make.
- Examination of foot muscles (quadratus plantae (QP), abductor hallucis (AH), flexor hallucis brevis (FHB), flexor digitorum brevis (FDB), and abductor digiti mini (ADM)) using DTI revealed that assessing diffusion anisotropy of water in this body region is feasible.
- The measured DTI metrics in the various foot muscles were: λ_1 : 1.88×10^{-3} to 2.14×10^{-3} mm²/s, λ_2 : 1.39×10^{-3} to 1.48×10^{-3} mm²/s, λ_3 : from 0.91×10^{-3} to 1.27×10^{-3} mm²/s, ADC: 1.48×10^{-3} to 1.55×10^{-3} mm²/s and FA: 0.21 to 0.40.
- DTI metrics in the foot were similar to those observed in thigh and calf skeletal muscles.

- Variations were noted in the DTI metrics between foot muscles, that could result from differences in muscle architecture or composition (Galbán et al., 2004). The observed differences were seen between: QP-AH, QP-FHB, AH-FDB, FHB-FDB, and FDB-ADM for λ_1 . QP-FDB, AH-FDB, AH-ADM, FHB-FDB and FHB-ADM for λ_3 .
- The obtained SNR of the nonweighted image for our foot DTI metrics was (mean \pm SD): 49.0 ± 16.0 in the QP muscle, 56.6 ± 25.2 in the AH muscle, 69.1 ± 27.4 in the FHB muscle, 47.5 ± 17.4 in the FDB muscle and 55.7 ± 23.7 in the ADM muscle.
- Examination of foot muscles (quadratus plantae (QP), abductor hallucis (AH), flexor hallucis brevis (FHB), flexor digitorum brevis (FDB), and abductor digiti mini (ADM)) using DTI revealed that all three eigenvalues and ADC were reduced in response to movement from the upright to supine position.
- Reductions of 2.7-4.6% were measured in the various foot DTI metrics, following 34 minutes of supine rest ($P < 0.05$).
- The FA did not change in any of the investigated foot muscles with supine rest.

8.2 Contributions of this Work

The studies examining alterations in diffusivity with positional changes (**chapter 4** and **chapter 7**) were the first, to our knowledge, to show that supine rest might be necessary before calf or foot DTI studies are conducted in order to allow for diffusivity metrics to stabilize. Our results further validated data obtained from studies looking at fluid volume changes that accompany postural manipulations, in that a similar time interval (approx. 30 minutes) seems to be reported by many of these studies in order to allow for the measured metrics to reach a steady value in healthy young subjects. These novel findings could change the way future DTI studies are performed. Posture standardization will most likely be implemented, leading to more reliable metric estimates. We have already started to use a half an hour resting period prior to data collection in skeletal muscle DTI studies being performed in our laboratory.

The study where we set out to establish diffusion metrics in the foot (**chapter 6**) serves as a starting point for many future studies to examine diffusivity changes that accompany diseases of this region of the body, such as peripheral vascular diseases and complex regional pain syndrome. Establishing feasibility of the technique in a region that has not been explored before was a necessary first step that has opened the door for further explorations.

Although investigating BOLD characteristics with positional changes provided negative results (**chapter 5**), it was an important examination to perform, given that the BOLD signal contains information about blood volume and tissue oxygenation and since our DTI studies did show significant changes with posture manipulations. The observed lack of changes in BOLD signal characteristics suggests that resting BOLD signal measurements may not be sensitive to the subtle differences in muscle use between the two postural states. This study has further revealed that BOLD time series of skeletal muscles could be analyzed using fractals, due to the presence of a power law scaling.

8.3 Future Work

Although our studies have added valuable knowledge to that existing in the DTI and BOLD literature of lower limb skeletal muscles, they have opened up the possibility for many more future investigations. First of all, all of the studies were conducted in young, healthy subjects. It remains unknown whether the same positional changes will be seen in the measured metrics of people of different ages or health conditions.

Secondly, in our BOLD work, the fractal dimension was used as a measure of signal complexity. This is a relatively new technique in terms of skeletal muscle BOLD assessments. It is speculated that the use of this method to as-

sess impairment of skeletal muscle microcirculation could be valuable. This is because fractal analysis has provided information of diagnostic and prognostic value previously. Also, losses of fractal scaling or alterations in the power law relationship have been noted in some diseases. Future BOLD studies should be performed on a pixel by pixel basis. This would help eliminate partial volume effects. It would also shed some light on the consistency of the BOLD time series within a muscle group.

For the foot study, the next step is to examine older healthy subjects. This would lead to an understanding of diffusion metrics in the foot region with aging. Following such an extension, foot DTI could be used to investigate muscle status in diseases that show an inflammatory muscle response, providing insight into muscle microstructure. Since the technique is non invasive, repeated studies of the same muscle can be undertaken if needed, allowing for disease status to be tracked.

References

- Basser, P. J. and D. K. Jones (2002, Jan). Diffusion-tensor mri: theory, experimental design and data analysis - a technical review. *NMR Biomed.* 15(7-8), 456–67.
- Basser, P. J., J. Mattiello, and D. LeBihan (1994, Mar). Estimation of the effective self-diffusion tensor from the nmr spin echo. *J Magn Reson B* 103(3), 247–54.
- Bassingthwaighte, J. B., L. S. Liebovitch, and B. J. West (1994). *Fractal physiology*. Oxford University Press, Inc.
- Berg, H. E., B. Tedner, and P. A. Tesch (1993, Aug). Changes in lower limb muscle cross-sectional area and tissue fluid volume after transition from standing to supine. *Acta Physiol Scand* 148(4), 379–85.
- Bernstein, M. A., K. F. King, and X. J. Zhou (2004). *Handbook of MRI Pulse Sequences*. Elsevier Academic Press.
- Bihan, D. L., J. F. Mangin, C. Poupon, C. A. Clark, S. Pappata, N. Molko, and H. Chabriat (2001, Apr). Diffusion tensor imaging: concepts and applications. *J Magn Reson Imaging* 13(4), 534–46.
- Budzik, J. F., V. L. Thuc, X. Demondion, M. Morel, D. Chechin, and A. Cotten (2007, Dec). In vivo mr tractography of thigh muscles using diffusion imaging: initial results. *Eur Radiol* 17(12), 3079–85.
- Bulte, D. P., J. Alfonsi, S. Bells, and M. D. Noseworthy (2006, Oct). Vaso-modulation of skeletal muscle bold signal. *J Magn Reson Imaging* 24(4), 886–90.
- Cermak, N. M., M. D. Noseworthy, J. M. Bourgeois, M. A. Tarnopolsky, and M. J. Gibala (2012, Jul). Diffusion tensor mri to assess skeletal muscle disruption following eccentric exercise. *Muscle Nerve* 46(1), 42–50.
- Conley, M. S., J. M. Foley, L. L. Ploutz-Snyder, R. A. Meyer, and G. A. Dudley (1996, Oct). Effect of acute head-down tilt on skeletal muscle cross-sectional area and proton transverse relaxation time. *J Appl Physiol* 81(4), 1572–7.
- Damon, B. M., M. C. Wadington, J. L. Hornberger, and D. A. Lansdown (2007, Aug). Absolute and relative contributions of bold effects to the

- muscle functional mri signal intensity time course: effect of exercise intensity. *Magn Reson Med* 58(2), 335–45.
- de Figueiredo, E. H. M. S. G., A. F. N. G. Borgonovi, and T. M. Doring (2011, Feb). Basic concepts of mr imaging, diffusion mr imaging, and diffusion tensor imaging. *Magn Reson Imaging Clin N Am* 19(1), 1–22.
- de Graaf, R. A. (2007). *In Vivo NMR Spectroscopy: Principles and Techniques*. John Wiley and Sons Ltd.
- Delignières, D., K. Torre, and L. Lemoine (2005, Oct). Methodological issues in the application of monofractal analyses in psychological and behavioral research. *Nonlinear Dynamics Psychol Life Sci* 9(4), 435–61.
- Deux, J. F., P. Malzy, N. Paragios, G. Bassez, A. Luciani, P. Zerbib, F. Roudot-Thoraval, A. Vignaud, H. Kobeiter, and A. Rahmouni (2008, Oct). Assessment of calf muscle contraction by diffusion tensor imaging. *Eur Radiol* 18(10), 2303–10.
- Dietrich, O., A. Biffar, A. Baur-Melnyk, and M. F. Reiser (2010, Dec). Technical aspects of mr diffusion imaging of the body. *European Journal of Radiology* 76(3), 314–22.
- Duteil, S., C. Wary, J. S. Raynaud, V. Lebon, D. Lesage, A. Leroy-Willig, and P. G. Carlier (2006, Feb). Influence of vascular filling and perfusion on bold contrast during reactive hyperemia in human skeletal muscle. *Magn Reson Med* 55(2), 450–4.
- Eke, A., P. Hermán, J. B. Bassingthwaite, G. M. Raymond, D. B. Percival, M. Cannon, I. Balla, and C. Ikrényi (2000, Feb). Physiological time series: distinguishing fractal noises from motions. *Pflugers Arch* 439(4), 403–15.
- Eke, A., P. Herman, L. Kocsis, and L. R. Kozak (2002, Feb). Fractal characterization of complexity in temporal physiological signals. *Physiol. Meas.* 23(1), R1–38.
- Eke, A., P. Herman, B. G. Sanganahalli, F. Hyder, P. Mukli, and Z. Nagy (2012, Jan). Pitfalls in fractal time series analysis: fmri bold as an exemplary case. *Front Physiol* 3, 417.
- Exeter, D. and D. A. Connell (2010, Jun). Skeletal muscle: functional anatomy and pathophysiology. *Semin Musculoskelet Radiol* 14(2), 97–105.
- Froeling, M., J. Oudeman, S. V. D. Berg, K. Nicolay, M. Maas, G. J. Strijkers, M. R. Drost, and A. J. Nederveen (2010, Aug). Reproducibility of

- diffusion tensor imaging in human forearm muscles at 3.0 t in a clinical setting. *Magn. Reson. Med.* 64(4), 1182–1190.
- Galbán, C. J., S. Maderwald, F. Stock, and M. E. Ladd (2007, Apr). Age-related changes in skeletal muscle as detected by diffusion tensor magnetic resonance imaging. *J Gerontol A Biol Sci Med Sci* 62(4), 453–8.
- Galbán, C. J., S. Maderwald, K. Uffmann, A. de Greiff, and M. E. Ladd (2004, Dec). Diffusive sensitivity to muscle architecture: a magnetic resonance diffusion tensor imaging study of the human calf. *Eur J Appl Physiol* 93(3), 253–62.
- Galbán, C. J., S. Maderwald, K. Uffmann, and M. E. Ladd (2005, Dec). A diffusion tensor imaging analysis of gender differences in water diffusivity within human skeletal muscle. *NMR Biomed.* 18(8), 489–98.
- Gold, G. E., E. Han, J. Stainsby, G. Wright, J. Brittain, and C. Beaulieu (2004, Aug). Musculoskeletal mri at 3.0 t: relaxation times and image contrast. *AJR Am J Roentgenol* 183(2), 343–51.
- Goldberger, A. L. and B. J. West (1987, Jan). Fractals in physiology and medicine. *Yale J Biol Med* 60(5), 421–35.
- Gondin, J., V. Callot, P. Cazzone, D. Bendahan, and G. Duhamel (2010, Nov). Specific changes in water diffusivity due to passive shortening and lengthening of the thigh muscles- a diffusion tensor imaging study. *Proc. Intl. Soc. Mag. Reson. Med.* 18, 881.
- Greenman, R. L., S. Panasyuk, X. Wang, T. E. Lyons, T. Dinh, L. Longoria, J. M. Giurini, J. Freeman, L. Khaodhiar, and A. Veves (2005, Nov). Early changes in the skin microcirculation and muscle metabolism of the diabetic foot. *Lancet* 366(9498), 1711–7.
- Hagan, R. D., F. J. Diaz, and S. M. Horvath (1978, Sep). Plasma volume changes with movement to supine and standing positions. *J Appl Physiol* 45(3), 414–7.
- Hagmann, P., L. Jonasson, P. Maeder, J.-P. Thiran, V. J. Wedeen, and R. Meuli (2006, Oct). Understanding diffusion mr imaging techniques: from scalar diffusion-weighted imaging to diffusion tensor imaging and beyond. *Radiographics* 26 Suppl 1, S205–23.
- Hashemi, R. H., W. G. Bradley, and C. J. Lisanti (2004). *MRI: The basics*. Lippincott Williams and Wilkins.
- Hata, J., K. Yagi, K. Hikishima, Y. Komaki, M. Goto, and K. Yano (2012, Jan). Diffusion fractional anisotropy-based transformation in skeletal muscle caused by pressure. *Magn Reson Med Sci* 11(3), 179–84.

- Hatakenaka, M., H. Yabuuchi, Y. Matsuo, T. Okafuji, T. Kamitani, T. Setoguchi, K. Nishikawa, and H. Honda (2008, Jan). Effect of passive muscle length change on apparent diffusion coefficient: detection with clinical mr imaging. *Magn Reson Med Sci* 7(2), 59–63.
- Heemskerk, A. M., M. R. Drost, G. S. van Bochove, M. F. M. van Oosterhout, K. Nicolay, and G. J. Strijkers (2006, Aug). Dti-based assessment of ischemia-reperfusion in mouse skeletal muscle. *Magn Reson Med* 56(2), 272–81.
- Heemskerk, A. M., T. K. Sinha, K. J. Wilson, Z. Ding, and B. M. Damon (2010, Apr). Repeatability of dti-based skeletal muscle fiber tracking. *NMR Biomed.* 23(3), 294–303.
- Heemskerk, A. M., G. J. Strijkers, M. R. Drost, G. S. van Bochove, and K. Nicolay (2007, May). Skeletal muscle degeneration and regeneration after femoral artery ligation in mice: monitoring with diffusion mr imaging. *Radiology* 243(2), 413–21.
- Huegli, R. W., A.-C. Schulte, M. Aschwanden, C. Thalhammer, S. Kos, A. L. Jacob, and D. Bilecen (2009, Feb). Effects of percutaneous transluminal angioplasty on muscle bold-mri in patients with peripheral arterial occlusive disease: preliminary results. *Eur Radiol* 19(2), 509–15.
- Hulsman, N. M., J. H. B. Geertzen, P. U. Dijkstra, J. J. A. M. van den Dungen, and W. F. A. den Dunnen (2009, Aug). Myopathy in crps-i: disuse or neurogenic? *Eur J Pain* 13(7), 731–6.
- Iyengar, N., C. K. Peng, R. Morin, A. L. Goldberger, and L. A. Lipsitz (1996, Oct). Age-related alterations in the fractal scaling of cardiac interbeat interval dynamics. *Am J Physiol* 271(4 Pt 2), R1078–84.
- Jacobi, B., G. Bongartz, S. Partovi, A.-C. Schulte, M. Aschwanden, A. B. Lumsden, M. G. Davies, M. Loebe, G. P. Noon, S. Karimi, J. K. Lyo, D. Staub, R. W. Huegli, and D. Bilecen (2012, Jun). Skeletal muscle bold mri: from underlying physiological concepts to its usefulness in clinical conditions. *J Magn Reson Imaging* 35(6), 1253–65.
- Jacobi, B., A.-C. Schulte, S. Partovi, S. Michel, S. Karimi, J. K. Lyo, T. Daikeler, M. Aschwanden, D. Staub, L. Zipp, M. Rasmus, R. W. Huegli, G. Bongartz, and D. Bilecen (2013, Mar). Alterations of skeletal muscle microcirculation detected by blood oxygenation level-dependent mri in a patient with granulomatosis with polyangiitis. *Rheumatology* 52(3), 579–81.

- Johnson, M., J. Polgar, D. Weightman, and D. Appleton (1973, Jan). Data on the distribution of fiber types in thirty-six human muscles. an autopsy study. *Journal of the neurological Sciences* 18(1), 111–129.
- Jones, G. E. G., D. A. Kumbhare, S. Harish, and M. D. Noseworthy (2013, Jan). Quantitative dti assessment in human lumbar stabilization muscles at 3 t. *J Comput Assist Tomogr* 37(1), 98–104.
- Jordan, B. F., J. Z. Kimpalou, N. Beghein, C. Dessy, O. Feron, and B. Gallez (2004, Aug). Contribution of oxygenation to bold contrast in exercising muscle. *Magn Reson Med* 52(2), 391–6.
- Kalliokoski, K. K., T. A. Kuusela, M. S. Laaksonen, J. Knuuti, and P. Nuutila (2003, Jan). Muscle fractal vascular branching pattern and microvascular perfusion heterogeneity in endurance-trained and untrained men. *The Journal of Physiology* 546(Pt 2), 529–35.
- Kan, J. H., A. M. Heemskerk, Z. Ding, A. Gregory, G. Mencio, K. Spindler, and B. M. Damon (2009, Mar). Dti-based muscle fiber tracking of the quadriceps mechanism in lateral patellar dislocation. *J Magn Reson Imaging* 29(3), 663–70.
- Kermarrec, E., J.-F. Budzik, C. Khalil, V. L. Thuc, C. Hancart-Destee, and A. Cotten (2010, Nov). In vivo diffusion tensor imaging and tractography of human thigh muscles in healthy subjects. *AJR Am J Roentgenol* 195(5), W352–6.
- Kiviniemi, V. J. (2009, Jan). Mapping transient hyperventilation induced alterations with estimates of the multi-scale dynamics of bold signal. *Front. Neuroinform.* 3, 1–10.
- klarhofer, M., S. Kos, M. Aschwanden, A. Jacob, K. Scheffler, and D. Bilecen (2008, Nov). Dynamic bold mri of calf and foot muscles. *Proc. Intl. Soc. Mag. Reson. Med.* (16), 604.
- Kos, S., M. Klarhöfer, M. Aschwanden, K. Scheffler, A. L. Jacob, and D. Bilecen (2009, Nov). Simultaneous dynamic blood oxygen level-dependent magnetic resonance imaging of foot and calf muscles: aging effects at ischemia and postocclusive hyperemia in healthy volunteers. *Invest Radiol* 44(11), 741–7.
- Lebon, V., C. Brillault-Salvat, G. Bloch, A. Leroy-Willig, and P. G. Carlier (1998, Oct). Evidence of muscle bold effect revealed by simultaneous interleaved gradient-echo nmri and myoglobin nmrs during leg ischemia. *Magn Reson Med* 40(4), 551–8.

- Ledermann, H. P., H.-G. Heidecker, A.-C. Schulte, C. Thalhammer, M. Aschwanden, K. A. Jaeger, K. Scheffler, and D. Bilecen (2006, Nov). Calf muscles imaged at bold mr: correlation with tcpo2 and flowmetry measurements during ischemia and reactive hyperemia—initial experience. *Radiology* 241(2), 477–84.
- Ledermann, H.-P., A.-C. Schulte, H.-G. Heidecker, M. Aschwanden, K. A. Jäger, K. Scheffler, W. Steinbrich, and D. Bilecen (2006a, Jun). Blood oxygenation level-dependent magnetic resonance imaging of the skeletal muscle in patients with peripheral arterial occlusive disease. *Circulation* 113(25), 2929–35.
- Ledermann, H.-P., A.-C. Schulte, H.-G. Heidecker, M. Aschwanden, K. A. Jäger, K. Scheffler, W. Steinbrich, and D. Bilecen (2006b, Jun). Blood oxygenation level-dependent magnetic resonance imaging of the skeletal muscle in patients with peripheral arterial occlusive disease. *Circulation* 113(25), 2929–35.
- Liang, Z.-P. and P. C. Lauterbur (2000). *Principles of magnetic resonance imaging: a signal processing perspective*. Institute of Electrical and Electronics Engineers, Inc.
- Lin, C., M. Bernstein, J. Huston, and S. Fain (2001, Apr). 1391. *Proc Intl Soc Mag Reson Med* 9, 1391.
- Lopes, R. and N. Betrouni (2009, Aug). Fractal and multifractal analysis: A review. *Medical Image Analysis* 13(4), 634–649.
- Maw, G. J., I. L. Mackenzie, and N. A. Taylor (1995, Oct). Redistribution of body fluids during postural manipulations. *Acta Physiol Scand* 155(2), 157–63.
- Maxim, V., L. Sendur, J. Fadili, J. Suckling, R. Gould, R. Howard, and E. Bullmore (2005, Mar). Fractional gaussian noise, functional mri and alzheimer’s disease. *NeuroImage* 25(1), 141–58.
- McRobbie, D. W., E. A. Moore, M. J. Graves, and M. R. Prince (2003). *MRI from Picture to Proton*. Cambridge University Press.
- Meyer, R. A., T. F. Towse, R. W. Reid, R. C. Jayaraman, R. W. Wiseman, and K. K. McCully (2004, Oct). Bold mri mapping of transient hyperemia in skeletal muscle after single contractions. *NMR Biomed.* 17(6), 392–8.
- Mori, S. (2007). *Introduction to diffusion tensor imaging*. Elsevier.
- Mori, S. and J. Zhang (2006, Sep). Principles of diffusion tensor imaging and its applications to basic neuroscience research. *Neuron* 51(5), 527–39.

- Mukherjee, P., J. I. Berman, S. W. Chung, C. P. Hess, and R. G. Henry (2008, Apr). Diffusion tensor mr imaging and fiber tractography: theoretic underpinnings. *AJNR Am J Neuroradiol* 29(4), 632–41.
- Noseworthy, M. D., D. P. Bulte, and J. Alfonsi (2003, Dec). Bold magnetic resonance imaging of skeletal muscle. *Semin Musculoskelet Radiol* 7(4), 307–15.
- Noseworthy, M. D., A. D. Davis, and A. H. Elzibak (2010, Jun). Advanced mr imaging techniques for skeletal muscle evaluation. *Semin Musculoskelet Radiol* 14(2), 257–68.
- Okamoto, Y., A. Kunimatsu, T. Kono, Y. Kujiraoka, J. Sonobe, and M. Minami (2010, Jan). Gender differences in mr muscle tractography. *Magn Reson Med Sci* 9(3), 111–8.
- Okamoto, Y., A. Kunimatsu, T. Kono, K. Nasu, J. Sonobe, and M. Minami (2010, Jan). Changes in mr diffusion properties during active muscle contraction in the calf. *Magn Reson Med Sci* 9(1), 1–8.
- Okamoto, Y., A. Kunimatsu, S. Miki, M. Shindo, M. Niitsu, and M. Minami (2008, Jan). Fractional anisotropy values of calf muscles in normative state after exercise: preliminary results. *Magn Reson Med Sci* 7(3), 157–62.
- Paramanathan, P. and R. Uthayakumar (2008, Mar). Application of fractal theory in analysis of human electroencephalographic signals. *Comput Biol Med* 38(3), 372–8.
- Partovi, S., M. Aschwanden, B. Jacobi, A.-C. Schulte, U. A. Walker, D. Staub, S. Imfeld, P. Broz, D. Benz, L. Zipp, K. A. Jaeger, M. Takes, M. R. Robbin, R. W. Huegeli, and D. Bilecen (2013, Feb). Correlation of muscle bold mri with transcutaneous oxygen pressure for assessing microcirculation in patients with systemic sclerosis. *J Magn Reson Imaging*.
- Partovi, S., S. Karimi, B. Jacobi, A.-C. Schulte, M. Aschwanden, L. Zipp, J. K. Lyo, C. Karmonik, M. Müller-Eschner, R. W. Huegeli, G. Bongartz, and D. Bilecen (2012, Aug). Clinical implications of skeletal muscle blood-oxygenation-level-dependent (bold) mri. *MAGMA* 25(4), 251–61.
- Partovi, S., A.-C. Schulte, M. Aschwanden, D. Staub, D. Benz, S. Imfeld, B. Jacobi, P. Broz, K. A. Jäger, M. Takes, R. W. Huegeli, D. Bilecen, and U. A. Walker (2012, Oct). Impaired skeletal muscle microcirculation in systemic sclerosis. *Arthritis Res Ther* 14(5), R209.

- Partovi, S., A.-C. Schulte, B. Jacobi, M. Klarhöfer, A. B. Lumsden, M. Loebe, M. G. Davies, G. P. Noon, C. Karmonik, L. Zipp, G. Bongartz, and D. Bilecen (2012, May). Blood oxygenation level-dependent (bold) mri of human skeletal muscle at 1.5 and 3 t. *J Magn Reson Imaging* 35(5), 1227–32.
- Potthast, S., A. Schulte, S. Kos, M. Aschwanden, and D. Bilecen (2009, Dec). Blood oxygenation level-dependent mri of the skeletal muscle during ischemia in patients with peripheral arterial occlusive disease. *Rofo* 181(12), 1157–61.
- Prince, J. L. and J. Links (2006). *Medical Imaging Signals and Systems*. Pearson Prentice Hall.
- Qi, J., N. J. Olsen, R. R. Price, J. A. Winston, and J. H. Park (2008, Jan). Diffusion-weighted imaging of inflammatory myopathies: polymyositis and dermatomyositis. *J Magn Reson Imaging* 27(1), 212–7.
- Sanchez, O. A., E. A. Copenhaver, C. P. Elder, and B. M. Damon (2010, Aug). Absence of a significant extravascular contribution to the skeletal muscle bold effect at 3 t. *Magn Reson Med* 64(2), 527–35.
- Schepers, H. E., J. H. G. M. van Beek, and J. B. Bassingthwaighte (2002, Aug). Four methods to estimate the fractal dimension from self-affine signals. *IEEE Eng Med Biol Mag* 11(2), 57–64.
- Schewzow, K., M. Andreas, E. Moser, M. Wolzt, and A. I. Schmid (2012, Nov). Automatic model-based analysis of skeletal muscle bold-mri in reactive hyperemia. *J Magn Reson Imaging*.
- Schulte, A.-C., M. Aschwanden, and D. Bilecen (2008, May). Calf muscles at blood oxygen level-dependent mr imaging: aging effects at postocclusive reactive hyperemia. *Radiology* 247(2), 482–9.
- Schwenzer, N. F., G. Steidle, P. Martirosian, C. Schraml, F. Springer, C. D. Claussen, and F. Schick (2009, Dec). Diffusion tensor imaging of the human calf muscle: distinct changes in fractional anisotropy and mean diffusion due to passive muscle shortening and stretching. *NMR Biomed.* 22(10), 1047–53.
- Shier, D., J. Butler, and R. Lewis (2006). *Hole's essentials of human anatomy and physiology* (Ninth ed.). McGraw-Hill.
- Sinha, S. and U. Sinha (2011, Jul). Reproducibility analysis of diffusion tensor indices and fiber architecture of human calf muscles in vivo at 1.5 tesla in neutral and plantarflexed ankle positions at rest. *J Magn Reson Imaging* 34(1), 107–19.

- Sinha, S., U. Sinha, and V. R. Edgerton (2006, Jul). In vivo diffusion tensor imaging of the human calf muscle. *J Magn Reson Imaging* 24(1), 182–90.
- Sinha, U., S. Sinha, J. A. Hodgson, and R. V. Edgerton (2011, Mar). Human soleus muscle architecture at different ankle joint angles from magnetic resonance diffusion tensor imaging. *J Appl Physiol* 110(3), 807–19.
- Sinha, U. and L. Yao (2002, Jan). In vivo diffusion tensor imaging of human calf muscle. *J Magn Reson Imaging* 15(1), 87–95.
- Slade, J. M., T. F. Towse, V. V. Gossain, and R. A. Meyer (2011, Nov). Peripheral microvascular response to muscle contraction is unaltered by early diabetes but decreases with age. *J Appl Physiol* 111(5), 1361–71.
- Thompson, W. O., P. K. Thompson, and M. E. Dailey (1928, Jun). The effect of posture upon the composition and volume of the blood in man. *J Clin Invest* 5(4), 573–604.
- Towse, T. F., J. M. Slade, J. A. Ambrose, M. C. DeLano, and R. A. Meyer (2011, Jul). Quantitative analysis of the postcontractile blood-oxygenation-level-dependent (bold) effect in skeletal muscle. *J Appl Physiol* 111(1), 27–39.
- Towse, T. F., J. M. Slade, and R. A. Meyer (2005, Aug). Effect of physical activity on mri-measured blood oxygen level-dependent transients in skeletal muscle after brief contractions. *J Appl Physiol* 99(2), 715–22.
- Trappe, S. W., T. A. Trappe, G. A. Lee, and D. L. Costill (2001, Apr). Calf muscle strength in humans. *Int J Sports Med* 22(3), 186–91.
- Wang, K., M. P. A. van Meer, K. van der Marel, A. van der Toorn, L. Xu, Y. Liu, M. A. Viergever, T. Jiang, and R. M. Dijkhuizen (2011, Jan). Temporal scaling properties and spatial synchronization of spontaneous blood oxygenation level-dependent (bold) signal fluctuations in rat sensorimotor network at different levels of isoflurane anesthesia. *NMR Biomed.* 24(1), 61–7.
- Wansapura, J. P., S. K. Holland, R. S. Dunn, and W. S. Ball (1999, Apr). Nmr relaxation times in the human brain at 3.0 tesla. *J Magn Reson Imaging* 9(4), 531–8.
- Wardlaw, G., R. Wong, and M. D. Noseworthy (2008, Jun). Identification of intratumour low frequency microvascular components via bold signal fractal dimension mapping. *Phys Med* 24(2), 87–91.

- Warsi, M. A., W. Molloy, and M. D. Noseworthy (2012, Oct). Correlating brain blood oxygenation level dependent (bold) fractal dimension mapping with magnetic resonance spectroscopy (mrs) in alzheimer's disease. *MAGMA* 25(5), 335–44.
- Waterfield, R. L. (1931, Jun). The effect of posture on the volume of the leg. *The Journal of Physiology* 72(1), 121–31.
- Wigmore, D. M., B. M. Damon, D. M. Pober, and J. A. Kent-Braun (2004, Dec). Mri measures of perfusion-related changes in human skeletal muscle during progressive contractions. *J Appl Physiol* 97(6), 2385–94.
- Winston, G. P. (2012, Dec). The physical and biological basis of quantitative parameters derived from diffusion mri. *Quant Imaging Med Surg* 2(4), 254–65.
- Yanagisawa, O., D. Shima, K. Maruyama, and M. Nielsen (2009, Mar). Evaluation of exercised or cooled skeletal muscle on the basis of diffusion-weighted magnetic resonance imaging. *Eur J Appl Physiol* 105(5), 723–9.
- Zaraiskaya, T., D. Kumbhare, and M. D. Noseworthy (2006, Aug). Diffusion tensor imaging in evaluation of human skeletal muscle injury. *J Magn Reson Imaging* 24(2), 402–8.
- Zuo, C. S., Y.-H. Sung, D. C. Simonson, E. Habecker, J. Wang, C. Haws, R. A. Villafuerte, M. E. Henry, R. L. Dobbins, R. J. Hodge, D. J. R. Nunez, and P. F. Renshaw (2012, Jan). Reduced t2* values in soleus muscle of patients with type 2 diabetes mellitus. *PLoS ONE* 7(11), e49337.